

Effects of cancerous mutations on mechanosensing of cells

A dissertation
Submitted to the Faculty of the
WORCESTER POLYTECHNIC INSTITUTE
In partial fulfillment of the requirements for the Degree of
Doctorate of Philosophy in Physics

August 2020

By

Minh-Tri Ho Thanh

Qi Wen, Ph.D.

Doctoral Advisor
Associate Professor
Worcester Polytechnic Institute
Department of Physics and Department of
Biomedical Engineering

Douglas Petkie, Ph.D.

Professor and Department Head
Worcester Polytechnic Institute
Department of Physics

Kristen Billiar, Ph.D.

Professor and Department Head
Worcester Polytechnic Institute
Department of Biomedical Engineering

Kun-Ta Wu, Ph.D.

Assistant Professor
Worcester Polytechnic Institute
Department of Physics

Abstract

The ability of cells to sense mechanical cues is essential for normal cell function, tissue development, and wound healing. Aberrant sensitivity to mechanical cues from the extracellular environment has been observed in cancer cells and many other types of diseases. Abnormal activities/expression of several proteins have been identified as hallmarks of cancer. Understanding how these proteins regulate the mechanosensing ability of cells would further explore the potential usage of these proteins as targets for cancer therapeutics. In this study, we characterized the effects of three prominent cancer markers used in pharmacology—vimentin, PTEN and KRAS—on cells' mechanosensing behavior. We observed that lowering the level of vimentin expression in fibroblasts reduces the cell traction force but does not affect mechanosensing ability. These results suggest that the function of vimentin in mechanosensing is facilitating the force transmission inside cells. By studying the effects of knocking out PTEN and overexpressing KRAS in MCF-10A breast epithelial cells, we investigated the impacts of cancer-associated pathways PI3K/AKT and Ras/MAPK on mechanosensing. Knocking out PTEN abolished mechanosensing ability and inhibited the formation of stress fibers—bundles of actin filaments—which is critical for force transmission and hence mechanosensing. Overexpressing KRAS promotes stress fiber formation but did not significantly affect the mechanosensing of MCF-10A. Furthermore, KRAS overexpression overturns the effects of PTEN knockout on stress fiber and rescues the mechanosensing ability of PTEN knockout cells. Our results suggest that both the PI3K/AKT pathway (upregulated via PTEN loss) and the KRAS/MAPK pathway (upregulated via KRAS overexpression) impact mechanosensing through their effects on the actin cytoskeleton. More importantly, we unveiled that the crosstalk of these two pathways co-modulates mechanosensing and cell migration.

Acknowledgement

I would like to thank Dr. Qi Wen, for his support, advice, and introduction to the field of biophysics, which provided a foundation for my experimental design and data analysis. I would like to thank my thesis committee members, Dr. Kristen Billiar and Dr. Kun-Ta Wu, for taking the time to help me with the focus of my research. Special thanks to Dr. Douglas Petkie for becoming my committee member at the last minute during this hectic time. I would like to thank the collaborators and members of Dr. Wen's laboratory group for their insight and support: Dr. Sakthikumar Ambady (Biomedical Engineering Department at WPI) for providing fibroblasts with the vimentin knockdown; Dr. Michele Vitolo (University of Maryland) for providing the breast epithelial cell lines; Gawain Thomas for helping with MATLAB; Dr. Jiaxin Gong for his immunofluorescence guidance; Will Linthicum and Jiazhang Chen for helping with atomic force microscopy; Pengbo Wang for assisting me with imaging instruments. I would like to also acknowledge the funding support from American Cancer Society (Research Scholar Grant, RSG-18-028-01-CSM) and from National Science Foundation (CBET-1403257). Finally, I would like to thank Worcester Polytechnic Institute Physics Department for providing me the funding support needed to complete my thesis.

Table of Contents

Abstract.....	2
Acknowledgement	3
List of Figures	7
List of Tables	8
List of Abbreviations	9
Chapter 1: Background and Introduction	11
1.1 Mechanosensing	11
1.1.1 Cytoskeleton	13
1.1.2 Stress fibers in mechanosensing	16
1.1.3 Focal adhesion	17
1.2 Mechanosensing in cancer.....	19
1.2.1 Epithelial-mesenchymal transition.....	20
1.2.2 Mechanosensing of cancer cells.....	21
1.2.3 Vimentin in cancer.....	22
1.2.4 PI3K/AKT and Ras/MAPK pathway in cancer.....	24
Chapter 2: Method overview.....	27
2.1 Traction Force Microscopy.....	27
2.1.1 Background.....	27
2.1.2 Principle of traction force microscopy	29
2.1.3 Procedure of TFM.....	32
2.1.4 Calculation of Force correlation length	36
2.2 Substrate Preparation	36
2.3 Imaging System	37
2.4 Additional Analysis	38
2.4.1 Cell Spreading Area and Cell Polarity	38
2.4.2 Immunofluorescence.....	38
2.4.3 Migration characterization	39
Chapter 3: Effects of vimentin knockdown on fibroblasts' mechanosensing	42
3.1 Background.....	42

3.2 Materials and Methods	43
3.2.1 Cell Lines	43
3.2.2 Substrate preparation	45
3.2.3 Cell viscoelasticity measurements.....	45
3.2.4 Migration Studies	46
3.2.5 Statistics.....	46
3.3 Results	47
3.3.1 Vimentin knockdown does not affect the ability of cells to sense substrate rigidity ..	47
3.3.2 Vimentin knockdown leads to a reduction in total cell traction force.....	49
3.3.3 Vimentin knockdown reduces maximum traction stress of fibroblasts.....	51
3.3.4 Reducing traction force by ROCK inhibition suppresses cellular response to substrate rigidity	52
3.3.5 Vimentin knockdown leads to a reduction in force correlation length	53
3.3.6 Knocking down vimentin reduces directional cell migration	55
3.4 Discussion	57
3.5 Summary	64
Chapter 4: Effects of PTEN loss and activated KRAS overexpression on breast epithelial cells' mechanosensing	65
4.1 Background.....	65
4.2 Materials and Methods	68
4.2.1 Cell Lines	68
4.2.2 Substrates	71
4.2.3 Migration Studies	71
4.2.4 Statistics.....	72
4.3 Results	72
4.3.1 PTEN knockout and KRAS overexpression have opposite effects on cell morphology response to substrate rigidity.....	72
4.3.2 PTEN knockout and KRAS overexpression have opposite effects on cell traction response to substrate rigidity.....	79
4.3.3 Maximum traction stress scales with substrate rigidity in all conditions.	79
4.3.4 PTEN knockout and KRAS overexpression modifies actin cytoskeleton structure and force correlation length.....	79

4.3.5 Combination of KRAS overexpression and PTEN knockout drastically enhances cell directional migration.	82
4.4 Discussion	86
4.5 Summary	92
Chapter 5: Conclusion	93
Chapter 6: Future directions	96
6.1 Effects of Vimentin Knockdown, PTEN knockout and KRAS overexpression on focal adhesion	96
6.2 Dynamic change of cell traction force at the initial stage of cell-substrate contact and during cell migration	98
6.3 Soft gel regime, 3D deformation and cluster studies	100
Reference	103
Appendix	114
Appendix A. Traction Force Microscopy (MATLAB & ANSYS APDL).....	114
A1. Image Preprocess (TFM_Prep)	114
A2. PIV (TFM_disp)	119
A3. Force Reconstruction (TFM_solve)	121
A4. Plots (TFM_Plot)	124
Appendix B. Traction Force Post Analysis (MATLAB)	128
B1. Order Parameter	128
B2. Correlation length.....	129
Appendix C. Time lapse TFM (MATLAB).....	133
C1. Time lapse TFM (TFMTL)	133
C2. Fitting.....	138
Appendix D. Migration Analysis (Python & VBA)	138
C1. Trajectories	138
C2. Displacement and Total Distance	138
C3. Directional Autocorrelation.....	140

List of Figures

- Figure 1. 13
- Figure 2. 14
- Figure 3. 18
- Figure 4. 21
- Figure 5. 24
- Figure 6. 32
- Figure 7. 34
- Figure 8. 35
- Figure 9. 41
- Figure 10. 44
- Figure 11. 48
- Figure 12. 49
- Figure 13. 50
- Figure 14. 51
- Figure 15. 53
- Figure 16. 54
- Figure 17. 56
- Figure 18. 57
- Figure 19. 59
- Figure 20. 60
- Figure 21. 66
- Figure 22. 67
- Figure 23. 70
- Figure 24. 74
- Figure 25. 75
- Figure 26. 76
- Figure 27. 77
- Figure 28. 78
- Figure 29. 81
- Figure 30. 82
- Figure 31. 84
- Figure 32. 85
- Figure 33. 88
- Figure 34. 97
- Figure 35. 99
- Figure 36. 100
- Figure 37. 102

List of Tables

Table 1.....28
Table 2.....94

List of Abreviations

Abbreviation	Explanation
AFM	Atomic force microscopy
AKT	Protein kinase B
APS	Ammonium persulfate
APTMS	3-aminopropyl trimethoxysilane
ATP	Adenosine triphosphate
BEM	Boundary Element Method
Cdc42	Cell division control protein 42 homolog
cmd	Command line
DA	Directional Correlation
DI	Deionized
DOF	Degree of freedom
DPBS	Dulbecco's phosphate-buffered saline
ECM	Extracellular matrix
EMT	Epithelial to mesenchymal transition
ER	Estrogen receptor
ERK1/2	Extracellular signal-regulated kinases 1 and 2
FAK	focal adhesion kinase
FBS	Fetal bovine serum
FEM	Finite Element Method
HEPES	4-(2-hydroxyethyl)-1-piperazineethanesulfonic acid)
HER2	Hormonal epidermal growth factor receptor 2
IF	Intermediate Filament
KRAS	Kristen rat sarcoma viral oncogene homolog
MAPK	Mitogen-activated protein kinase
MEK	Mitogen-activated protein kinase kinase
MT	Microtubule
NPU	Neural Processing Unit
pAKT	Phosphorylated AKT
PDMS	Polydimethylsiloxane
pERK	Phosphorylated ERK1/2
PI3K	Phosphatidylinositol 3-kinase
PIP2	Phosphatidylinositol (4,5)-bisphosphate
PIP3	Phosphatidylinositol (3,4,5)-trisphosphate
PIV	Particle Image Velocimetry
PTEN	phosphatase and tensin homolog

PTEN-/-	PTEN knockout
Rac1	Ras-related C3 botulinum toxin substrate
Ras	Receptor-linked tyrosine kinases
RhoA	Ras homolog family member A
ROCK	Rho-associated kinase
SD	Standard deviation
SEM	Standard error of the mean
shRNA	Short hairpin RNA
shVim	Vimentin Knockdown
Src	Proto-oncogene tyrosine-protein kinase
TEMED	Tetramethylethylenediamine
TFM	Traction force microscopy
TFMTL	Traction force microscopy time lapse
TIRF	Total internal reflection microscopy
VBA	Visual Basic Application
VIF	Vimentin Intermediate Filament

Chapter 1: Background and Introduction

1.1 Mechanosensing

Cells are capable of interacting with their surrounding environments in several ways, one of which involves sensing and responding to mechanical cues such as mechanical force and rigidity of the extracellular matrix. It has been reported that the shape of cells cultured on a soft surface is drastically different from that of cells cultured on a hard surface [1]. The speed, persistence and directionality of cell migration have been reported to increase with increasing substrate rigidity [2]. Matrix rigidity can also modulate mesenchymal stem cells differentiation into either smooth muscle cells or chondrogenic cells [3, 4]. The process by which cells sense mechanical cues is called mechanosensing.

Mechanosensing plays a crucial role in cell differentiation, proliferation/apoptosis, and many other cellular processes [5]. Impairment in cell mechanosensing ability, caused by mutations or misregulation of proteins, contributes to the development and progression of various human diseases, ranging from muscular dystrophies and cardiomyopathies to cancer progression and metastasis [6, 7].

Mechanosensing involves sensor molecules (mechanosensors). These mechanosensors help translate mechanical forces into biochemical signals (mechanotransduction)[8, 9] (Figure 1). A classical example of the mechanosensor system is the mechanosensitive channel. When subjected to force, these mechanosensitive channels undergo a structural change from close state to open state, allowing the exchange of ions between the cell and the surrounding environment. This interaction transduces the mechanical force to electrochemical signals,

providing interpretable information for the cell to respond [10, 11]. For example, bacteria use mechanosensitive channels to sense the conditions of hypo- or hyperosmotic stress in their surroundings and adjust their osmolarity accordingly to avoid lysis [12]. Other than the mechanosensitive channels, the cytoskeleton and cell-ECM adhesions have also been implicated in mechanosensing [8, 9]. The exact molecular mechanisms in mechanosensing and mechanotransduction remain elusive [13-15]. In the next few sections, we will review the cytoskeleton structure, the focal adhesion and their roles in mechanosensing.

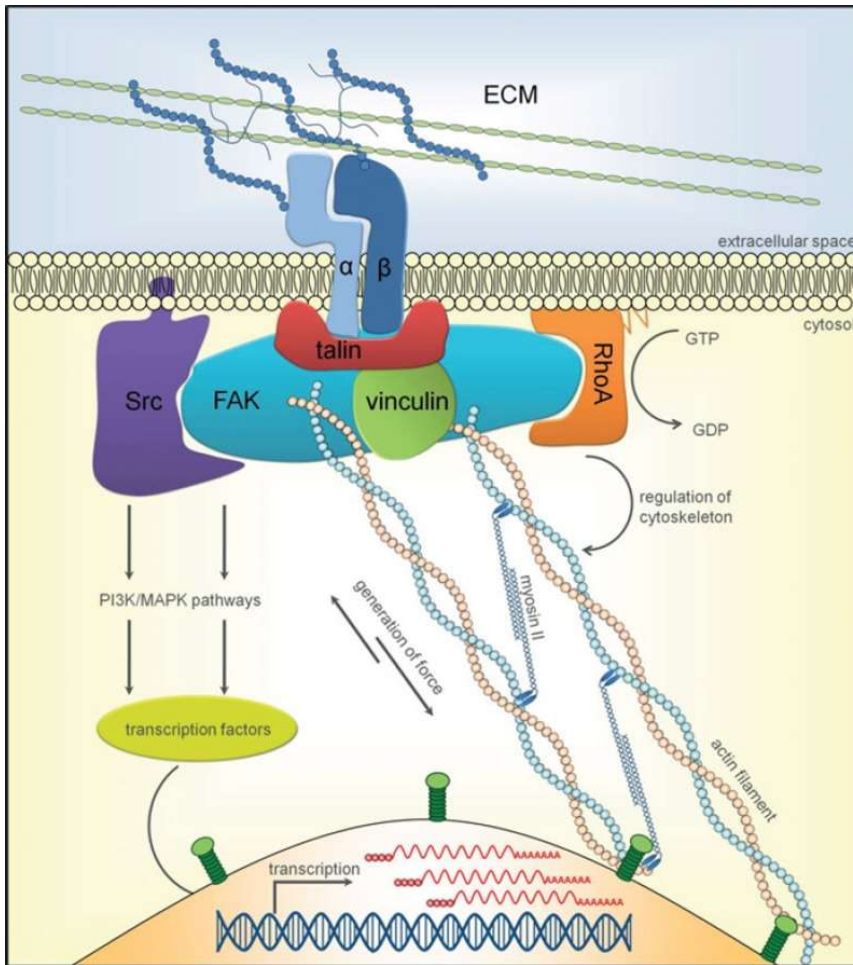


Figure 1. Cell mechanosensing and mechanotransduction. Adapted from [16].

1.1.1 Cytoskeleton

Cytoskeleton is the key for force generation and transmission in cells. The cell cytoskeleton consists of three classes of protein filaments: actin filament (F-actin), microtubules (MTs) and intermediate filaments (IFs). (Figure 2)

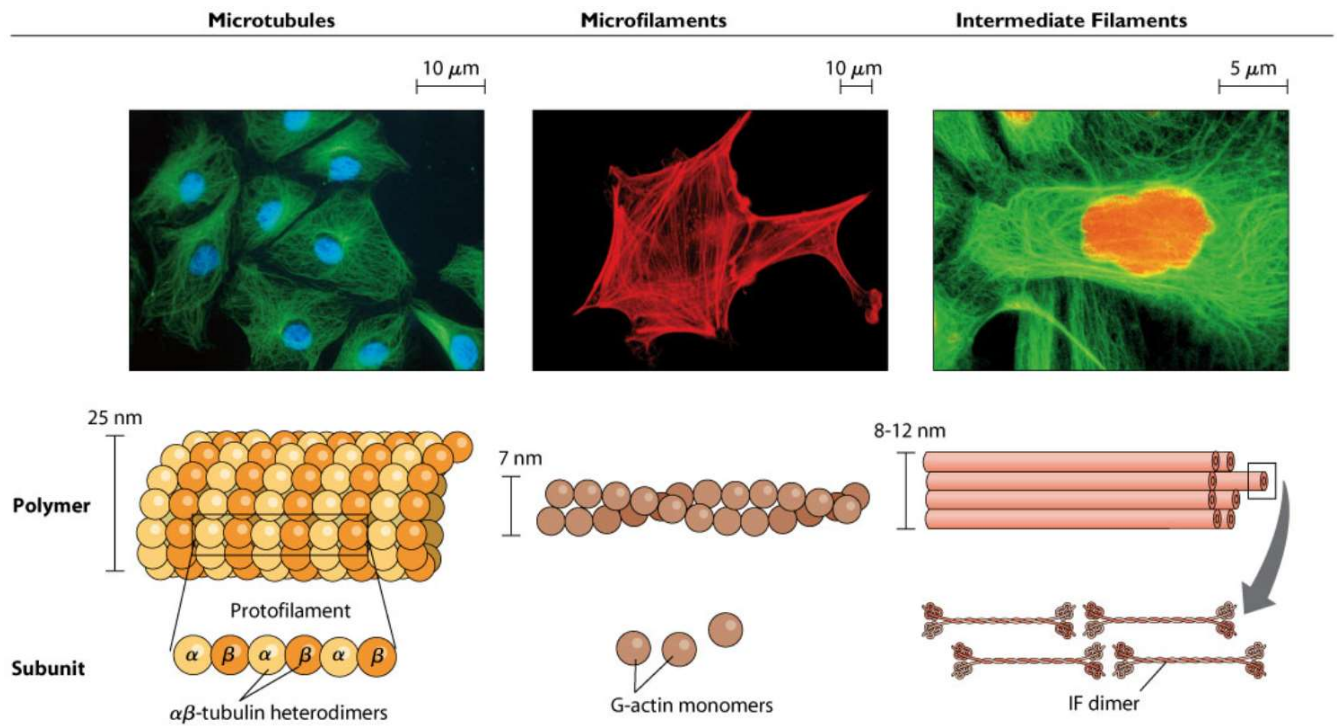


Figure 2. Microtubules, Actin microfilaments, and Intermediate filaments. Adapted from [17].

Microtubules (MTs) are the first principal component of the cytoskeleton and play crucial roles in several cellular activities, including intracellular transport of organelles, mitotic spindle formation, cilium formation and cell polarity formation [18]. MTs are dynamic structures that undergo continual assembly and disassembly within the cell. MTs are composed of a single type of globular protein tubulin, which consists of α and β tubulin heterodimers [18]. In mechanobiology, MTs play an essential role in regulating mechanical force involved in spindle organization, chromosome alignment and segregation in mitosis [19]. MTs are major components of cilia (and flagella), tiny hair-like organelles protruding from the cell surface. Cilia allows cells to sense and transduce various chemical and mechanical signals from the

extracellular environment, suggesting the role of MTs in mechanosensing [20, 21]. However, there is no evidence that MTs function as the mechanosensor directly by themselves.

Intermediate filaments (IFs) are the second principal component of the cytoskeleton and play crucial roles in maintaining cell integrity, polarization and migration [22-24]. IFs are relatively stable filaments compared to actin filaments and MTs [25]. Intermediate filaments are composed of a variety of proteins expressed in different types of cells, unlike actin microfilaments and microtubules, which are composed of a single type of protein (actin and tubulin, respectively). IF proteins are classified into six groups, type I-VI, based on similarities between their amino acid sequences [26]. Canonically intermediate filaments have been shown to interact with cell adhesions indirectly by modifying the stability of actin-linked focal adhesions [27, 28]. However, novel evidence indicates that intermediate filaments are physically linked to these various adhesion complexes [29, 30]. For example, vimentin intermediate filaments interact with integrins either directly by binding to $\beta 3$ integrin tail or indirectly via linker proteins, including plectin [31]. This vimentin-adhesion regulates the size and adhesive strength of focal adhesions. The affiliation of IFs with actin and focal adhesion implies that IFs are likely involved in mechanotransduction. However, it has not been demonstrated whether or not IFs function as a mechanosensor on their own. Additional studies are required to understand the molecular mechanisms underlying IF-mediated mechanosensing.

Actin microfilaments are the third principal component of the cytoskeleton structure and have a fundamental role in various cellular processes such as cell migration, morphogenesis, cytokinesis, endocytosis and phagocytosis [32]. The actin cytoskeleton consists

of filamentous actin (F-actin) and globular actin subunits (G-actin). Similar to microtubules, actin filaments constantly undergo assembly and disassembly inside the cell. The meshwork consists of actin filaments that are attached to the cell membrane and to each other.

Many motor proteins can bind to cytoskeletal filaments. Myosin is a class of motor protein that binds to actin. The interaction between myosin and actin causes actin filaments to slide past each other and leads to contraction of the cytoskeleton. This actomyosin interaction is the major source of force generation inside cells.

1.1.2 Stress fibers in mechanosensing

Stress fiber refers to the bundles of F-actin in cells. The actin filaments in stress fibers are crosslinked together by α -actinin and myosin motors. Stress fibers play a critical role in mechanosensing by providing a basic structure for the generation and propagation of force, which enables cells to probe the extracellular properties [33, 34]. In a stress fiber, each myosin motor binds to two antiparallel actin filaments, slides the filaments against each other, and generates tension in the stress fiber. Stress fibers are often anchored to focal adhesions at the cell–substrate contact sites. The contractile force generated by stress fibers regulates the assembly and dynamics of focal adhesions, through which cells acquire a “sense of touch” on substrates [35]. The stress fibers also facilitate the transmission of force to other mechanosensors besides focal adhesion. It has been reported that stress fibers transmit force to the cell membrane to open the mechanosensitive ion channels and allow cells to sense the force from optical tweezers [11].

In addition to transmitting force to the cell-ECM boundary, stress fibers also directly regulate mechanotransduction inside the cytoskeleton and the cell nucleus. It has been reported that stress fibers affect the translocation of YAP/TAZ between the cytoskeleton and nucleus, leading to increased transcription of genes related to cell proliferation and differentiation [36].

1.1.3 Focal adhesion

Focal adhesions (FAs) are large macromolecular assemblies which consist of clusters of proteins including integrins, talin and vinculin, connecting the cytoskeleton to the extracellular material [35, 37, 38] (Figure 3). Focal adhesion also plays a vital role in mechanosensing. It provides a basic structure that allows cells to apply traction force to ECM and to transmit extracellular force to the intracellular components. Integrins are heterodimers composed of an α and β subunit that bind to the ECM by forming the integrin-ligand bonds with ECM's macromolecules such as collagen, fibronectin or laminin [39]. The intricate connection between ECM ligand, integrin, focal adhesion proteins and actin cytoskeleton allows the cells to directly transmit intracellular contractile force generated by actin-myosin activity onto ECM as traction force.

Focal Adhesion

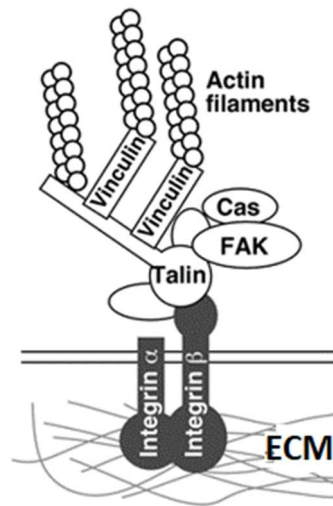


Figure 3. Focal adhesion. Adapted from [40].

The formation of a focal adhesion starts from the single integrin-ligand bond. The binding of an integrin to ECM ligand triggers a series of intercellular events that result in the formation of focal adhesion [41]. Following the binding of integrin-ligand, recruitment of adhesion proteins to the adhering site through intracellular signaling and phosphorylation [38] results in a stronger bond between the cell and the surface. These newly reinforced integrin-ligand bindings are called focal complexes and are typically located at the leading-edge of cellular movement as the cell explores the surrounding microenvironment [42]. With further recruitment of focal adhesion proteins, the focal complex grows to a fully mature focal adhesion, allowing cells to firmly anchor to the ECM. During cell migration, the polarized intracellular signals promote focal adhesion assembly at the leading-edge and result in focal adhesion disassembly at the trailing edge of the cell [43].

Many focal adhesion proteins are potential mechanotransducers, which transduces mechanical signals into biochemical signals through force-induced conformational changes. The

role of talin and vinculin complex in transducing mechanical signals in focal adhesion has been studied in recent years [44-46]. Talin links integrins to actin stress fibers at FAs. Talin has multiple vinculin-binding sites (Figure 3). These vinculin-binding sites of talin are usually folded in a latent state, but become active by applying tensile force [47, 48]. This association of vinculin to talin triggers a series of intercellular processes that regulate cell migration, growth, and proliferation [49]. These suggest that talin can transduce mechanical signals through its force-dependent binding to vinculin. Force also induces conformational changes from low-affinity to high-affinity state in integrins such as $\alpha_{IIb}\beta_3$, $\alpha_V\beta_3$, etc. [50, 51]. Furthermore, forces exerted on focal adhesions can activate tyrosine-protein kinase (Src) and focal adhesion kinase (FAK) to stimulate the growth of the adhesions [52, 53].

1.2 Mechanosensing in cancer

Cancers are a large group of diseases that are usually associated with abnormal cell growth which has the ability to invade and spread to other parts of the body. All cancer cells exhibit one of the six hallmarks of cancer: sustaining proliferation signaling, resisting apoptosis, inducing angiogenesis, evading growth suppressors, enabling replicative immortality and activating invasion and metastasis [54]. Metastatic spread of the primary tumor accounts for over 90% of patient mortality associated with solid cancers [54-56]. Despite this, research into the process of cancer metastasis and the factors governing cancer spread and establishment at secondary locations is still lagging behind other hallmarks of cancer such as proliferation, apoptosis, angiogenesis, etc. [57]. Hence, furthering our understanding of the processes that lead to metastasis is crucial for developing treatments that could slow down or prevent the metastasis from happening.

1.2.1 Epithelial-mesenchymal transition

Healthy cells acquire metastatic behavior through a chain of events called malignant cell transformation. A key event in such transformation is the developmental regulatory program, referred to as the epithelial-mesenchymal transition (EMT)(Figure 4). EMT is canonically associated with several developmental processes such as mesoderm formation during gastrulation [58], neural crest and somite development [59] as well as fibrosis and wound healing [60]. However, it has become prominently implicated in the process of cancer cells acquiring the ability to invade and resist apoptosis [61]. In this process, a cell of epithelial phenotype which typically resides within the tumor bulk and is involved in unregulated proliferation and strong cell-cell adhesion transform into a mesenchymal phenotype characterized by loss of cell-cell adhesion, increased cellular polarity, high expression of actin stress fibers, and enhanced migratory and invasive properties [62]. As such, the process of EMT that enables the invasive, tumorigenic phenotype represents a key interest in cancer research.

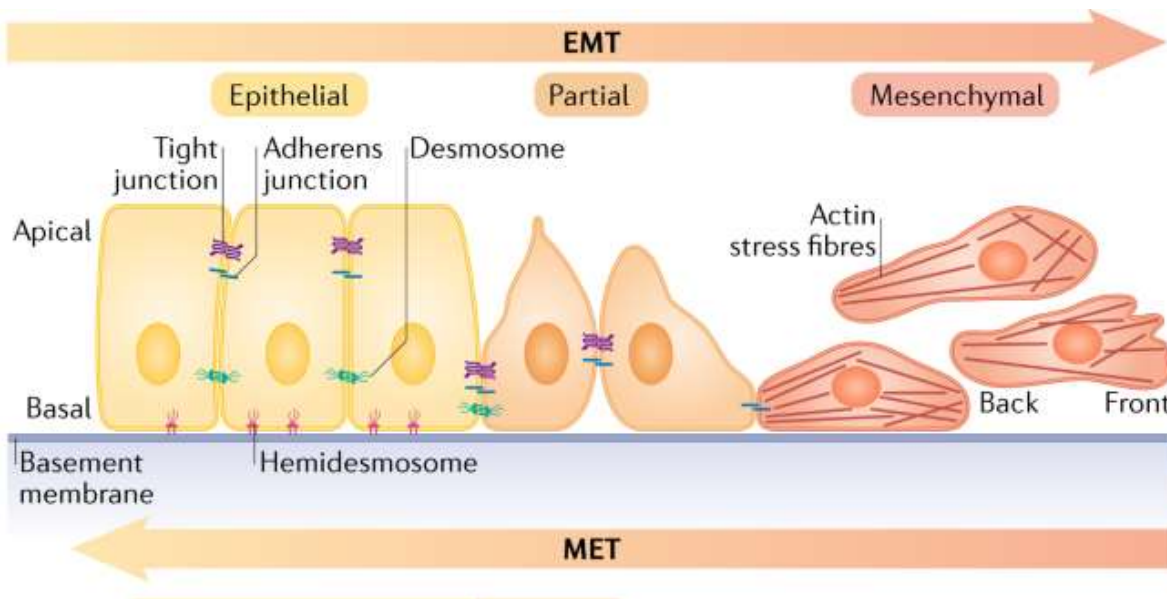


Figure 4. Epithelial to Mesenchymal Transition in cells. Adapted from [63]. In this process, a cell of epithelial phenotype which typically resides within the tumor bulk and is involved in unregulated proliferation and strong cell-cell adhesion transform into a mesenchymal phenotype characterized by loss of cell-cell adhesion, increased cellular polarity, high expression of actin stress fibers, enhanced migratory and invasive properties.

1.2.2 Mechanosensing of cancer cells

Can cancer cells sense mechanical cues? On one hand, melanoma cells have shown insensitivity to matrix rigidity [64]. Some cancer cells can maintain high proliferation rates even in low adhesion environments [65]. On the other hand, several cancer cells - including breast, lung and prostate cancer cells - demonstrated rigidity sensing ability [66]. Furthermore, mechanosensitivity is greatly decreased in less-metastatic ovarian cancer cells [67]. Generally, alterations in ECM rigidity and geometry coupled with one or several oncogenic mutations are crucial to induce normal cells to adopt phenotypes characteristic of transformed and/or metastatic cells [68-73]. For example, stiffer substrates promote increased cellular traction

leading to more mesenchymal, invasive phenotypes [66, 74]. Reduced tension in the ECM with laser ablation [75, 76] reverts cell invasiveness. Intrinsically, this implicates the involvement of cell mechanical sensing and adaptation with EMT, which regulates the process of enabling cells to switch to a more invasive and tumorigenic phenotype.

Furthermore, mechanosensing is also heavily implicated in cancer progression intracellular signaling pathways. For example, in response to an increase in tension in focal adhesion, increases in integrin clustering and the phosphorylation of focal adhesion kinase (FAK) occur, which downstream initiates the activation of Rho-family GTPases, such as RhoA. RhoA activation stimulates actin remodeling and induces protein phosphorylation to promote cell survival [77, 78]. Others integrin-dependent signaling pathway that is indirectly implicated in response to mechanical force stimuli are the mitogen-activated protein kinase/extracellular signal-regulated kinase (MAPK/ERK) pathway, the phosphatidylinositol 3 kinase/v-akt murine thymoma viral oncogene (PI3K/AKT) pathway due to their upstream activator focal adhesion kinase (FAK). These pathways have been implicated in several types of cancers and they regulate cell proliferation and cell differentiation [79]. Hence, studying the effects of altering these protein expressions on mechanosensing could provide potential pharmacological targets to reduce the invasiveness of cancer cells.

1.2.3 Vimentin in cancer

Vimentin is a Type III intermediate filament protein expressed in the cells and tissues of many different organisms [80]. During EMT, intermediate filaments undergo a significant compositional change: epithelial cells, which normally express only keratin IFs, initiate the

expression of vimentin IFs (VIFs). Because of this dramatic change in IF composition, VIF expression has become a canonical marker of the EMT [60, 61, 81] (Figure 5). Microinjection or transfection with vimentin induces mesenchymal phenotype coincident with VIF assembly in epithelial cells in vitro. The reorganization of VIFs caused by negative mutation or by silencing vimentin with shRNA (neither of which alter microtubule or microfilament assembly) causes mesenchymal cells to adopt epithelial shapes [22, 82]. While vimentin is not directly involved in mechanosensing, vimentin is heavily involved with focal adhesions and cytoskeletal structures. Vimentin has been observed to be transported by microtubule-dependent motor proteins towards the cell periphery [83, 84]. The vimentin has been reported to bind with actin both directly [85] and via cross-linking proteins such as plectin [86]. Vimentin has also been associated with mature focal adhesions [87]. Vimentin can bind directly to the integrin $\alpha 2\beta 1$ and it is enriched in integrin- $\beta 1$ -containing focal adhesions [88]. Despite this, the functional implications of vimentin expression in EMT with respect to mechanobiology are poorly understood. Understanding how vimentin regulates cells' mechanosensing process could uncover the role of vimentin expression in EMT, potentially leading to the utilization of vimentin expression as a therapeutic target in metastasis inhibition.

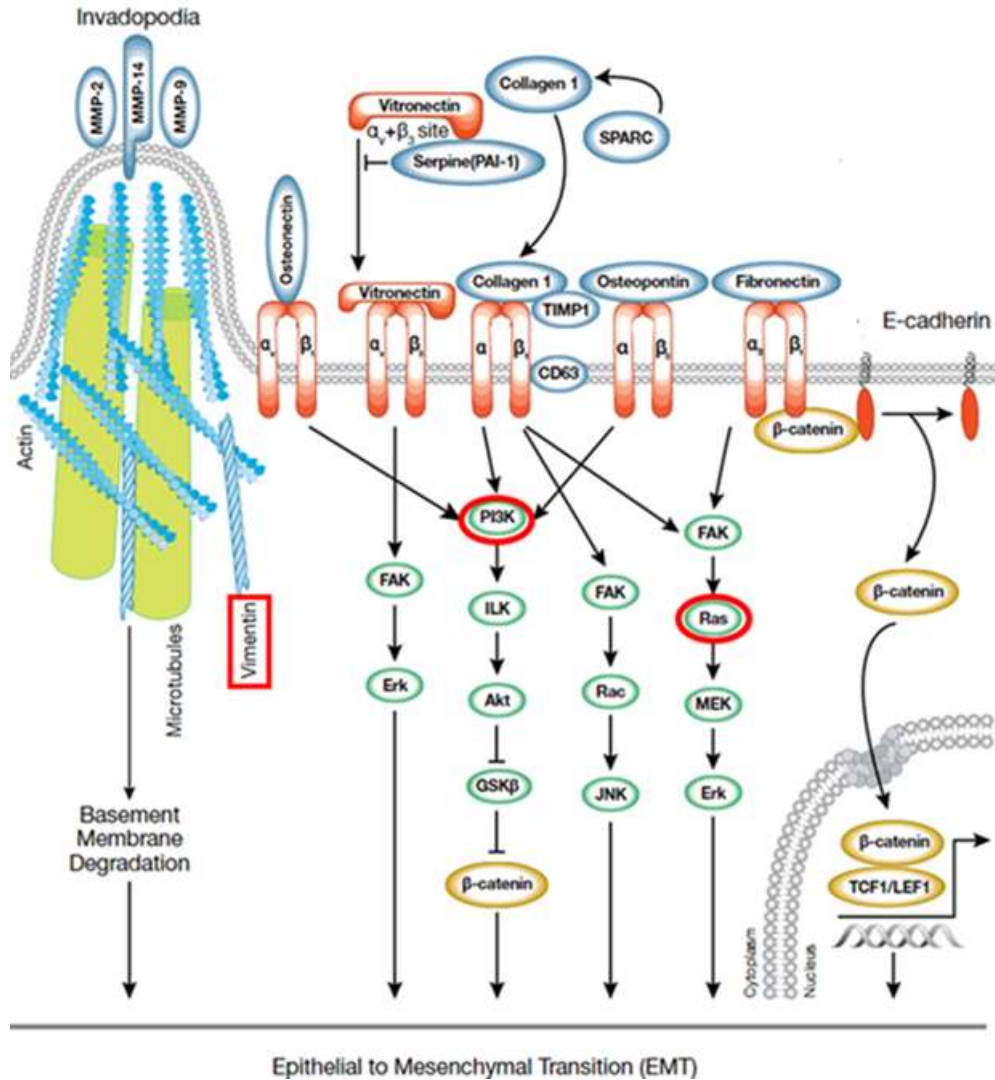


Figure 5. Contribution of Extracellular Matrix to EMT. Adapted from [89]. Components of interest are highlighted by bold, red boxes: Vimentin, PI3K and Ras.

1.2.4 PI3K/AKT and Ras/MAPK pathway in cancer

Phosphatidylinositol 3-kinase (PI3K) is a key regulatory protein involved in a wide variety of cellular processes such as cell growth, proliferation, and differentiation [90]. PI3K expression is implicated in multiple aspects of tumorigenesis. In particular, the PI3K/AKT signaling pathways can induce EMT directly [91] or through cooperation with various other signaling pathways [92] (Figure 5). PI3K has also been shown to be directly involved in reorganization of

actin cytoskeleton through activated AKT in chicken embryo fibroblast [93], implicating its' involvement with mechanosensing and migration. Phosphatase and tensin homolog (PTEN) is a protein that antagonizes the expression of PI3K [90]. Knocking out PTEN is a common methodology to upregulate the PI3K pathway [90, 94]. In fact, PTEN is one of the most frequently mutated tumor suppressor genes in human cancer and has been extensively studied in breast, thyroid, kidney and endometrial cancer models [95, 96].

The mitogen-activated protein kinase (MAPK) signaling pathways are important mediators of many cellular functions such as cell proliferation, meiosis, cell death, differentiation, secretion, migration, and tissue development [97]. The MAPK/ERK (also known as MEK/ERK) signaling pathway is the most important signaling cascade among all MAPK signal transduction pathways and plays a crucial role in EMT and tumorigenesis [98] (Figure 5). MAPK/ERK pathway is also implicated in mechanosensing due to its involvement with focal adhesion kinase (FAK) [99] as well as small GTPases Rac1 and Cdc42 [100] which regulate actin cytoskeleton dynamics. MAPK signaling pathways can be activated via mutation in the receptor-linked tyrosine kinases (Ras) subfamily, most notably H-Ras (HRAS) and K-Ras (KRAS) [101]. Mutations in Ras (mainly KRAS) are the most common mutations in cancer, appearing in approximately 30% of all cancer types [102] and in 10% of all patients with cancer [103].

In many cancers, the PI3K/AKT and MAPK/ERK pathways are concurrently activated [104]. The interplay between these two signaling pathways results in complications in drug study which targets each individual pathway using a linear signaling conduit model (monotherapy) [105, 106]. For example, a metastatic phenotype of the triple-negative cancerous breast cell line MDA-MB-231 LM2 exhibits high migratory behavior due to

overactivation of Ras/MAPK pathway. However, inhibition of Ras/MAPK pathways with the downstream rho-associated kinase (ROCK) inhibitor LY2940029 is ineffective. Migratory potential was unaffected and regulated through the new overactivation of the PI3K/AKT pathway. This invasive behavior is only prohibited when the Ras/MAPK and PI3K/AKT pathways were simultaneously inhibited [107]. This study indicates a significant pathway integration between the PI3K and Ras/MAPK either through cross-activation or cross-inhibition of upstream or downstream signaling components when it comes to metastatic potential [105]. Additional study on the crosstalk between the PI3K and Ras/MAPK pathways is needed to develop a proper understanding of this crosstalk and its role in metastasis.

Chapter 2: Method overview

2.1 Traction Force Microscopy

2.1.1 Background

Measuring cellular forces applied on the surrounding environment is an essential tool to study mechanosensing and migration quantitatively. We typically quantify force through force measurement systems, which use a force sensor and a measuring instrument. The force sensor is a physical device that converts force to a physical quantity that can be measured directly by a correlated instrument. A simple example of such device is the Newton's dynamometer, whereby a spring (force sensor) translates the weight of an object into length deformation measured by a ruler (measuring instrument). In cell biology, we utilize a similar force measuring system in which measurable physical quantities such as mechanical deformation or light intensity can be used to quantify the cellular force once the force sensor's mechanical/material properties are known. A few popular examples of those are traction force microscopy in 2D and 3D [108, 109] – utilizing deformation of substrate; micropillars – utilizing the displacement of pillars [110]; cantilevers – utilizing the deflection of cantilever [111]; or molecular sensors – utilizing the changes in fluorescent intensity [112]. A comparison of these systems is summarized in table 1 below.

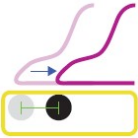
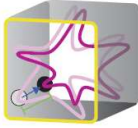
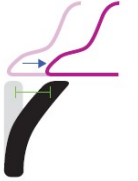
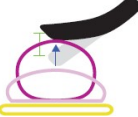
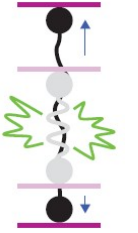
	Force range	Length scale	Measured quantity	Advantages	Limitations	Schematic
2D TFM	1–10 ⁴ Pa	10 ⁻¹ –10 ³ μm	Substrate displacement	-Tunability of substrate rigidity -Output is a 2D map	-Computationally involved -High sensitivity to displacement noise	
3D TFM	10–10 ⁴ Pa	10 ⁻¹ –10 ² μm	ECM displacement	-Cells in 3D environment -Output is a 3D map	-Computationally very involved -Unknown ECM material properties close to the cell -Physiological ECM is non-linear	
Micropillars TFM	10 ⁻² –10 ² nN	10 ⁻¹ –1 μm	Pillar displacement	-No reference images required -Simple force calculation	-Discrete rather than continuous adhesion -Difficult to compare to physiological environments -Small rigidity range	
Cantilevers	10 ⁻² –10 ² nN	10 – 10 ³ μm	Cantilever displacement	-No reference image required. -Force measurements in real time	-Requires contact -Low throughput	
Synthesized molecular sensors	1–100- pN	1–10nm	Fluorescence signal	-Higher force resolution	-Only available for extracellular ligands	

Table 1. Comparison of several popular cellular force quantification in vitro. Adapted from [113].

Traction force microscopy maps traction stresses at the cell surface by measuring the deformation of the underlying substrate. As adherent cells exert tractions on their surroundings, if the substrate is sufficiently soft, deformation of the substrate caused by the

cell can be measured and solved for cell traction force/stress [109]. The advantage of using TFM to probe for cellular force comes from how the adjustable elastic properties of the substrate don't restrict cell-matrix adhesion contacts. The disadvantage of traction force microscopy has been vastly improved in the past decades through better computing capabilities (for numerical solution) [108, 114, 115], usage of regularization factors (for analytical solution) [116] and advances in image acquisition (noise reduction) [108].

2.1.2 Principle of traction force microscopy

The basic principle of traction force microscopy is based on the deformation gradient in continuum mechanics [117-119]. In summary, a material point undergoing deformation from location \mathbf{x} to \mathbf{x}' can be represented by its displacement $\mathbf{u}(\mathbf{x})$ by: $\mathbf{x}' = \mathbf{x} + \mathbf{u}(\mathbf{x})$. Differentiating both sides with respect to \mathbf{x} gives us:

$$\nabla \mathbf{x}' = \nabla(\mathbf{x} + \mathbf{u}(\mathbf{x})) = \mathbf{I} + \nabla \mathbf{u}(\mathbf{x}) = \mathbf{F} \quad [1]$$

Here \mathbf{I} is the identity matrix and \mathbf{F} is the deformation gradient tensor, which is the Jacobian of the coordinate transformation from the undeformed state \mathbf{x} to the deformed state \mathbf{x}' . The Lagrangian strain tensor gives us:

$$\mathbf{E} = \frac{1}{2}(\nabla \mathbf{u} + (\nabla \mathbf{u})^T + \nabla \mathbf{u}(\nabla \mathbf{u})^T) \quad [2]$$

With small strain and assumed linear elasticity, we can simplify the strain tensor to:

$$\boldsymbol{\varepsilon} = \frac{1}{2}(\nabla \mathbf{u} + (\nabla \mathbf{u})^T) \text{ or in components form: } \varepsilon_{ij} = \frac{1}{2}\left(\frac{\partial u_i}{\partial x_j} + \frac{\partial u_j}{\partial x_i}\right).$$

From here, force can be found by direct TFM or inverse TFM (Figure 6). In direct TFM, the material is approximated by the Neo-Hookean material model [120]. This approach requires determination of the material's true stress tensor, or Cauchy stress σ ; which demands highly precise image acquisition, image processing and material properties of the cell-matrix interface region [108]. In inverse TFM, we assume that if the substrate material has a linear and isotropic constitutive relation (material linearity), then a linear relation exists between the strain tensor ϵ and the stress tensor σ describing the forces acting over internal surfaces:

$$\sigma_{ij} = \frac{E}{1+\nu} \left(1 + \frac{\nu}{1-2\nu} \epsilon_{uu} \delta_{ij}\right) \quad [3]$$

Here E and ν represent the Young modulus and Poisson ratio of the linear and isotropic substrate. Combining equation 2, equation 3 and the balance of internal and body forces $\nabla \sigma = \mathbf{f}$, we get the Lamé equation:

$$\frac{E}{2(1+\nu)} \Delta \mathbf{u} + \frac{E}{2(1+\nu)(1-2\nu)} \nabla(\nabla \cdot \mathbf{u}) = \mathbf{f} \quad [4]$$

Numerically equation 4 can be solved with FEM, realizing that it is of the form:

$[K]\{u\} = \{F\}$, where $[K]$ is the global rigidity matrix (governed by material properties), $\{u\}$ is the nodal displacement vector and $\{F\}$ is the nodal force [115]. This form can be further expanded in terms of with equilibrium condition in terms of sub-matrices and sub-vectors as [114]:

$$\begin{Bmatrix} [K_{cc}] & [K_{cs}] \\ [K_{cs}]^T & [K_{ss}] \end{Bmatrix} \begin{Bmatrix} \{u_c\} \\ \{u_s\} \end{Bmatrix} = \begin{Bmatrix} \{F_c\} \\ \{F_s\} \end{Bmatrix} \quad [5]$$

Here subscript s denotes degrees-of-freedom (DOF) where displacements are known; and subscript c denotes the rest of the DOFs where the forces are known. By enforcing several boundary conditions [115]:

1. $u_i = u_i^*$ at the top plane (interface plane between cell and gel);
2. $u_i = 0$ at the bottom plane (interface plane between gel and glass);
3. $\sigma_{ij}n_j = 0$ otherwise (at the side planes) and
4. all nodal force outside cell boundary is 0

where u_i^* = measured displacement at the top surface between the cell and substrate, n_j = surface normal vector at the side planes (planes except top and bottom) we have:

$$\begin{Bmatrix} [K_{cc}] & [K_{cs}] \\ [K_{cs}]^T & [K_{ss}] \end{Bmatrix} \begin{Bmatrix} \{u_c\} \\ \{u_s\} \end{Bmatrix} = \begin{Bmatrix} \{0\} \\ \{F_s\} \end{Bmatrix} \text{ and thus get the nodal solution [114]:}$$

$$\{u_c\} = [K_{cc}]^{-1}(-[K_{cs}])\{u_s\} \text{ and } \{F_s\} = (-[K_{cs}]^T[K_{cc}]^{-1}[K_{cs}] + [K_{ss}])\{u_s\}$$

Equation 4 can be solved analytically through Green's function [33, 109, 121]. For infinite halfspace and elastic layer of finite thickness, the Green's functions to solve equation 4 are known, called Boussinesq solution [122]. The solution can be obtained in real space using the Boundary Element Method (BEM) [123, 124] or the Adjoint Method – traction force reconstruction with point force (TRPF) [125] or in Fourier space using the Fourier Transform Traction Cytometry (FTTC) [119].

For this study, we utilize the FEM method to solve for force from deformation tracked by beads displacement on the surface of an elastic gel. While FEM is computationally more expensive than Green's function methods, FEM has the advantage that it can be adapted to model complex geometries, large deformations and governing equations. Furthermore, with advances in parallel and asynchronous computing, the computation time has significantly reduced for FEM. Thus, FEM is the only method that has been readily used to solve 3D-TFM

problems (aside from direct TFM), where complex cell boundaries prevent the use of analytical solutions to the elasticity equations in the traction force reconstruction process [108, 114, 115].

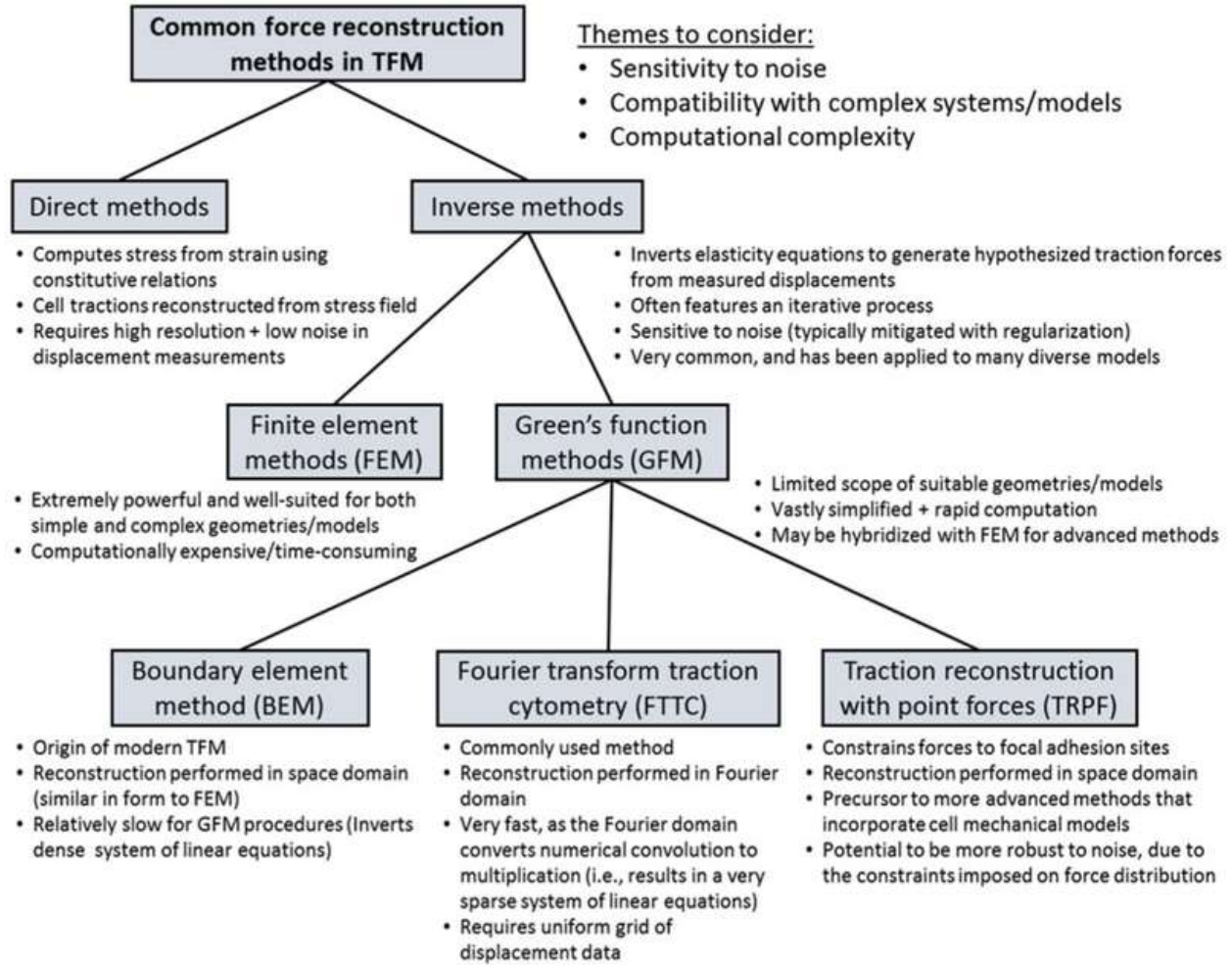


Figure 6. Common traction force framework to for reconstruction of force from material deformation. Adapted from [117].

2.1.3 Procedure of TFM

Flowchart and demonstration of the traction force microscopy experiment are shown in Figures 7 and 8. In our experiment, we use polyacrylamide gel coated with a single layer of fluorescent beads as a substrate for TFM (see **Section 2.2 Substrate Preparation** section for

more information). Polyacrylamide gel has elastic properties suitable for traction force experiments [126]. Rigidity of the gel is characterized using atomic force microscopy. Next, the gel is coated with collagen to ensure attachment of cells to the substrate. Afterward, we measure the deformation \mathbf{u} caused by the cell by comparing two images of fluorescent beads on the gel surface. The first image is obtained when the cell is applying a force on the substrate (loaded image) and the second when the substrate is fully relaxed (unloaded image or reference image) when the cell is detached from the surface by trypsinization. In addition, a phase contrast image is taken to obtain the cell boundary. Bead displacement before and after trypsinization was compared using particle imaging velocimetry (PIV) software in MATLAB (The MathWorks, Natick, MA; <http://www.oceanwave.jp/software/mpiv/>). The working principle of PIV is described in detail in [127]. In short, images before and after are sub-divided in small interrogation windows and the corresponding image samples within each interrogation window are cross-correlated. For each pair of interrogation windows f_1 and f_2 , the cross correlation coefficient is calculated using Minimum Quadric Differences (MQD) algorithm [128] :

$$C(\Delta x, \Delta y) = \sum_{i=1}^N \sum_{j=1}^N |f_1(x_i, y_j) - f_2(x_i + \Delta x, y_j + \Delta y)|$$

, which calculates the pixel value differences between the search windows within the interrogation windows. The displacement of the particle images ensemble within each interrogation window is determined by estimating the location of the MQD minimum value.

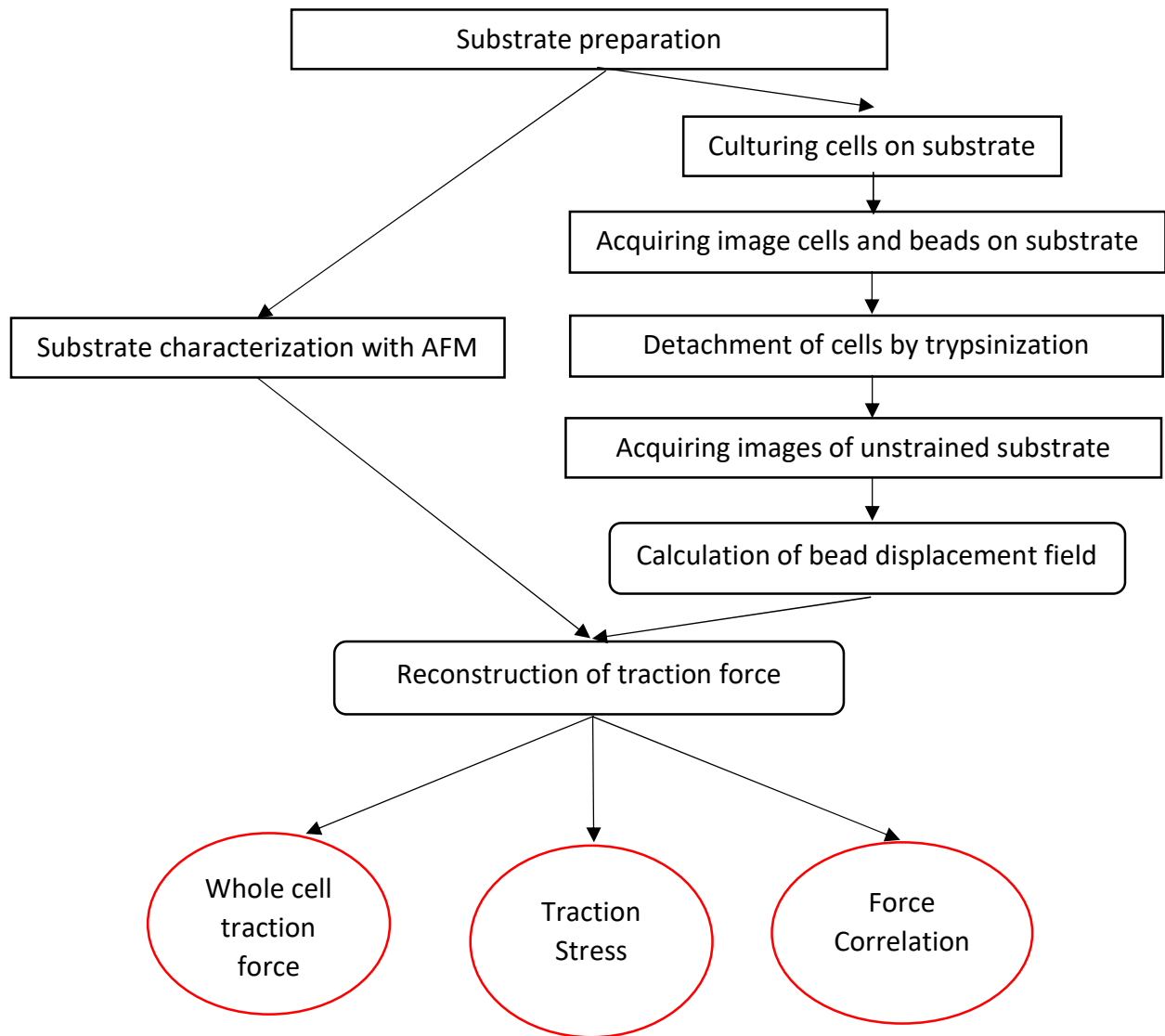


Figure 7. Pipeline of traction force microscopy experiment and output.

The displacement field is then used to reconstruct the traction stress using finite element method (FEM) [118]. ANSYS Mechanical APDL (ANSYS, Canonsburg, PA) was used to create a computational mesh (typically 32x32 pixels) and elastic substrate model. Gel information such as width, length, thickness, Young modulus and Poisson's ratio is specified. Nodal traction force $\{F\}$ is then solved on the surface layer using model constructed and nodal displacements $\{u\}$ found with PIV. From the result of FEM, we can directly obtain two

parameters: traction force and stress apply at each node specified in the constructed model [119]. With cell area and boundaries specified, total traction force applied by the whole cell and maximum traction stress can be readily calculated. Average stress can also be calculated by dividing the total traction force applied by the cell area. In addition to these quantities, we also attempt to calculate the traction force persistence of the cell via force correlation length value.

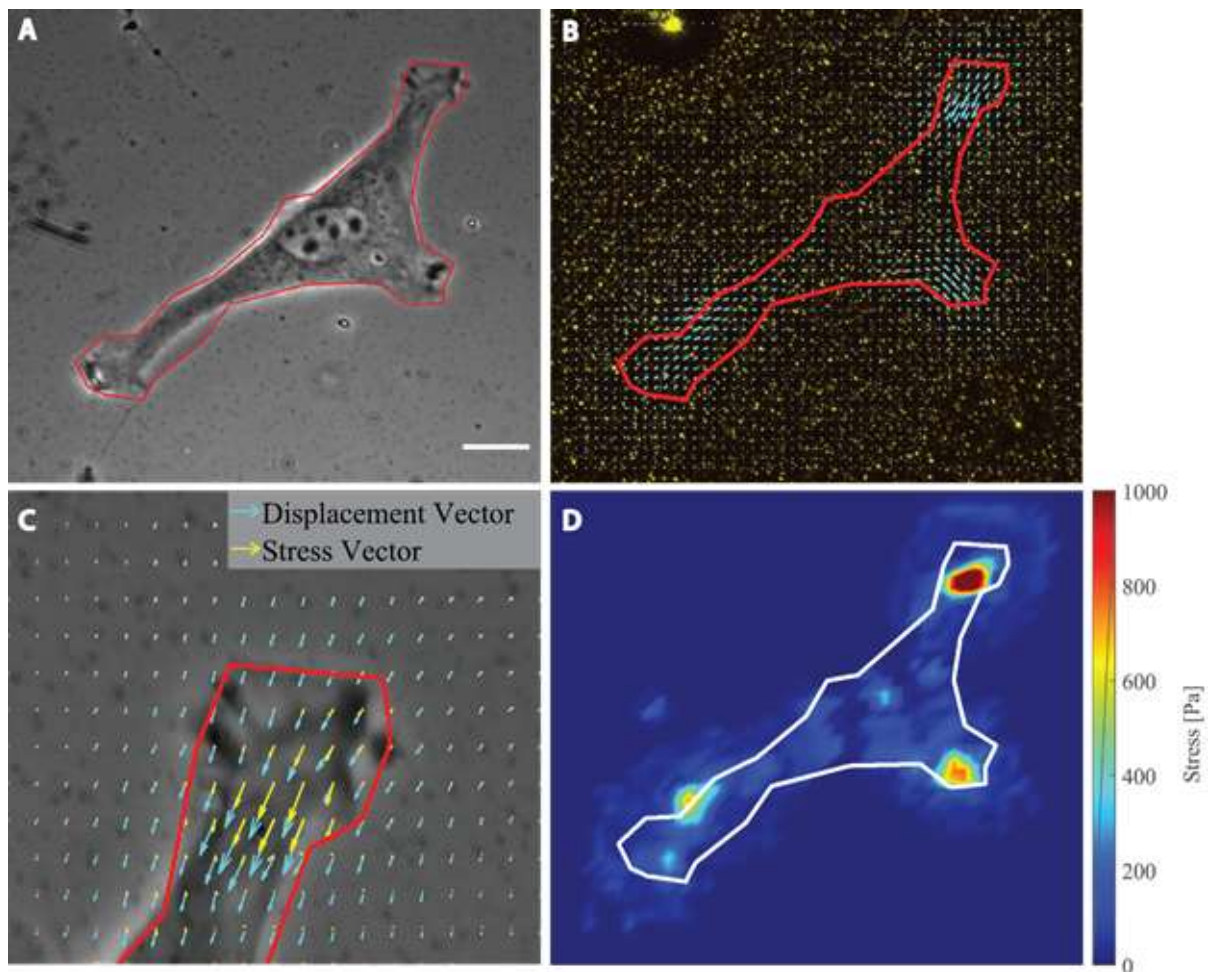


Figure 8. Demonstration of traction force microscopy. A: Phase contrast image of a normal 3T3 fibroblast with cell trace. B: Fluorescent beads image overlay with displacement field plot. C: Enlarged displacement field and the stress field. D: Heat map of stress distribution. Scale bar =

10 μm .

2.1.4 Calculation of Force correlation length

From the stress map from post TFM analysis for each cell, we first normalized each traction stress vector to its magnitude. Then we calculated the average dot product of the normalized traction stresses as a function of distance between the two stress vectors. The result can be plotted to show the correlation of force over distance. A demonstration of this force correlation plot is shown in Figure 16. A cell with lower force correlation will have a faster decay in the force correlation plot. From this correlation plot, the force correlation length can be extracted by fitting the correlation curve to the persistence length equation: $\langle \vec{a}_i \cdot \vec{a}_j \rangle = \langle \cos\theta_{ij}(r) \rangle = C e^{-\frac{r}{L_p}}$ where $\langle \cos\theta_{ij}(r) \rangle$ is the average of the dot product of all normalized vector pairs i, j with the same distance r between them; L_p is the force correlation length (length of persistence). Correlation length can be understood as the length over which correlations in the direction of the force vectors' tangent are lost [129]. By comparing correlation length, we can understand how traction force is transmitted on different cell lines and gain insight on the differences in cytoskeleton organization.

2.2 Substrate Preparation

The procedure for preparing the polyacrylamide substrate was adapted from the protocol described in Gardel *et. al* [130]. 25x25 mm glass coverslips (VWR, Radnor, PA) were cleaned and silanized with 1% 3-aminopropyl-trimethoxysilane solution (Alfa Aesar, Haver Hill, MA) for 10 minutes and then treated with 0.5% glutaraldehyde (Amresco, Solon, OH) before being attached to the culture dish. Next, 18 mm round glass coverslips (VWR) were plasma cleaned and coated with 0.2 μm fluorescent beads (Life Technologies, Carlsbad, CA) on the

surface. Solutions of 3-14% acrylamide (Bio-Rad, Hercules, CA) and 0.03-0.15% bis-acrylamide (Bio-Rad) were mixed in HEPES solution (Amresco, Solon, OH) to a final volume of 500 μ l which were used to prepare polyacrylamide gels with rigidity ranging from 800-40000Pa. The solution was then initiated with 5 μ l of 10% ammonium persulfate (Amresco) and 1.5 μ l of N,N,N',N'-tetramethylethylenediamine (Amresco). Immediately after initiation, 25 μ l of the solution was pipetted onto the bead-coated 18 mm glass coverslip and the coverslip was then applied on top of the 25x25 mm glass slide. After 15 minutes, the gel was immersed in HEPES solution for 30 minutes before the 18 mm glass coverslip was peeled off. The substrate has now been polymerized with a thin layer of 100-nm fluorescent microbeads on the surface. The gel's surface was then cross-linked with 0.1mg/ml collagen type I (Gibco) using sulfo-SANPAH (G-Biosciences, St. Louis, MO). The gels were then incubated in culture medium for 30 minutes before cells plating. Traction force microscopy experiments were performed within 12 to 16 hours after plating.

2.3 Imaging System

Phase contrast images of the cells were taken with 40x objective on an IX3 Olympus microscope (Olympus, PA) equipped with a QIClick CCD camera (QImaging, BC, Canada), using SlideBook software (Intelligent Imaging Innovations, CO). Fluorescent images were captured on the same system with the addition of a L200 mercury and halogen fluorescent lamp (Prior Scientific, MA).

2.4 Additional Analysis

2.4.1 Cell Spreading Area and Cell Polarity

Part of a cell mechanical response to the surrounding environment is reflected through their cell morphology [5]. As a result, a simple test for mechanosensitivity can be done by characterizing the spreading area and cell polarity changes as a function of rigidity. After different groups of cells were seeded on substrates of different rigidity, cell boundaries were traced from either phase contrast or fluorescent images using the Freehand/Wand selections tool and thresholding in Fiji, a distribution of open-source software ImageJ [131, 132]. The area enclosed by the cell boundary gives us the cell spreading area. The cell polarity is characterized by first fitting the ellipse on the cell boundary. Then we extract the aspect ratio of the fitted ellipse, which is the ratio of major axis length over minor axis length. Higher cell polarity is reflected by higher cell aspect ratio.

2.4.2 Immunofluorescence

Cells apply force to the underlying environment through the intracellular interaction between myosin motors and actin filaments in the cytoskeleton network [34, 133, 134]. Thus, visualizing the cytoskeleton structure provides the key to understanding the difference or similarity in the mechanical force response of the cell to ECM changes. In this project, we use immunofluorescence to image actin cytoskeletons at high magnification to fully understand the result of traction force measurement.

Cells were first seeded on glass for approximately 16 hours then washed with 37 °C PBS supplemented with 1 mM Ca^{2+} and 0.5 mM Mg^{2+} . Afterwards, the cells were fixed with 3.7%

paraformaldehyde in PBS for 10 min, then permeabilized in 0.1% Triton-X PBS (Alfa Aesar, Haverhill, MA, USA) for 15 min. Cells were then stained for actin cytoskeleton with Alexa Fluor488 Phalloidin (Molecular Probes, Eugene, OR, USA) at 4 units per 1 mL PBS for 30 min, followed by nucleus staining with 1 µg/mL DAPI (Biotium, Fremont, CA, USA) for 10 min. Fluorescent images were captured using a QIClick Camera (QImaging, BC, Canada) mounted on an Olympus IX83 microscope with 60x objective (Olympus America Inc., Center Valley, PA, USA).

2.4.3 Migration characterization

The process of cell migration involves contractile forces that pull the cell body forward and promote retraction at the back of the cell. Hence, impaired force transmission mechanism will lead to changes in cell migration patterns [134, 135]. These changes could be observed through measuring migration speed or characterizing the directionality of the migration pattern. In this project, due to low time resolution of the time-lapse experiment, we characterize the directional cell migration over a long period of time through various means such as final displacement (how far does the cell move away from its initial position), total distance traveled and directional persistence.

Cell centroids were extracted from MATLAB cell boundary tracing over the time course of the experiment. All centroids are then normalized against a cell centroid at t_0 and then plotted as trajectories. From centroid positions, we can calculate final displacement: $D =$

$$\sqrt{(x_f - x_0)^2 + (y_f - y_0)^2}, \text{ total distance traveled: } d = \sum_{i=1}^f \sqrt{(x_i - x_{i-1})^2 + (y_{i-1} - y_i)^2},$$

where f is the final time point and x, y indicates centroid position in Cartesian coordinates.

Migration speed can be calculated by dividing the total distance traveled by the time course of

the experiment. To characterize the directionality of cell migration trajectories, we utilized directional autocorrelation [136]. Directional autocorrelation (DA) represents the angle of migration that displacement vectors form, measured over different timescales (Figure 9).

Directional autocorrelation is calculated using:

$$DA(n) = \frac{1}{N - n + 1} \sum_{i=0}^{N-n} (\vec{v}_{(i+n)\Delta t} \cdot \vec{v}_{i\Delta t}) = \frac{1}{N - n + 1} \sum_{i=0}^{N-n} \cos(\alpha_{(i+n)\Delta t} - \alpha_{i\Delta t})$$

Here, $DA(n)$ is the directional autocorrelation of a given cell at step size n , given the total number of displacement N . It is calculated using the dot product of two normalized velocity vectors $\vec{v}_{(i+n)\Delta t} \cdot \vec{v}_{i\Delta t}$. For the population of C cells, the average directional autocorrelation for a given time interval is calculated using the formula below: $\langle DA \rangle_C = \sum_{j=1}^{j=C} (DA)_j \cdot N_j / \sum_{k=1}^{k=C} N_k$

A plot of DA against the time interval represents the correlation in the angle of migration over time. A cell with a low persistency in migration path (more randomized migration pattern) will have a faster decay in directional autocorrelation curve.

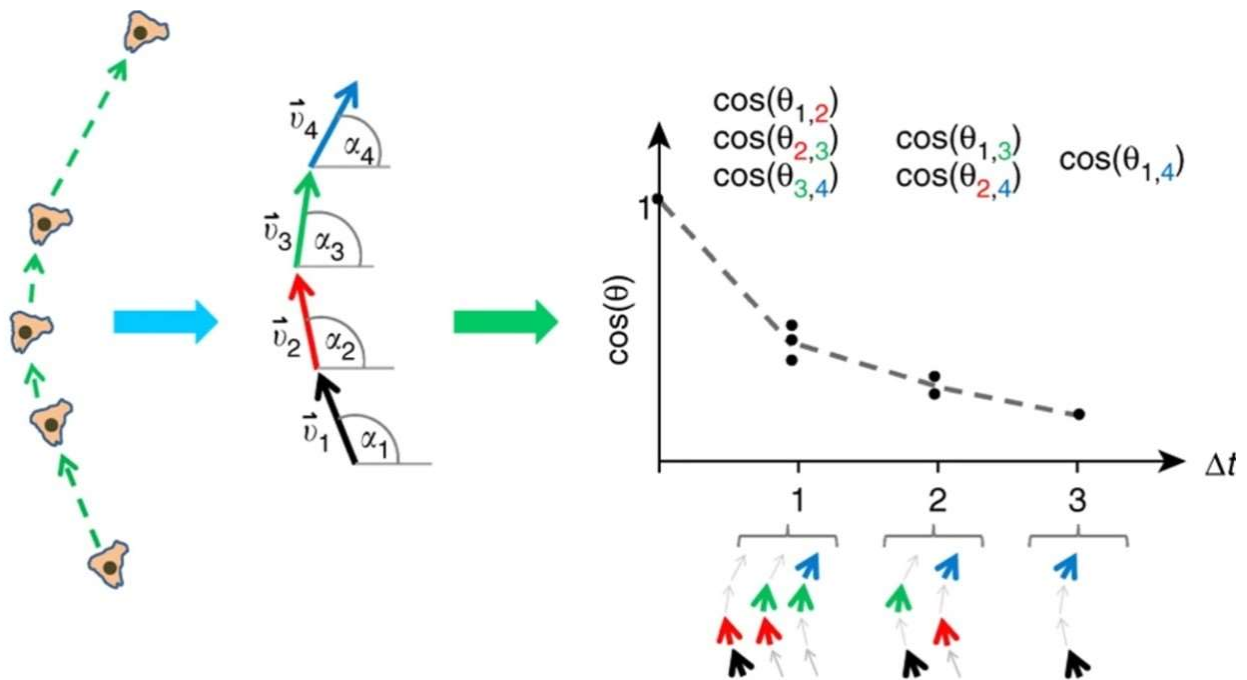


Figure 9. Demonstration of directional autocorrelation (DA). Adapted from [136]. DA is calculated using the dot product of two normalized velocity vectors $\vec{v}_{(i+n)\Delta t} \cdot \vec{v}_{i\Delta t} = \cos(\alpha_{(i+n)\Delta t} - \alpha_{i\Delta t})$ over different time scale Δt . A cell with low persistence in its directional migration path will have a much faster decay in directional autocorrelation plot.

Chapter 3: Effects of vimentin knockdown on fibroblasts'

mechanosensing

3.1 Background

Vimentin is a type of intermediate filament (IF) protein expressed in cells of mesenchymal origin, e.g. fibroblasts, neuronal cells and endothelial cells. While it is critical for normal cell function, vimentin has also been implicated in many aspects of cancer initiation and progression, including tumorigenesis, epithelial-to-mesenchymal transition (EMT) and the metastatic spread of cancer [81, 137]. Vimentin expression in epithelial cells, which normally do not express vimentin, is a marker for prostate cancer, gastrointestinal tumors and many other types of cancer [80, 138-141]. Knocking out vimentin in mice led to impaired wound healing in both embryonic and adult stages and fibroblasts derived from these knockout mice are mechanically weak and have severely reduced capacity to migrate [142]. However, it remains unclear how vimentin regulates normal cell function and cancer progression.

A growing body of evidence indicates that, in addition to helping maintain the mechanical integrity of cells [22-24], vimentin may regulate cell behavior by playing a role in mechanosensing and mechanotransduction. Since cells sense mechanical cues by actively exerting force on the extracellular matrix, mechanosensing and mechanotransduction rely on intricate force transmission between the extracellular matrix, the cytoskeleton and the interior of the nucleus [6]. Knocking out vimentin in mouse embryonic fibroblasts (mEFs) reduces their contractile forces on collagen gels [143]. Whereas, in osteosarcoma cells and dermal

fibroblasts, silencing the vimentin expression leads to increased contractile strength [144].

These studies demonstrated that vimentin expression influences the ability of cells to generate force. However, there is no direct study on how vimentin regulates cellular sensitivity to extracellular matrix's rigidity. Additionally, knocking out vimentin completely could potentially lead to gene compensation [145], causing discrepancies between knockout mutant and knockdown phenotypes. Hence, in this work, we study the effects of vimentin knockdown on cells' rigidity sensing ability. We demonstrate that reducing the level of vimentin in 3T3 fibroblasts impairs force transmission in cells and results in a reduction in traction force. However, the reduced traction force does not impair the 3T3 fibroblasts' ability to sense substrate rigidity.

3.2 Materials and Methods

3.2.1 Cell Lines

NIH-3T3 fibroblasts were cultured in DMEM (BioWhittaker, Walkersville, MD) supplemented with 10% bovine calf serum (Gibco, Waltham, MA), 2mM L-Glutamine (Gibco), 100 µg/ml streptomycin and 100 units/ml penicillin (Gibco). Vimentin knockdown (shVim) 3T3 line was obtained by transfecting the NIH-3T3 fibroblasts using a lentiviral vector containing short hairpin RNA (shRNA) against mouse vimentin. Western blot analysis and Quantitative Polymerase Chain Reaction (qPCR) was used to determine the relative levels of vimentin mRNA in clonally selected cell lines where vimentin RNA has been knocked down (see Figure 10). The vimentin knockdown (shVim) cells were cultured in the same medium as the control cell line with the addition of 2 µl/ml of puromycin dihydrochloride (Gold Biotechnology, Olivette, MO) to remove

non-transfected/non-infected cells. For inhibition studies, control and vimentin knockdown fibroblasts were inhibited by adding 10 mM Y27632 (Cell Signaling Technology, Danvers, MA, USA) in a 1:1000 volume ratio to cell culture dishes for 12-16 hours before imaging.

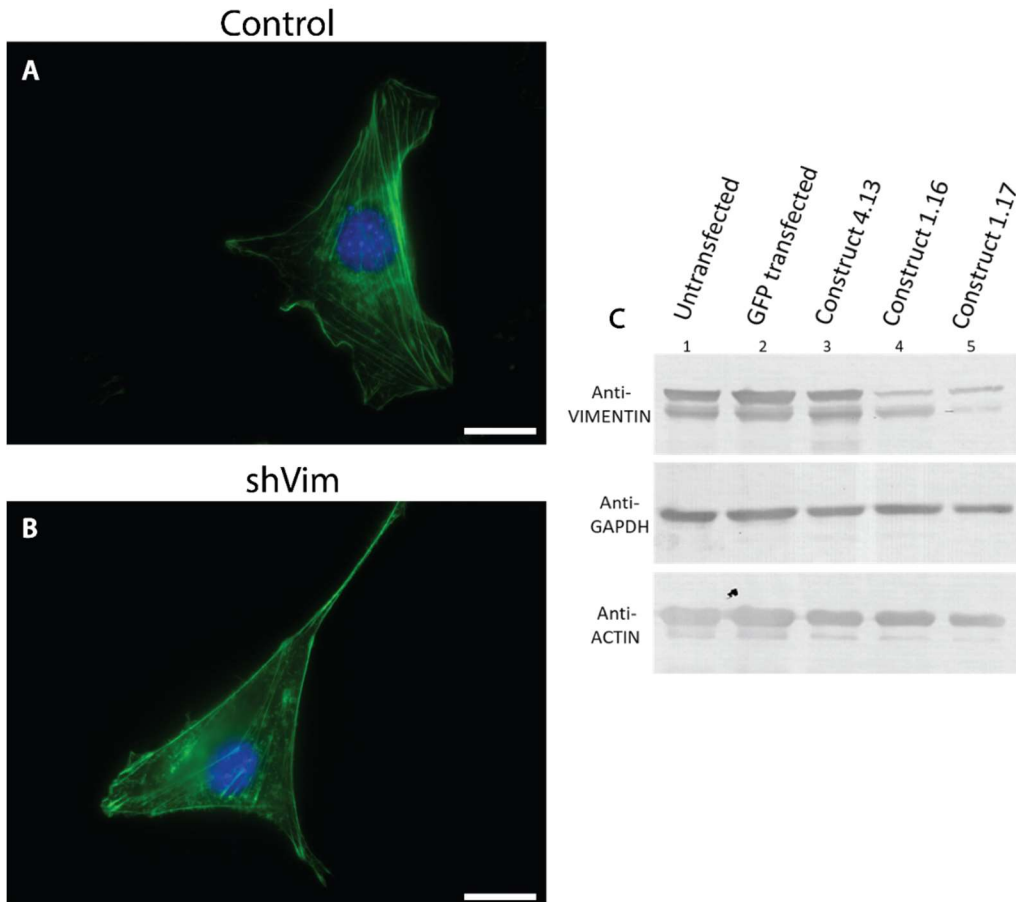


Figure 10.(A and B) Phalloidin staining for actin filament of control and vimentin knockdown 3T3. Control cells have more elongated actin stress fiber across the nucleus region compared to knockdown cells. Scale bar: 20 μ m C. Vimentin knockdown 3T3 western plot analysis. Vimentin RNA levels are knocked down using a lentiviral vector containing short hairpin RNA (shRNA) against mouse vimentin in constructs 4.13, 1.16 and 1.17. Clone 1.17 was chosen as the vimentin knockdown 3T3 fibroblast for all experiments performed in this paper. Subsequent

qPCR analysis of clone 1.17 results in of 5.4-fold decrease in vimentin expression compared to normal 3T3.

3.2.2 Substrate preparation

Polyacrylamide gels were prepared as described in **Chapter 2.2 Substrate Preparation**. For both cell area/aspect ratio and traction force experiments, we used 5 different rigidity: 2000, 7500, 13000, 20000 and 40000 Pa. The gel stiffness values were chosen to cover the typical tissue stiffness, ranging from human lung tissue stiffness to bone tissue stiffness. Force correlation length calculation and migration analysis were done on fibroblasts cultured on 7500 Pa gels.

3.2.3 Cell viscoelasticity measurements

Atomic Force Microscopy was applied to measure the viscoelasticity property of cells following the procedure described in Gawain Thomas et. al [146, 147]. All measurements were performed utilizing an MFP-3D-BIO atomic force microscope (Asylum Research, Santa Barbara, CA, USA) and DNP cantilevers (Bruker, Camarillo, CA, USA) with nominal spring constant 0.06 N/m.

Before being subjected to AFM measurements, cells were seeded for 12 hours on the collagen-coated polyacrylamide gels. Cell rigidity values were extracted from the recorded AFM force-distance curves using a custom MATLAB routine. To measure the cell viscoelastic property, we impose the AFM cantilever to a small amplitude sinusoidal oscillatory motion, 25 nm in amplitude and 10 Hz in frequency, when it reaches the deepest point of indentation. The phase lag between cell deformation and force is determined and the tangent function of phase

lag, i.e., loss tangent, is reported to represent the ratio of elastic storage modulus over elastic loss modulus (E''/E').

3.2.4 Migration Studies

Centrifuged cells are seeded on a petri dish containing polyacrylamide gel and were transferred directly to the environment chamber mounted on the microscope system described above. For every 10 minutes over 4.5 hours, phase contrast images of the cells are taken. Trajectories of both control and shVim cells over a 4.5 hours period are plotted base on the centroid position. From centroid trajectories, we can find average initial-final displacement, total distance traveled, as well as directional auto correlation curves for both control and vimentin knockdown cell lines.

3.2.5 Statistics

All results presented were tested for significant difference using unpaired Student t-tests with equal/unequal variance using Microsoft Excel Data Analysis Tool and Prism. Linear regressions are also compared using Prism's ANCOVA. Differences with P-value less than 0.05 were all considered significant. All errors listed are standard error of the results. In all figures, *, ** and *** represent p-value less than 0.05, 0.01 and 0.001 respectively. Error bars represent standard deviation unless indicated. Error bars on XY graphs represent standard error of the mean (SEM) to demonstrate the difference between populations.

3.3 Results

3.3.1 Vimentin knockdown does not affect the ability of cells to sense substrate rigidity

To study the effect of knocking down vimentin on the ability of 3T3 fibroblasts to sense changes in substrate rigidity, we measured the cell shape of both control and shVim fibroblasts as functions of substrate rigidity (Figure 11). Both cell lines were able to respond to substrate rigidity changes by adjusting their shape. On the softest gel (2 kPa), cells assume the smallest spreading area and have the least polarized shape. As gel rigidity increases, both cell lines increase their spreading area and develop a more polarized shape. Notably, the shVim cell line appears to have a slightly smaller spreading area (Figure 12A) and a smaller polarization factor (Figure 12B) than the control fibroblasts. However, these parameters tested between the two cell lines are only statistically different for cells cultured on the softest gel (2 kPa).

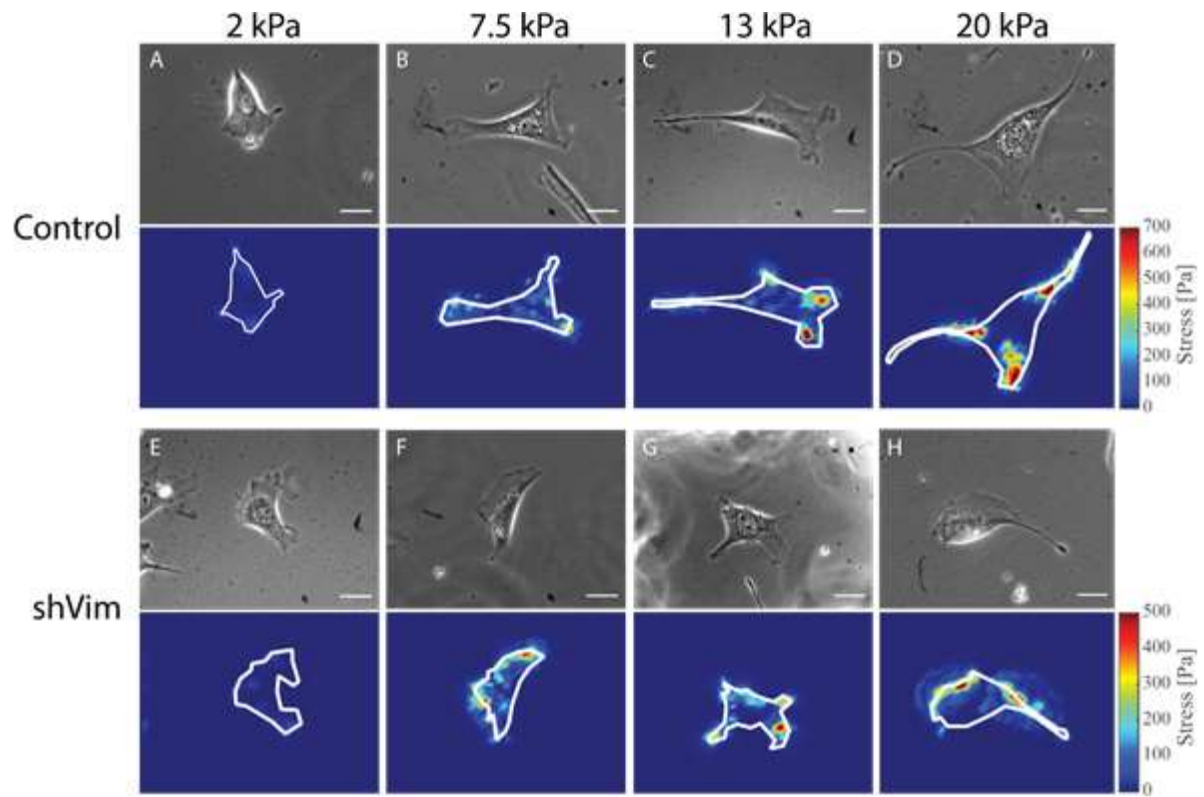


Figure 11. Phase contrast images and stress heat maps of control and vimentin knockdown fibroblasts on different substrate rigidity. Cell edges are drawn in white on heat maps. Scale bar = 10 μm .

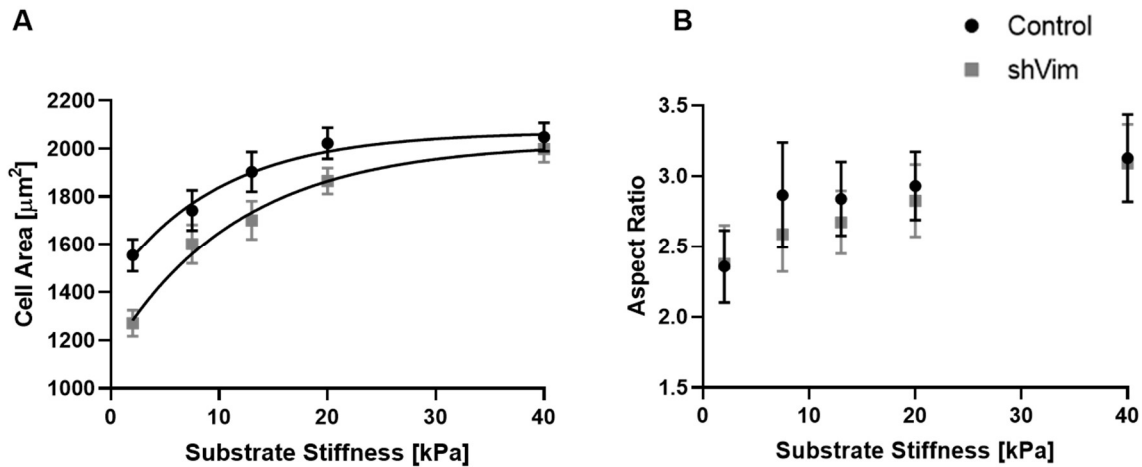


Figure 12. Cell Area (A) and Aspect Ratio (B) comparison between control (Round) and vimentin knockdown (Square) 3T3 fibroblasts. Cell spreading area and aspect ratio of both control and shVim fibroblasts respond to changes in ECM rigidity. Error bars represent standard error of the mean (SEM) to demonstrate the difference between two population. (N ≥ 120 cells)

3.3.2 Vimentin knockdown leads to a reduction in total cell traction force

The total traction force output by vimentin knockdown cells overall is lower than the output by the control group across all rigidity values (Figure 13A). As the rigidity increases from 2 kPa to 40 kPa, the total traction force of the control fibroblasts group increases non-linearly from 170 nN to approximately 400 nN. For the shVim fibroblasts group, the total traction force increases non-linearly from 130 nN to around 320 nN over the same rigidity range. Hence, both control and vimentin knockdown 3T3 cells have the ability to change their mechanical output in response to ECM rigidity changes. Because total traction force scales with cell area, we also plot total traction force against cell area for both populations (Figure 14). Linear regression reveals that the control fibroblasts total traction force exerted by control fibroblasts is higher than

shVim with the same area for all rigidity conditions. Likewise, average traction stress, defined as total traction force divided by cell area, is significantly higher for control fibroblasts compared to their vimentin knockdown phenotype ($p = 0.0005$) (Figure 14)

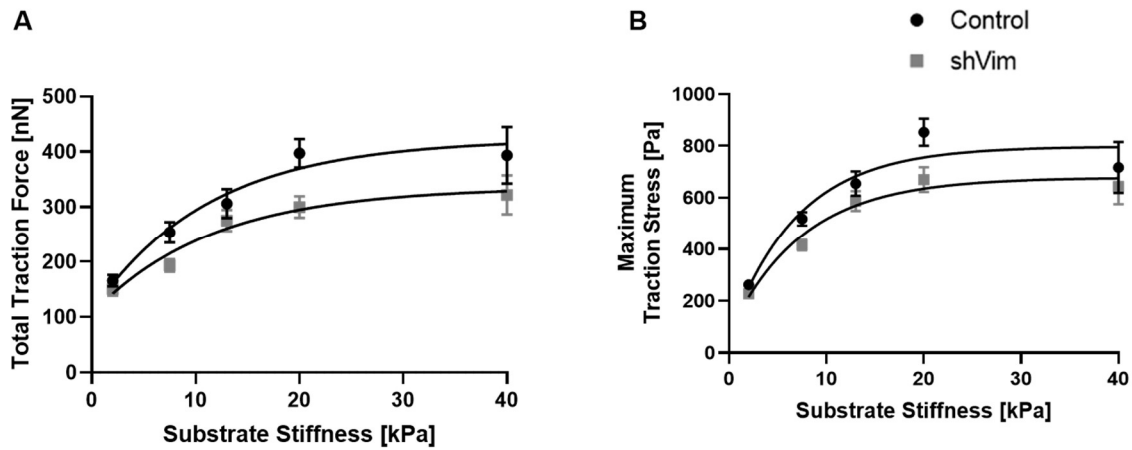


Figure 13. Total Traction Force (A) and Maximum Stress (B) comparison between Control (Round) and shVim (Square) 3T3 fibroblasts. Both cell lines' mechanical output changes in response to different substrate rigidity. However, shVim cells apply lower total traction force on all substrate rigidity compared to control cells. Error bars represent standard error of the mean (SEM) to demonstrate the difference between two population. ($N \geq 23$ cells)

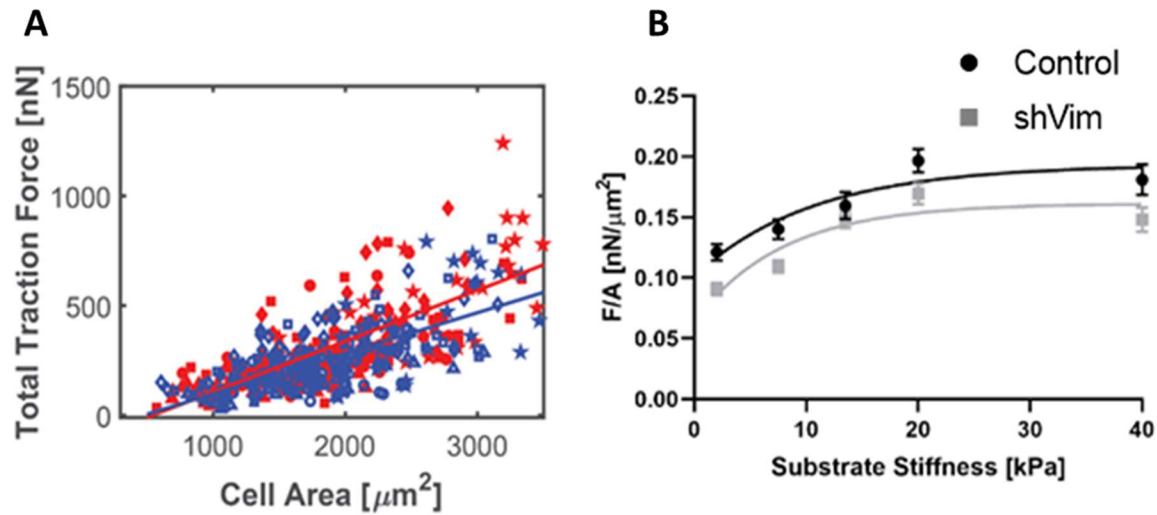


Figure 14. Total traction force plotted against cell area for all substrate rigidity comparison between Control (Red) and shVim (Blue) 3T3 fibroblasts. Triangle: 2kPa; Round: 7.5kPa; Square: 13kPa; Diamond: 20kPa; Polygon: 40kPa. Linear Regression reveals that vimentin knockdown population tends to produce lower traction force compare to control fibroblasts of the same cell area. Slope: Control: 0.232 ± 0.015 nN/ μm^2 ; shVim: 0.185 ± 0.005 nN/ μm^2 . B. Plot of total force over Cell Area for cells in all condition. Control 3T3 cells have higher average stress than vimentin knockdown phenotype. $p = 0.0005$. Error bars represent standard error of the mean (SEM) to demonstrate the difference between two population.

3.3.3 Vimentin knockdown reduces maximum traction stress of fibroblasts

Like the total force, the maximum stress in vimentin knockdown cells is lower than the control group across all rigidity values (Figure 13B). For both cell lines, the maximum stress increases linearly as the rigidity goes from soft to intermediate range then plateaus as the rigidity increase further. The maximum stress exerted by the control 3T3 fibroblasts increases linearly from 260 Pa to around 750 Pa as the substrate rigidity increases from 2 kPa to 20 kPa

then reaches a plateau at roughly 800 Pa. On the other hand, the maximum stress by shVim group exhibits linear growth from 230 Pa to 600 Pa as substrate rigidity increases only from 2 kPa to 13 kPa substrate. As substrate rigidity increases further to 40 kPa, the maximum stress of the vimentin knockdown group reaches a plateau at 650 Pa. The total traction force and stress results demonstrate that while knocking down vimentin expression decreases the mechanical output; it does not affect 3T3 cells' ability to adjust their mechanical output in response to changes in the substrate rigidity. However, there is a significant decrease in the maximum amount of stress that the cells can apply to the substrate when vimentin is knocked down.

3.3.4 Reducing traction force by ROCK inhibition suppresses cellular response to substrate rigidity

While vimentin deficient fibroblasts retain the ability to sense the rigidity of the surrounding environment, we observed that they produce lower traction force and stress on substrate when compared to control fibroblasts. To test whether the mechanosensing ability is still conserved with low level of traction force, we treated 3T3 fibroblasts with ROCK inhibitor - Y27632, which has been shown previously to be one of the traction force regulators [148]. Our result (Figure 15 A) shows that after 30 minutes of Y27632 treatment, the average total traction force of control and shVim fibroblasts decreases to 40 nN and 50 nN, respectively. We measured the cell area of both control and shVim fibroblasts treated with Y27632 on soft (2.5 kPa) and stiff (20 kPa) polyacrylamide gels, as well as glass. Comparing with the non-inhibited population, both control and shVim fibroblasts treated with Y27632 no longer react to changes in substrate rigidity (Figure 15B). Cells grown on soft PAA gels were as large as cells grown on either stiff gels or glasses.

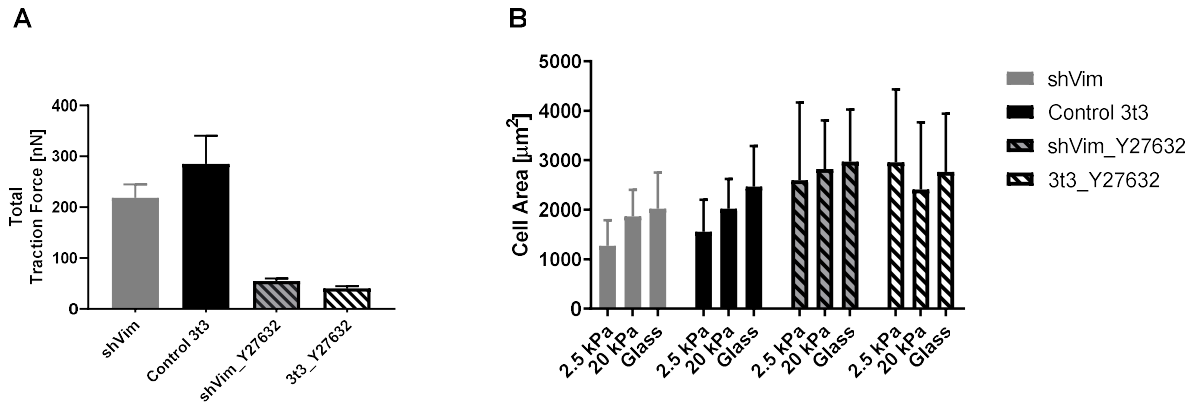


Figure 15.(A) Y27632 (ROCK inhibitors) treatment reduces traction force applied by control 3T3 fibroblasts by approximately 8 times from the average of 300 nN to 40 nN. (B) Control and vimentin knockdown 3T3 fibroblasts' cell spreading area on 2.5kPa, 20 kPa polyacrylamide gels and glass with or without Y27632 - ROCK inhibitors. Inhibition of ROCK pathway renders both control 3T3 and vimentin knockdown fibroblasts insensitive to rigidity change. Error bars indicate SD. (N = 11)

3.3.5 Vimentin knockdown leads to a reduction in force correlation length

We also studied the details of force transmission inside cells by measuring the correlation length (L_p) of traction stress vectors. Figure 16B demonstrates that the directional correlation of stress vectors of shVim cells decays faster as a function of distance. In Figure 16C, the average correlation length of control cells is 10 μm , which is roughly more than 20% of the cells' major axis length, indicating the long-distance force transmission in these cells. In vimentin knockdown cells, the average correlation length is only 5 μm , suggesting that the distance of transmission in shVim cells is much shorter than that in control cells.

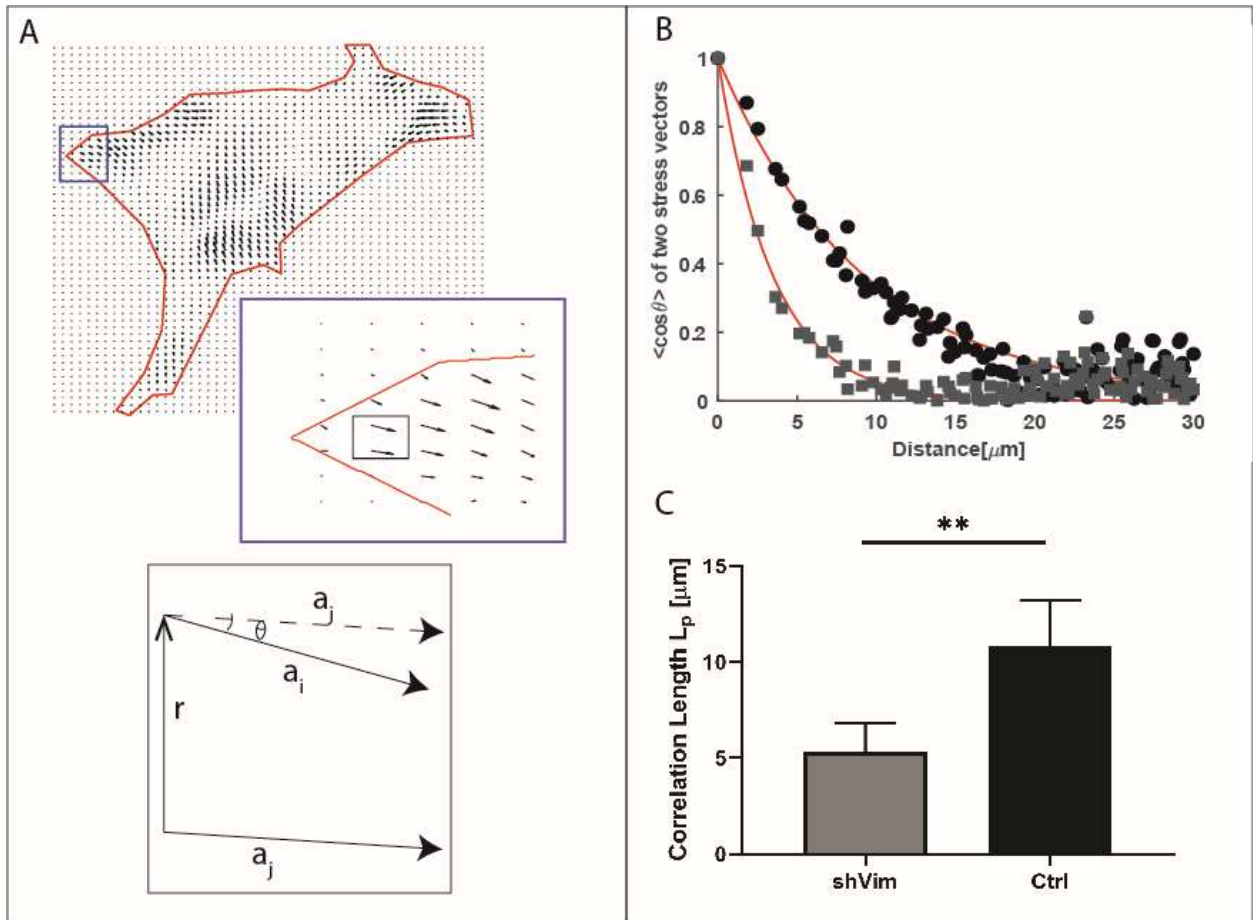


Figure 16. (A) Demonstration of calculation of correlation length: for any pair of two vectors a_i and a_j in the stress map that are separated by distance r , we first normalized a_i and a_j , then calculated the average dot product between them and subsequently fit the result to the persistence equation: $\langle \vec{a}_i \cdot \vec{a}_j \rangle = \langle \cos \theta_{ij}(r) \rangle = C e^{-\frac{r}{L_p}}$, where L_p is the correlation length. (B) Average normalized dot product $\langle \cos(\theta) \rangle$ vs distance of a control and vimentin 3T3. (C) Average correlation length L_p of control and vimentin knockdown fibroblasts. Error bars indicate SD. (N = 9)

3.3.6 Knocking down vimentin reduces directional cell migration

Finally, we quantified the effect of knocking down vimentin on cell migration. Centroid trajectories are plotted for control and vimentin knockdown population in Figure 17 A,B. Afterward, cell migration is characterized by obtaining the average displacement and the average total distance traveled of each population. From Figure 17 C,D, we can see that while the total distance traveled is the same for both control cells and vimentin knockdown cells, control cells on average move further away from their initial position compared to vimentin knockdown cells. To understand this result, we quantified the directional persistence in cell migration by calculating the directional autocorrelation (DA) and plot the result as a function of the time interval (figure 18) [149]. Vimentin knockdown fibroblasts directional autocorrelation curve decays faster than control fibroblasts, indicating a weak correlation in the angle of normalized velocity vectors over time. This result implies that vimentin knockdown cells lack directional persistence compared to control fibroblasts, i.e. they frequently change the direction of migration.

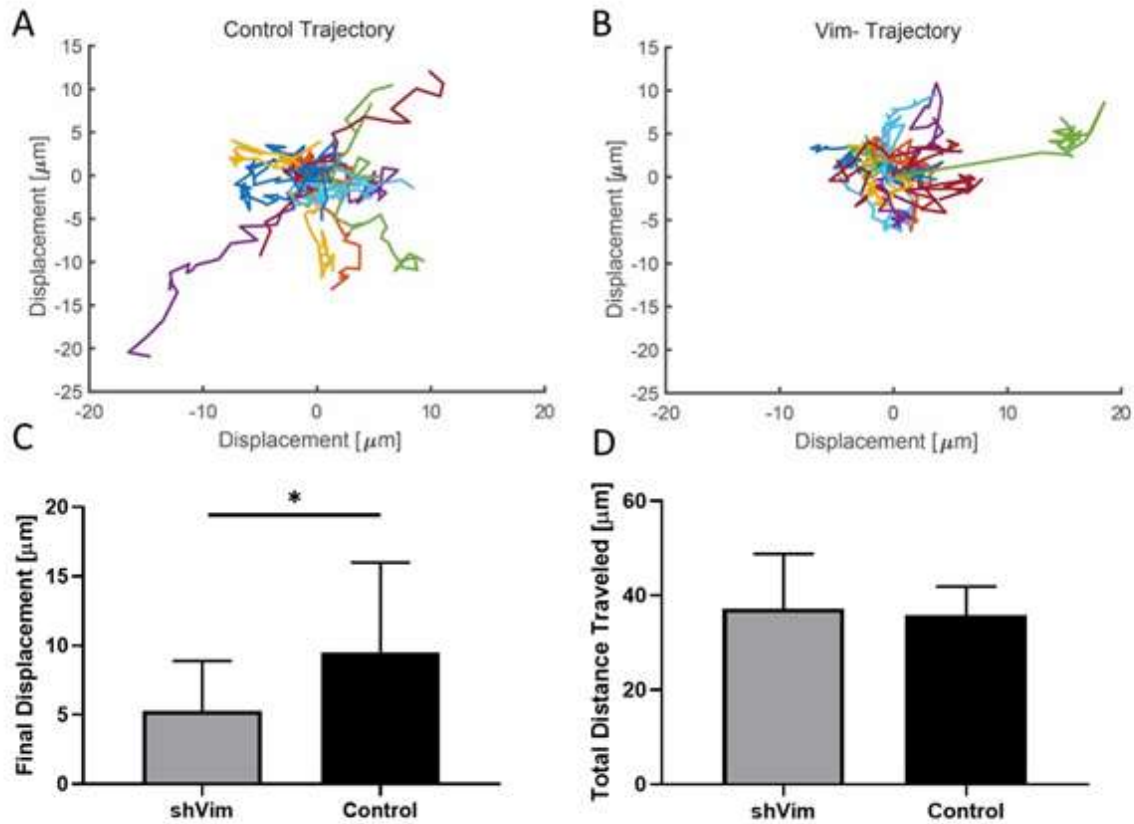


Figure 17.(A and B) Trajectories of centroids of each control and shVim cell over 4.5 hours. (C) Total displacement between $t = 0$ and $t = 4.5$ hours and (D) Total distance traveled between $t=0$ to $t = 4.5$ hours for both control and shVim cells. Similar distance covered but different displacement suggests a difference in directional migration between control and shVim cells.

Error bars indicate SD (N = 14).

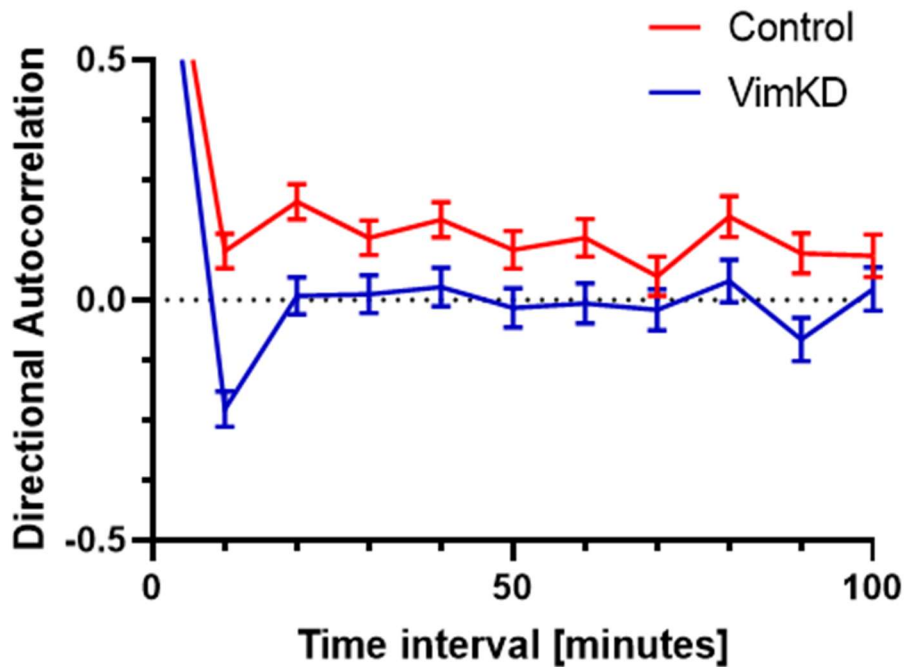


Figure 18. Directional Autocorrelation analysis of control and shVim fibroblasts. Directional autocorrelation curve of vimentin knockdown cells decays faster than that of control cells, indicating a lower persistency in cell migration pattern in shVim. Error bars indicate SD.

(N=14)

3.4 Discussion

In order to identify how knocking down vimentin in fibroblasts results in a lower force, we need to establish how the cell applies force to the surrounding environment. The cell first generates intracellular force by the cross-bridging interactions of actin and myosin II cytoskeleton [150]. This force is then transmitted through the cytoskeleton network and applied to the extracellular matrix through cell-ECM adhesions [135, 151, 152]. These focal adhesions are the sites where integrins bridge the extracellular matrix with the cellular

cytoskeleton and recruit a complex network of signaling and scaffolding proteins [153]. The exerted force also triggers cellular signaling by inducing conformational or organizational changes to protein receptors, complexes and ion channels [15, 154, 155]. This process, called mechanotransduction, effectively transduces the physical signals into biochemical responses [133]. Hence, reduction of traction force may be caused by either a reduction in force generation or the impaired force transmission through cytoskeleton network and force transmission through focal adhesion complexes to substrate.

If we visualize the force transmission pathway (Figure 19A) as a network of cytoskeletal structures including microtubules, actin microfilaments and vimentin intermediate filaments connected by mechanical cross-linker plectin [156, 157], then the intracellular force is presumably affected when components of this network are altered. Evidently, knocking out cross-linker (plectin) between vimentin intermediate filaments (VIF) and F-actin experiment leads to softer cells [158]. Traction force measured on plectin knockout mouse embryonic fibroblasts is also lower compared to wild type. Similarly, in our experiment, we have shown that shVim cells are less stiff while also exerting lower total traction force compared to control fibroblasts (Figure 14A,20A).

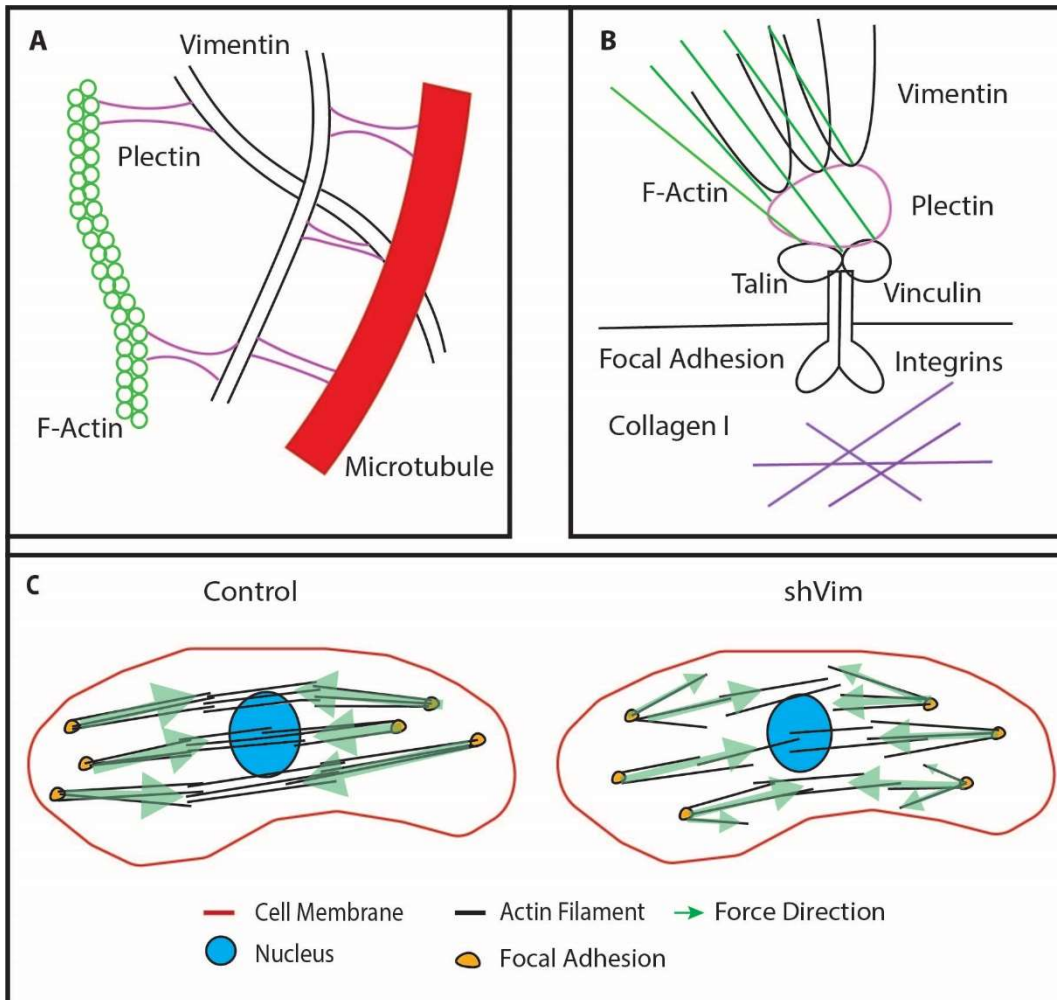


Figure 19. Interaction of vimentin intermediate filaments, F-actin with focal adhesion proteins.

A: Vimentin IFs are bind to various cytoskeleton structure in cells via plectin mechanical linkers;

B: Vimentin IF network is connected to integrins in focal adhesion through plectin. When vimentin expression is knocked down, this connection is severed and thus leads to weak force

transmission. C: Presence of vimentin network increases the alignment of actin. Insufficient

vimentin leads to appearance of shorter actin filaments/bundles (Figure 10) and more

randomized traction stress orientation (Figure 16).

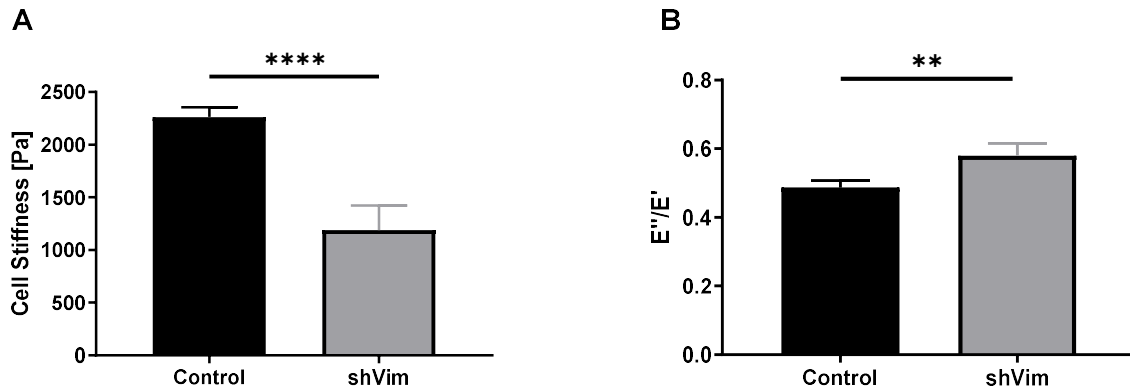


Figure 20. (A) Cell elastic rigidity and (B) Ratio of elastic storage modulus over elastic loss modulus E''/E' , of control (black) and vimentin knockdown (gray) 3T3 fibroblast. Vimentin knockdown cells are softer than control fibroblasts but have a higher E''/E' ratio, implying that intracellular force are much more susceptible to damping effect in vimentin knockdown population. Error bars indicate SD. (N=9).

There are strong pieces of evidence showing that vimentin deficiency affects the mechanics of the cytoskeleton network. Vimentin deficient fibroblasts have been shown to be softer than wild-type cells via magnetic twisting cytometry, displaying compromised mechanical stability [143]. Moreover, active micro-rheology measurement has shown that the cytoplasmic shear modulus G' of vimentin knockout cell is 80% lower than that of wild type, while loss moduli G'' of both are similar [159]. Hence, the ratio of G''/G' , defined as $\tan \delta$, of vimentin knockout cells is much larger than their wild type counterpart. Using atomic force microscopy, we measured elastic storage modulus E' , elastic loss modulus E'' and their ratio $\tan \delta$ of control and shVim cells. Our results (Figure 20B) are consistent with the shear moduli result established above. Since the ratio of loss modulus over storage modulus $\tan \delta$ represents the ratio of

energy dissipated over stored energy, higher $\tan \delta$ measured on vimentin knockdown/knockout cell line means energy dissipation is dominated in these cells' cytoplasm. This result implies that intracellular force is much more susceptible to damping effects in vimentin knockdown cells. These pieces of evidence combined indicate that reducing/silencing vimentin changes the rigidity, viscoelastic properties of the cytoplasm and implicates the mechanics of cytoskeleton network. Consequently, actomyosin force was not transmitted efficiently in the shVim cells.

The corollary of this damping effect is that we could observe the dissipation of force transfer inside the cytoplasm of vimentin knockdown cells. Indeed, disruption of force transfer between integrins and the nucleus in endothelial cells by disrupting the vimentin system with acrylamide has been observed by Maniotis et al., 1997. Micropipette pulling on capillary endothelial cells with a disorganized vimentin network resulted in lower nuclear elongation in the direction of the pull compared to wild type [160]. Traction force distributions also appeared to be more homogeneous with control cells than with vimentin knockdown cells in Y. Liu et al [161]. In our experiment, we try to quantify this effect using correlation length, estimating the distance over which the stress vectors alignment is lost. The result (Figure 16C) reveals that while 3T3 fibroblasts' traction stresses are still strongly aligned over distances as large as 10 μm , vimentin knockdown cells' traction stresses quickly disorient after the first 5 μm . This result directly supports previous observation showing vimentin knockdown can also alter the cytoskeleton network such that it might affect the long-range force propagation (\sim tens of μms) [162]. Likewise, it has been predicted that the long-range force propagation also becomes short-ranged (a few μms) when either the pre-stress in the actin stress fibers are inhibited or disrupted [8, 163]. Altogether, these cross-linked components (VIF, plectin and F-Actin) of the

cytoskeleton are crucial for robust force transmission. Knocking down vimentin thus leads to inefficient force transmission to the underlying substrate.

During cell migration, forces generated by the actin cytoskeleton are transmitted through adhesion complexes to the substrate to drive cellular motion [134, 135, 143]. Hence, an indirect significance of the lower directional force correlation in vimentin knockdown is that we can observe a reduction in cell migration persistence of vimentin knockdown compared to control fibroblast (Figures 17,18). Directed collective cell migration has been shown to be influenced by long-range intercellular force transmission in both 2D and 3D ECM [164, 165]. In our experiment, we have also shown that long-range intracellular force transmission would lead to higher directional migration at a single-cell level. In addition, this result furthers our understanding of how vimentin promotes the migration of cells. Vimentin fibers restrict the formation of lamellipodia and actin flow while facilitating the alignment of traction forces, resulting in higher force transmission persistence which promotes single-cell migration in collaboration with microtubules [161, 166].

On the other hand, force transmission through adhesion/integrin could also be compromised. This transmission, called the adhesion clutch model, is mediated by leading-edge actin retrograde flow with FA molecules and ECM-bound integrin (ligand-integrin-actin linkage) [14, 167, 168]. A well-studied example of this clutch model is the linkage of actin filament to β_1 integrin tail (collagen-ligand) via FA molecules talin and vinculin [41]. Vimentin intermediate filaments have also been shown to physically link to focal contacts in the filopodium of motile cells [169], suggesting that VIF might play a key role in regulating cell-substrate adhesion [170]. For instance, in vimentin associated matrix adhesion (VMA), the adhesion clutch involves a

connection between vimentin IF and actin filaments with β_1 integrins via actin crosslinking protein filamin A [88, 171, 172] or with $\alpha_v\beta_3$ integrins via FA protein plectin [173]. Maximum traction stress (Figure 13B) result, which has been used to predict the maximum focal adhesion strength [174-176], can give more insight into how shVim can influence the adhesion clutch. We observed that shVim fibroblasts reach a lower maximum stress plateau compared to control fibroblasts. This result suggests that vimentin knockdown affects the maximum force that focal adhesions can withstand, which causes the low binding state of integrins [177], leading to integrin slippage (clutch disengagement) rather than stable linkage to ECM [178]. Subsequently, such slippage between actin and ECM results in lower traction force propagated to ECM [167, 179, 180].

Cells rely on traction force to sense substrate rigidity. Yet lowering traction force does not affect mechanosensing ability in shVim, indicating that vimentin plays a role in force transmission but is not involved in transduction of force signal. Many proteins in the focal adhesion are able to transduce force signals through its force-induced conformational changes. As discussed in **Section 1.1.3**, force-induced conformation changes in talin to expose its hidden vinculin-binding sites [48]. Integrins such as $\alpha_{IIb}\beta_3$, $\alpha_v\beta_3$, etc. undergo conformational changes from low affinity to an open, high affinity state under applied force [50, 51]. Another example of such change is the force-activating open and close states of mechanosensitive ion channels [9, 10, 181]. Therefore, mechanotransduction remains intact, as long as the traction force magnitude is high enough to induce conformational changes of mechanosensors. This is similar to the working principle of a rheometer [182], whereby the mechanical properties of the

sample can be acquired as long as shear stress applied is enough to cause measurable deformation in the sample.

3.5 Summary

Knocking down vimentin resulted in fibroblasts applying lower total traction force and maximum traction stress to the substrate. However, shVim cells can react to changes in physical properties in the environment: cell area, shape and traction force adapt to rigidity changes. Since mechanosensing describes the ability of a cell to sense and respond to the surrounding mechanical cues and adapt to the changing environment [5], these pieces of evidence support that vimentin knockdown does not abolish the aforementioned mechanosensing mechanism of cells. Unimpaired mechanosensing might explain why cell biological functions are not largely compromised in several in vitro experiments involve vimentin-lacking organisms [183-186].

Chapter 4: Effects of PTEN loss and activated KRAS overexpression on breast epithelial cells' mechanosensing

4.1 Background

Tumor initiation and progression is typically associated with malfunctioning cell signaling pathways resulting in abnormal cell proliferation, differentiation, apoptosis resistance [54]. Common alterations to major signaling pathways in human breast cancer involve the phosphatidylinositol 3-kinase (PI3K) pathway and the mitogen-activated protein kinases (MAPK) pathway [187]. Overactivation of the PI3K pathway has been observed in 70% of tumors from patients with invasive breast cancer. Upregulation of ERK1/2, a major effector of the Ras/MAPK pathway, has been observed in 50% of primary breast tumors as compared to adjacent healthy tissue [188]. In addition, phosphorylation of ERK has been implicated in breast tumor cells capable of metastasis [189]. Dual activation of the PI3K and Ras/MAPK pathways in healthy MCF-10A breast cells via PTEN loss and KRAS activation (Figure 21) promotes tumorigenic behavior in vivo. However, PTEN loss and KRAS activation individually was not sufficient to promote tumorigenesis but instead generated a dormancy phenotype [190] (Figure 22). These dormant cancer cells are present in early tumor progression or are residuals left behind after the treatment of the primary tumor [191].

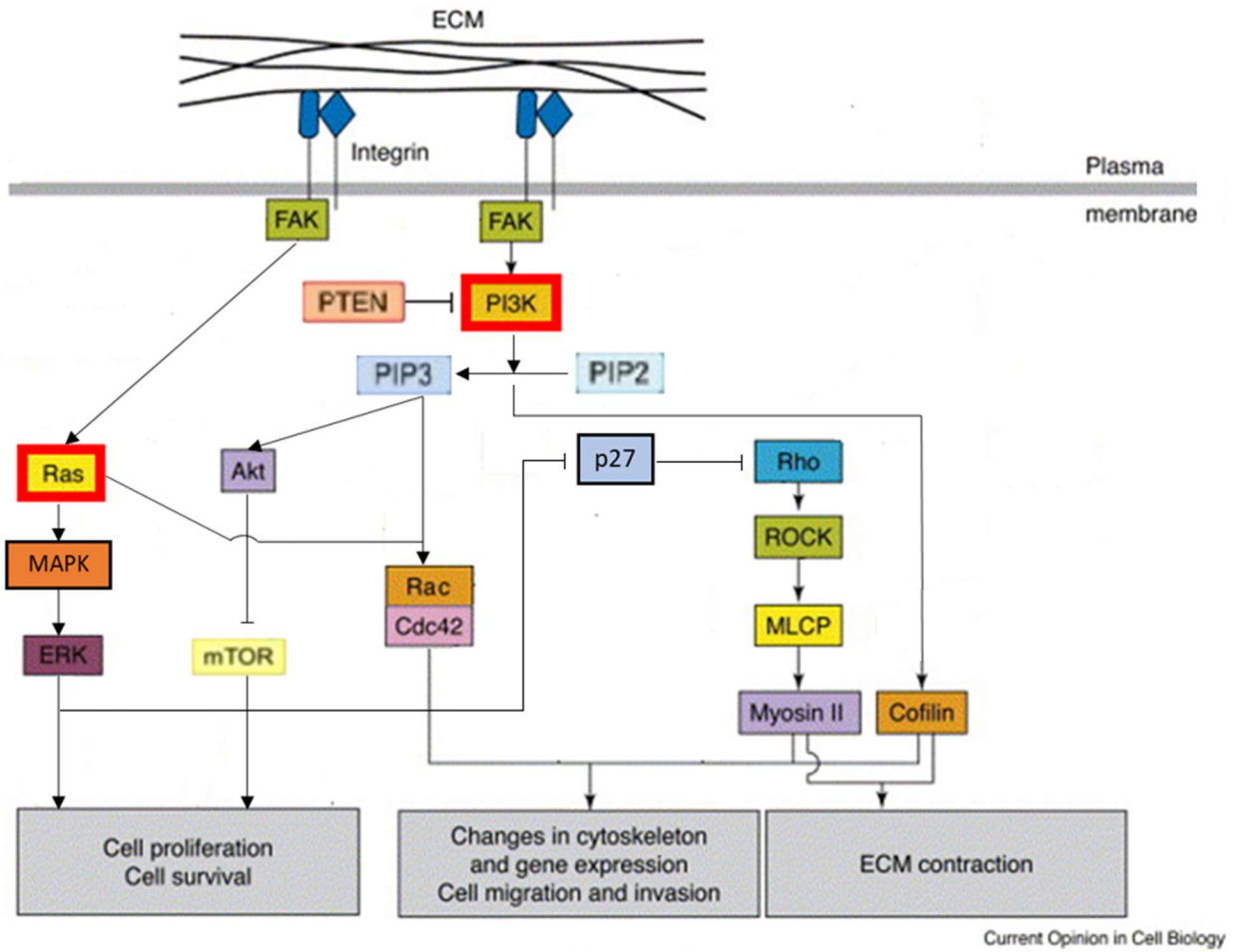


Figure 21. Depiction of several signaling pathways regulating major cellular behavior properties. Adapted from [192]. Our pathways of interest, involving PI3K and Ras, are highlighted by bold, red boxes.

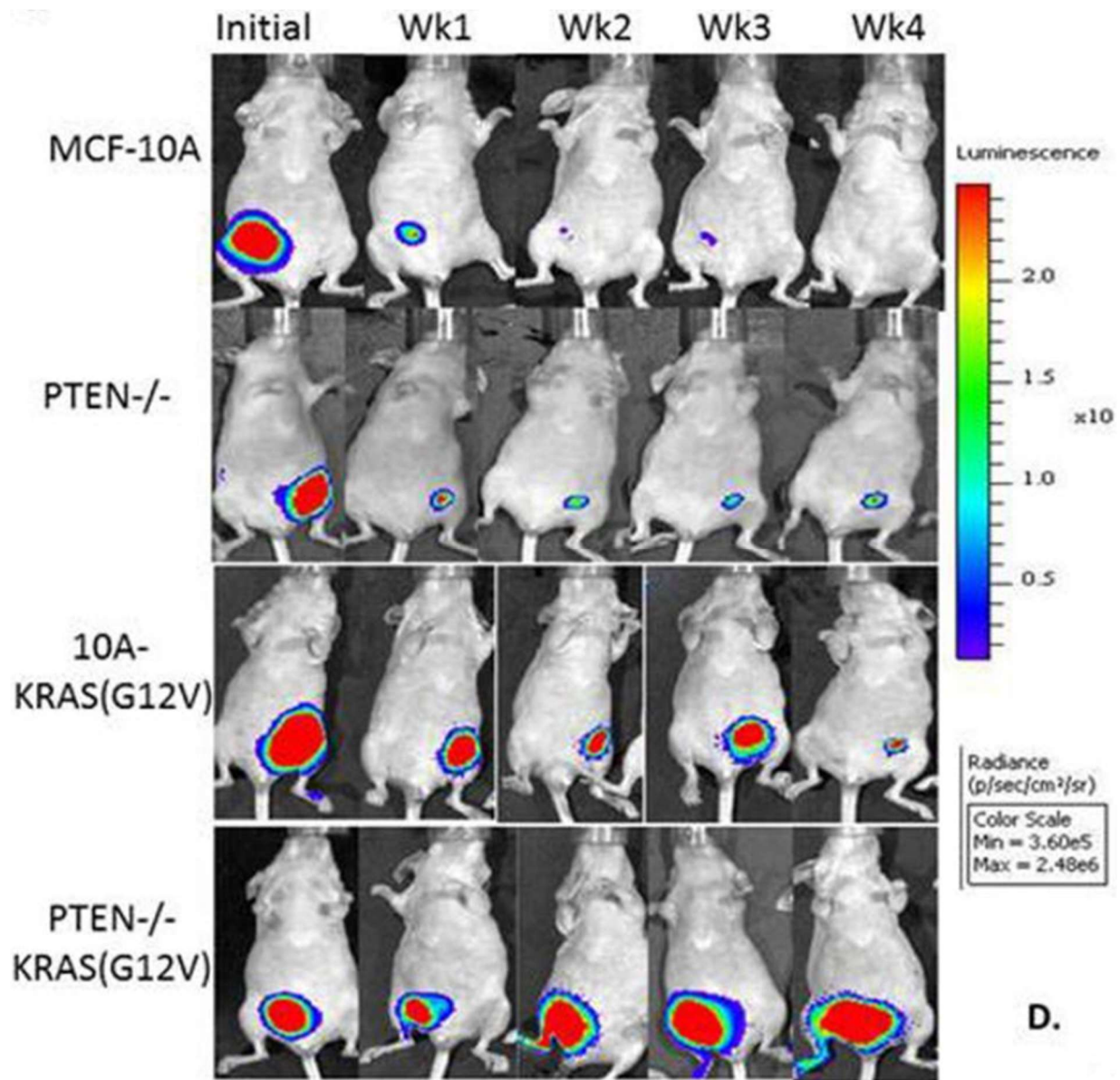


Figure 22.(A and B) Bioluminescence imaging of female athymic nude-Foxn1nu mice over four weeks with injected MCF-10A cells with varied PI3K and Ras/MAPK pathway expression, modulated through PTEN knockout and KRAS(G12V) overexpression respectively. Adapted from

[193].

Aberrant mechanical response of cells has been implicated in many aspects of cancer initiation and progression, including tumorigenesis, epithelial-to-mesenchymal transition (EMT), and the metastatic spread of cancer [194]. A number of cancer cell types and Ras-transformed cells (including pancreatic, breast and kidney) exhibit rigidity insensitivity [195, 196]. On the other hand, PTEN regulates the activity of Phosphatidylinositol 4,5-bisphosphate (PIP2) [197, 198], which is involved in the organization of actin dynamics in the cell membrane [199] as well as the activation focal adhesion kinase [200] – two essential components of the mechanosensing process. Hence, PTEN and KRAS may play roles in regulating cell mechanosensing ability and mechanotransduction. Yet, no study has been conducted to explore how PTEN and KRAS influence the mechanosensing pathway and its implication.

We present the first set of studies on the effects of PTEN loss and activated KRAS overexpression on the mechanosensing of human breast epithelial cells, MCF-10A. Cell shape and traction force as functions of substrate rigidity were compared between a healthy MCF-10A cell line with a cell line with PTEN deletion (PTEN^{-/-}), a cell line with overexpression of activated KRAS (10A-KRAS(G12V)), and a cell line with both PTEN deletion and activated KRAS overexpression (PTEN^{-/-}-KRAS(G12V)).

4.2 Materials and Methods

4.2.1 Cell Lines

MCF-10A cells were bought from ATCC (Manassas, VA, USA). PTEN^{-/-}, 10A-KRAS(G12V) and PTEN^{-/-}-KRAS(G12V) cell lines were created from the MCF-10A cell line by our collaborator Dr. Vitolo from University of Maryland. Briefly, the PTEN^{-/-} cells were created by deleting exon

2 of PTEN and 10A-KRAS through retroviral infection of the KRAS(G12V) gene [190, 193]. Cells were cultured in an incubation chamber at 37 °C and 5% CO₂ in high humidity. DMEM/F-12 media (Invitrogen, Grand Island, NY) supplemented with 5% Horse serum (Gibco, New Zealand), 1% Penicillin-Streptomycin (Gemini Bio-Products, West Sacramento, CA), 0.2 µg/mL recombinant human EGF (Invitrogen), 0.2 µg/mL Cholera Toxin (Sigma), 10 µg/mL Insulin (Sigma) and 0.5 µg/mL hydrocortisone (Sigma, St. Louis, MO) was used to promote cell proliferation and growth.

MDA-MB-231 cells were bought from ATCC (Manassas, VA, USA) . MDA-MB-231 cells are cultured in DMEM culture media (BioWhittaker, Walkersville, MD) supplemented with 10% fetal calf serum (Gibco, Waltham, MA), 2mM L-Glutamine (Gibco), 100 µg/ml streptomycin and 100 units/ml penicillin (Gibco) at 37 °C and 5% CO₂ in high humidity to promote healthy growth and proliferation.

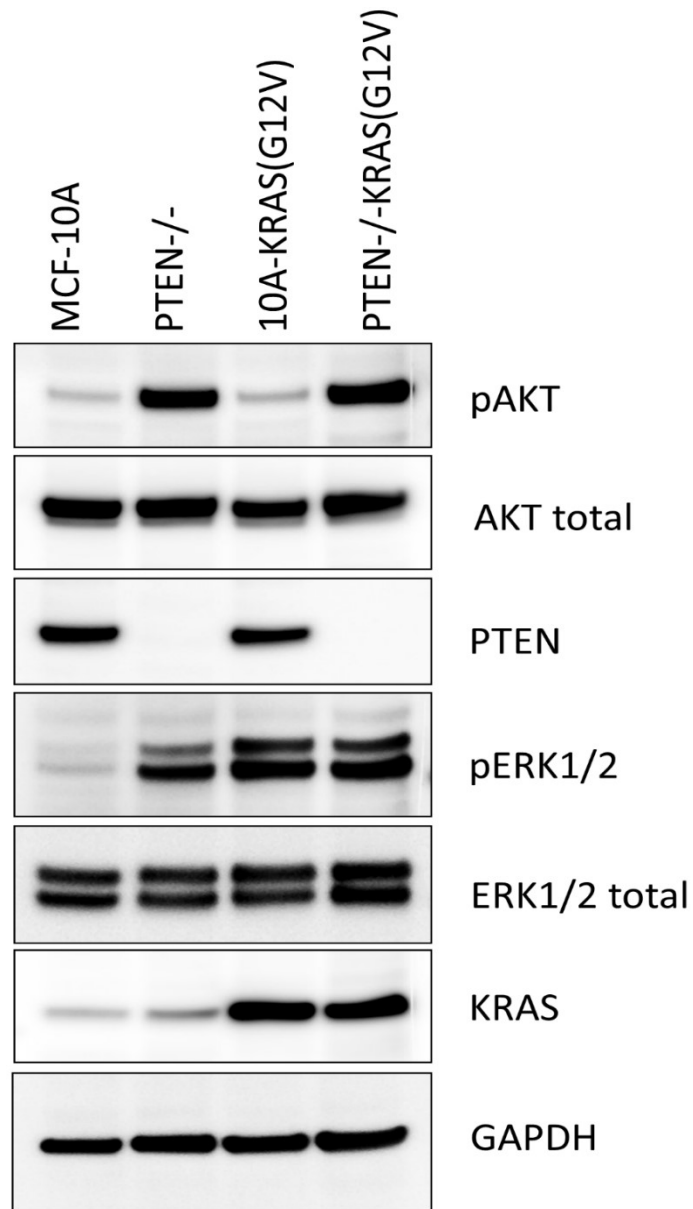


Figure 23. Western blots of MCF-10A, PTEN^{-/-}, 10A-KRAS(G12V) and PTEN^{-/-}-KRAS(G12V) cells highlighting proteins critical to the expression of the PTEN/PI3K/AKT (pAKT level) and KRAS/MAPK/ERK pathway (pERK1/2 level). Adapted from [146].

4.2.2 Substrates

Since native breast tissues are soft (≈ 1000 Pa) [201, 202], we used a very soft polyacrylamide gel with a rigidity of 800 Pa (measured by AFM). For such soft gels, gel-making protocols mentioned in **Chapter 2.2** usually resulted in tears, wrinkles on the gel surface, which are due to the 18mm round coverslip used for gel-forming is hydrophilic (oxygen plasma cleaned). As a result, it is tough to peel off the coverslip and leave the soft gel intact. Even without plasma cleaning, half of the time, we would not get a wrinkle-free gel after peeling off the coverslip. Instead, we submerged the coverslip in Rain-X (RAIN-X, Houston, TX, USA) to make the surface hydrophobic. Then we wiped the Rain-X solution off with a 70% ethanol tissue. Polyacrylamide solution (3% acrylamide, 0.12% bis-acrylamide) can be deposited on the Rain-x coated coverslip. After the gel is polymerized, the coverslip can now be peeled off safely. Since the coverslip is now hydrophobic, beads solution cannot be deposited on the surface very well. Thus, the beads coating on Rain-X coverslip needs to be applied several times to achieve the same density as coating on non-Rain-X coverslips.

For both cell area/aspect studies, we used four different rigidities: 800, 2000, 7500 and 13000 Pa. For traction force experiment, since there are problems reconstructing force on 800 Pa gels (refer to **Chapter 6.3 Future directions**), we used 2000, 3500, 7500 and 13000 Pa gels. Correlation length calculation and migration were done on cells cultured on 7500 Pa gels.

4.2.3 Migration Studies

Centrifuged cells are seeded on a petri dish containing polyacrylamide gel and were transferred directly to the environment chamber mounted on the microscope system described

above. For every 15 minutes over 7.5 hours, phase contrast images of the cells are taken.

Trajectories of MCF-10A, PTEN^{-/-}, KRAS(G12V) and PTEN^{-/-}-KRAS(G12V) cells over 7.5 hours are plotted based on the centroid position. From centroid trajectories, we can find the average initial-final displacement, the total distance traveled, and the directional auto correlation curve for both healthy MCF-10A and mutated cell lines.

4.2.4 Statistics

All results presented were tested for significant difference using unpaired Student t-tests with equal/unequal variance using Microsoft Excel Data Analysis Tool and Prism. Linear regressions are also compared using Prism's ANCOVA. Differences with P-values less than 0.05 were all considered significant. All errors listed are standard errors of the results. In all figures, *, ** and *** represent p-value less than 0.05, 0.01 and 0.001 respectively. Error bars represent standard deviation unless indicated. Error bars on XY graphs represent standard error of the mean (SEM) to demonstrate the difference between populations.

4.3 Results

4.3.1 PTEN knockout and KRAS overexpression have opposite effects on cell morphology response to substrate rigidity

We measured the cell spreading area and cell aspect ratio of MCF-10A, PTEN^{-/-}, 10A-KRAS(G12V), PTEN^{-/-}-KRAS(G12V) and MDA-MB-231 as functions of substrate rigidity (Figures 25AB, 26AB, 27AB). All cell lines except PTEN^{-/-} were able to respond to substrate rigidity changes by adjusting their shape (Figure 24). Both cell area and cell aspect ratio of PTEN^{-/-} group are invariant with substrate stiffness. KRAS(G12V) and PTEN^{-/-}-KRAS(G12V) conditions

alter cell shape significantly. KRAS overexpressed cells assume a large cell spreading area compare to other cell lines. Their average cell area is around $1500 \mu\text{m}^2$ compared to around $1000 \mu\text{m}^2$ for the other three cell lines on the highest substrate rigidity. This characteristic holds even in lower substrate rigidity, reflected by higher average cell area on 800 Pa compared to MCF-10A, PTEN^{-/-} and MDA-MB-231 cells (approximately $500 \mu\text{m}^2$ larger). KRAS(G12V) and PTEN^{-/-}KRAS(G12V) significantly increase MCF-10A cells' polarity, reflected by a higher aspect ratio. MDA-MB-231 cancer cells show extremely high aspect ratio on high substrate rigidity.

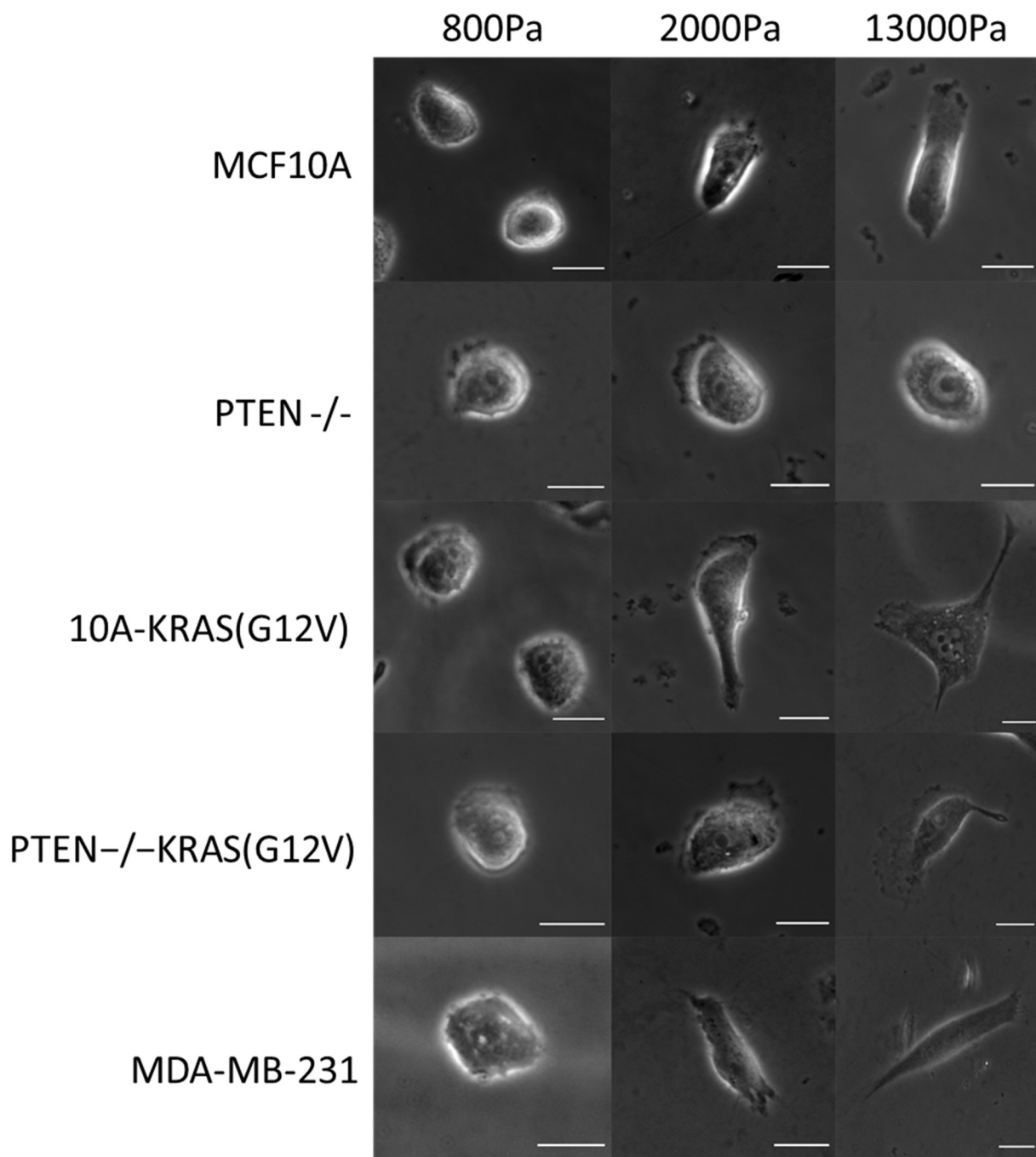


Figure 24. Typical morphology of MCF-10A, PTEN^{-/-}, 10A-KRAS(G12V), PTEN^{-/-}-KRAS(G12V) and MDA-MB-231 on soft (800 Pa), intermediate (2000 Pa) and stiff (13000 Pa) gels. KRAS mutated groups and MDA-MB-231 have very distinct cell morphology on very stiff substrate.

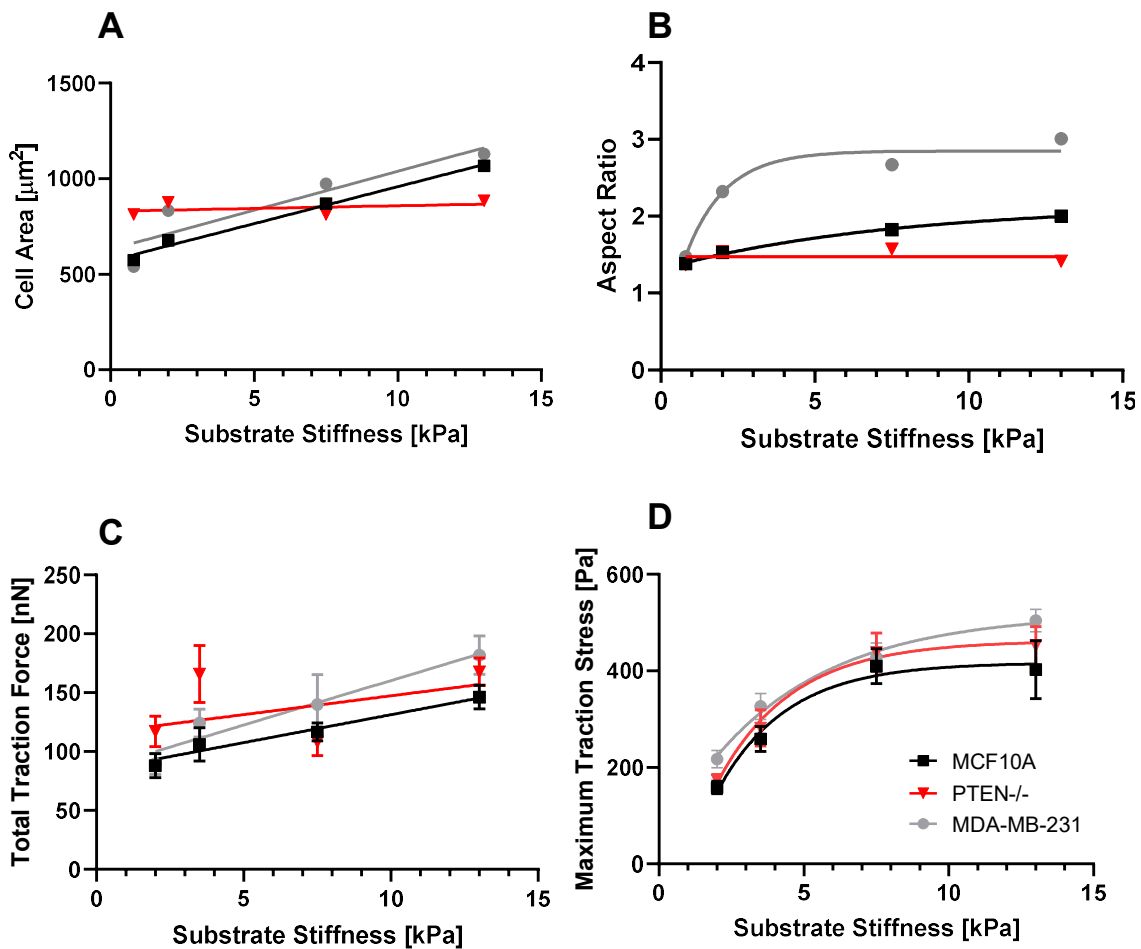


Figure 25. Comparison of cell area, aspect ratio, total traction force and maximum stress of MCF-10A, PTEN^{-/-} and MDA-MB-231 on 4 different substrate rigidities: 800, 2000, 7500 and 13000 Pa. Linear fit was performed on cell area and total traction force to test whether the slope is significantly non-zero. Exponential plateau fit is performed on aspect ratio and maximum stress. Error bars represent SD. PTEN^{-/-} slopes are not significantly different from 0, demonstrating insensitivity to substrate rigidity. (N ≥ 18, n ≥ 3)

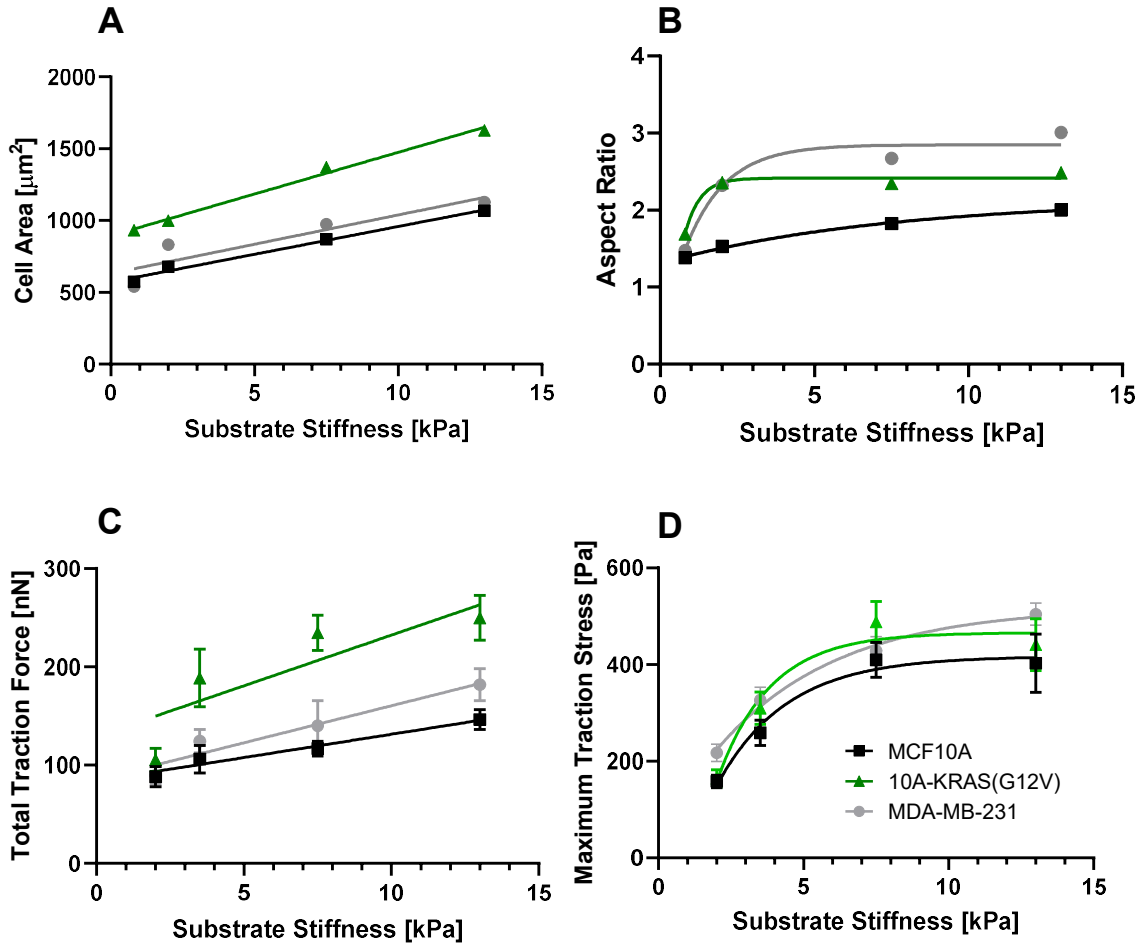


Figure 26. Comparison of cell area, aspect ratio, total traction force and maximum stress of MCF-10A, 10A-KRAS(G12V) and MDA-MB-231 on 4 different substrate rigidity: 800, 2000, 7500 and 13000 Pa. Linear fit was performed on cell area and total traction force to test whether the slope is significantly non-zero. Exponential plateau fit is performed on aspect ratio and maximum stress. Error bars represent standard error of the mean (SEM) to demonstrate the difference between two population. ($N \geq 18$)

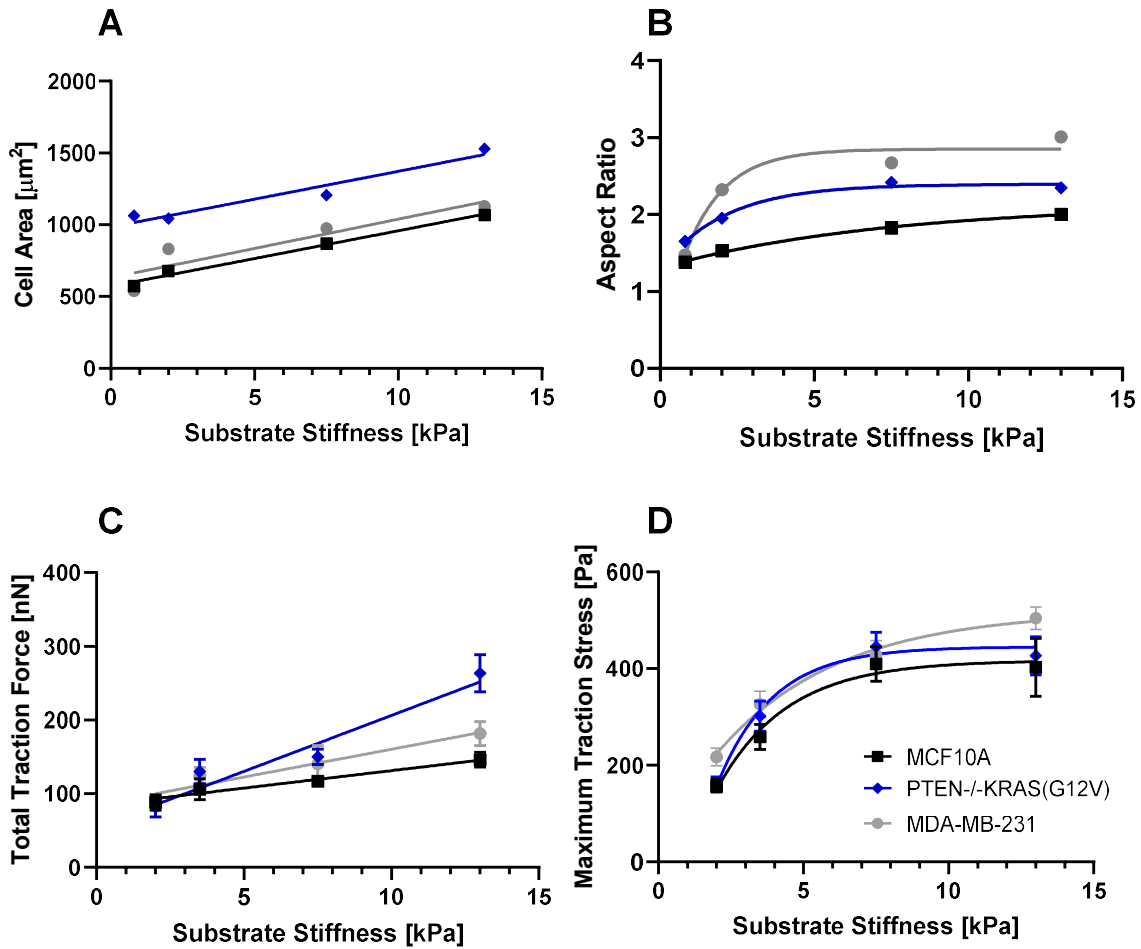


Figure 27. Comparison of cell area, aspect ratio, total traction force and maximum stress of MCF-10A, PTEN-/-KRAS(G12V) and MDA-MB-231 on 4 different substrate rigidities: 800, 2000, 7500 and 13000 Pa. Linear fit was performed on cell area and total traction force to test whether the slope is significantly non-zero. Exponential plateau fit is performed on aspect ratio and maximum stress. Error bars represent standard error of the mean (SEM) to demonstrate the difference between two populations. ($N \geq 18$)

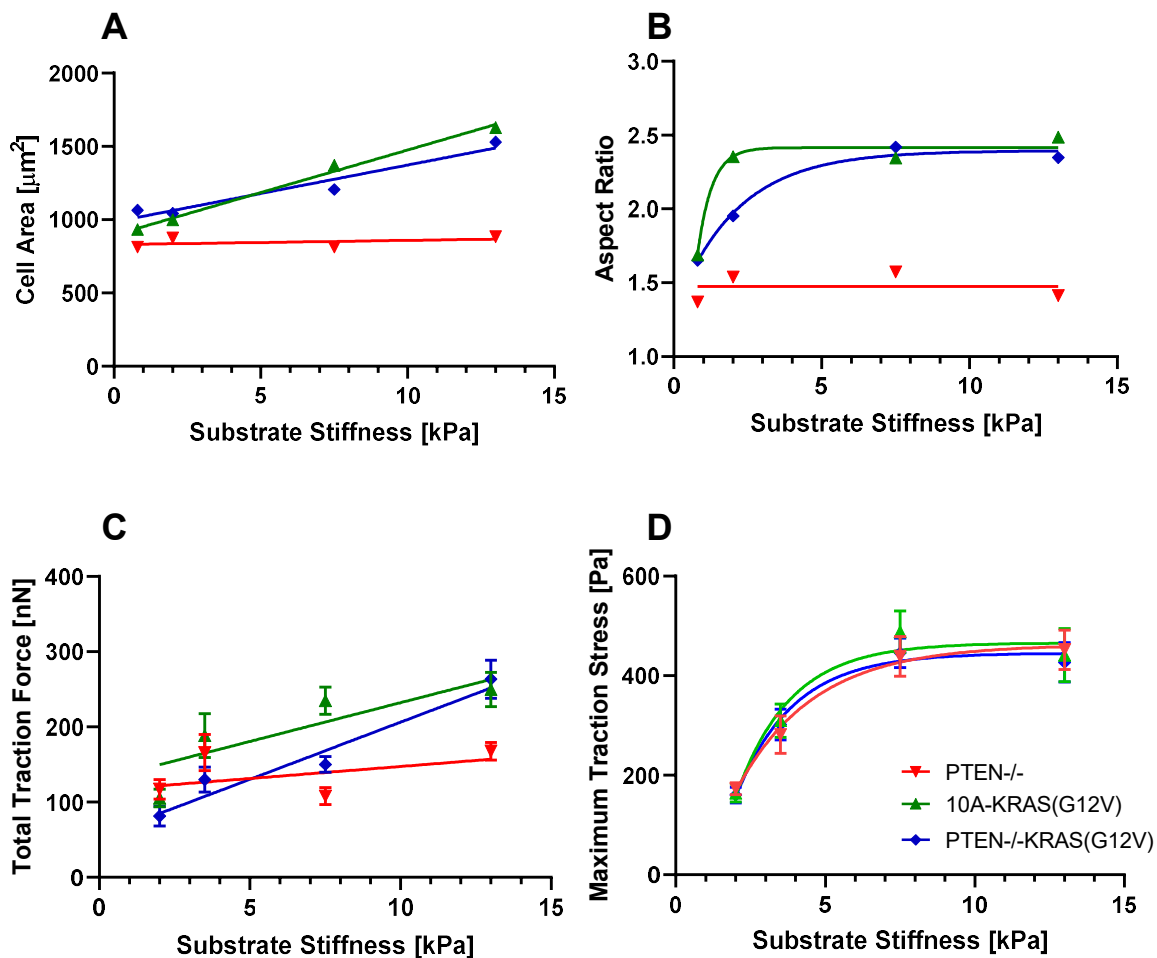


Figure 28. Comparison of cell area, aspect ratio, total traction force and maximum stress of PTEN^{-/-}, KRAS(G12V) and PTEN^{-/-}-KRAS(G12V) on 4 different substrate rigidity: 800, 2000, 7500 and 13000 Pa. Linear fit was performed on cell area and total traction force to test whether the slope is significantly non-zero. Exponential plateau fit is performed on aspect ratio and maximum stress. Overexpressing KRAS overturns the characteristics of PTEN^{-/-} on MCF-10A. PTEN^{-/-}-KRAS(G12V) cells can respond to changes in rigidity. Error bars represent standard error of the mean (SEM) to demonstrate the difference between two population. (N \geq 18)

4.3.2 PTEN knockout and KRAS overexpression have opposite effects on cell traction response to substrate rigidity

Total traction force response of MCF-10A, PTEN^{-/-}, 10A-KRAS(G12V), PTEN^{-/-}-KRAS(G12V) and MDA-MB-231 to different substrate rigidity is very similar to their shape response (Figures 25C, 26C, 27C). All conditions, except PTEN^{-/-}, demonstrate the ability to adjust total traction force with different rigidity. Furthermore, 10A-KRAS(G12V) and PTEN^{-/-}-KRAS(G12V) cells generate significantly higher traction force than the control MCF-10A, PTEN^{-/-} and even MDA-MB-231 cells.

4.3.3 Maximum traction stress scales with substrate rigidity in all conditions.

Unlike the previous two parameters (shape and total traction), maximum traction stress of PTEN^{-/-} group scales with increasing substrate rigidity (Figures 25D, 26D, 27D). PTEN^{-/-}, 10A-KRAS(G12V), PTEN^{-/-}-KRAS(G12V) and MDA-MB-231 expressed higher maximum stress than control MCF-10A on all rigidity conditions. In addition, while PTEN^{-/-}, 10A-KRAS(G12V) and PTEN^{-/-}-KRAS(G12V) cell lines reach their plateau maximum stress in the chosen rigidity range (2-13 kPa), MDA-MB-231 cells do not. MDA-MB-231 cancer cells continue the trend of increasing maximum stress as rigidity increases from 7.5 to 13 kPa.

4.3.4 PTEN knockout and KRAS overexpression modifies actin cytoskeleton structure and force correlation length

Next, we quantified the force transmission in cells by calculating the force correlation length (L_p). The result is plotted in Figure 30. All the four cell lines have L_p values smaller than 10 μm , significantly smaller than the L_p value of fibroblasts measured in Chapter 3. Compared

to the MCF-10A cell line, the PTEN^{-/-} cells have smaller L_p value, whereas the KRAS(G12V) cells have significantly greater L_p value. With KRAS overexpression, the PTEN^{-/-}-KRAS(G12V) cells have significantly greater L_p value than the PTEN^{-/-} cells.

Quantitative analysis of actin cytoskeleton structure is also done using immunofluorescence (Figure 29). The percentage of cells exhibiting stress fibers is shown in Figure 29F. Control MCF-10A population exhibits stress fibers in nearly all cells. PTEN^{-/-} results in a decrease in the percentage of cells that express stress fibers. Both KRAS(G12V) and PTEN^{-/-}-KRAS(G12V) have a high probability of exhibiting stress fibers.

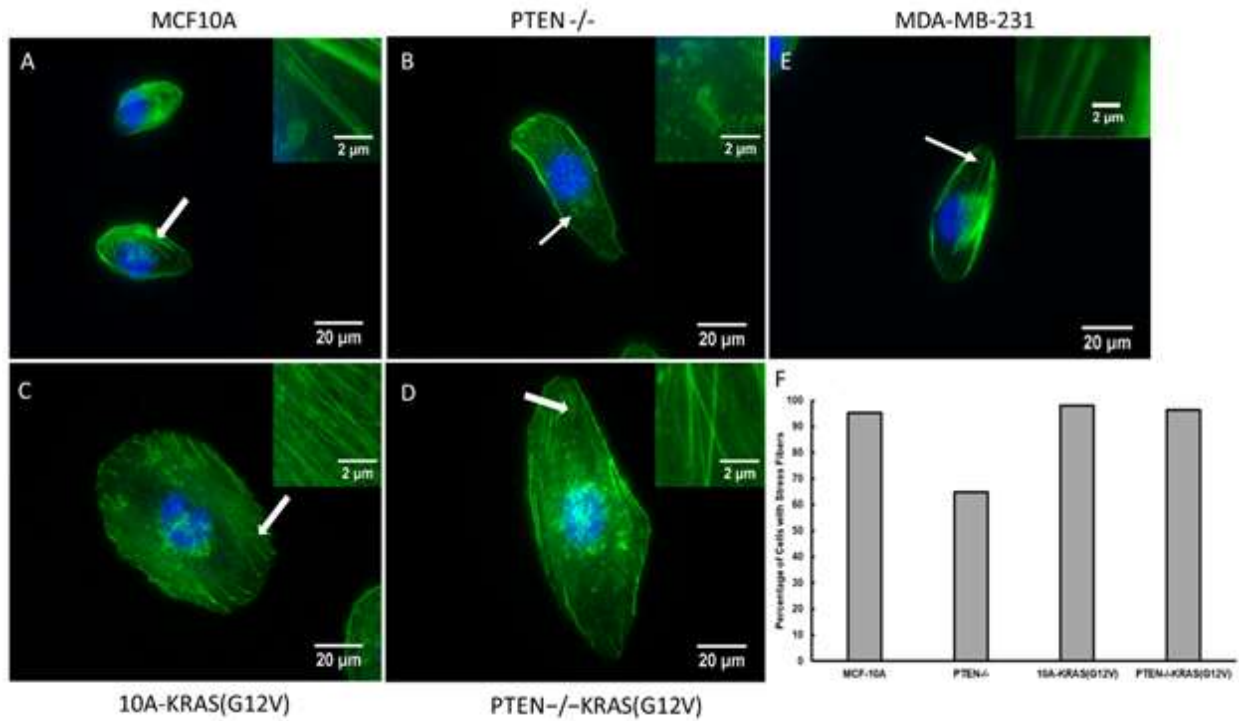


Figure 29. Immunofluorescence images of MCF-10A, PTEN^{-/-}, 10A-KRAS(G12V), PTEN^{-/-}-KRAS(G12V) and MDA-MB-231 cells stained with phalloidin (green) and DAPI (blue). Insets are zoomed views of the regions highlighted in the white boxes. (F) Percentage of cells with stress fibers for MCF-10A, PTEN^{-/-}, 10A-KRAS(G12V) and PTEN^{-/-}-KRAS(G12V) cells.

(50 ≤ N ≤ 63).

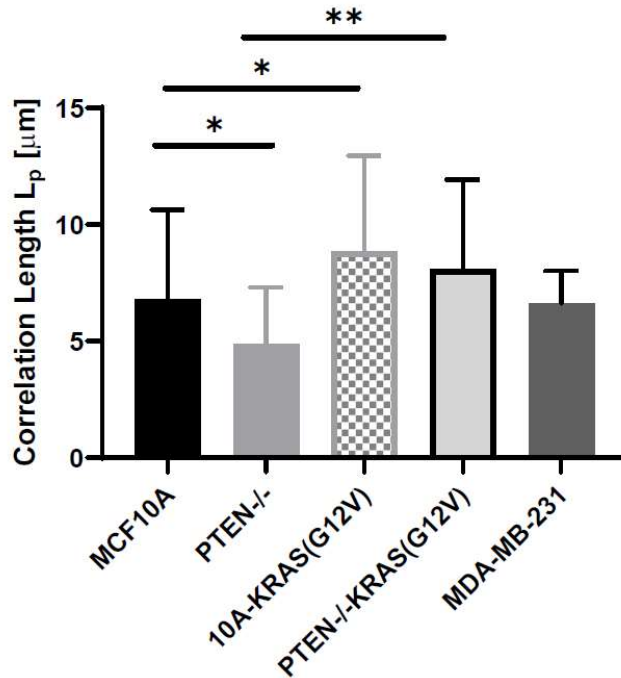


Figure 30. Traction force correlation length L_p of MCF-10A, PTEN^{-/-}, 10A-KRAS(G12V), PTEN^{-/-}-KRAS(G12V) and MDA-MB-231. Error bars represent SD. (N = 8)

4.3.5 Combination of KRAS overexpression and PTEN knockout drastically enhances cell directional migration.

Finally, we quantified the effects of knocking out PTEN and overexpressing KRAS on cell migration. Figure 31 demonstrates the trajectories of cells plot for each cell. The MCF-10A and PTEN^{-/-} cells move in a random walk fashion with their trajectories compacted around the starting point. The trajectories of KRAS(G12V) and PTEN^{-/-}-KRAS(G12V) cells extend out from the starting point. These differences in cell trajectories are quantified by the contour length of the trajectories, total displacement, and average speed (Figure 32). Among the four cell lines, PTEN^{-/-} cells have the lowest speed. KRAS(G12V) cells move faster than the MCF-10A cells. PTEN^{-/-}-KRAS(G12V) cells have the largest migration speed, which is approximately three times

higher than MCF-10A cell speed. The directional persistence in migration quantified using directional autocorrelation of the velocity vectors. In Figure 32D, MCF-10A and PTEN^{-/-} cells have similar the directional autocorrelation functions. The fast decay in the autocorrelation function suggests that the migrations of these cells do not have any directional persistence, i.e. they frequently change direction of migration. A weak correlation is observed for velocity vectors of KRAS(G12V) cells. Surprisingly, the PTEN^{-/-}-KRAS(G12V) cell line has a much lower decay in directional correlation, suggesting a highly directed migration pattern.

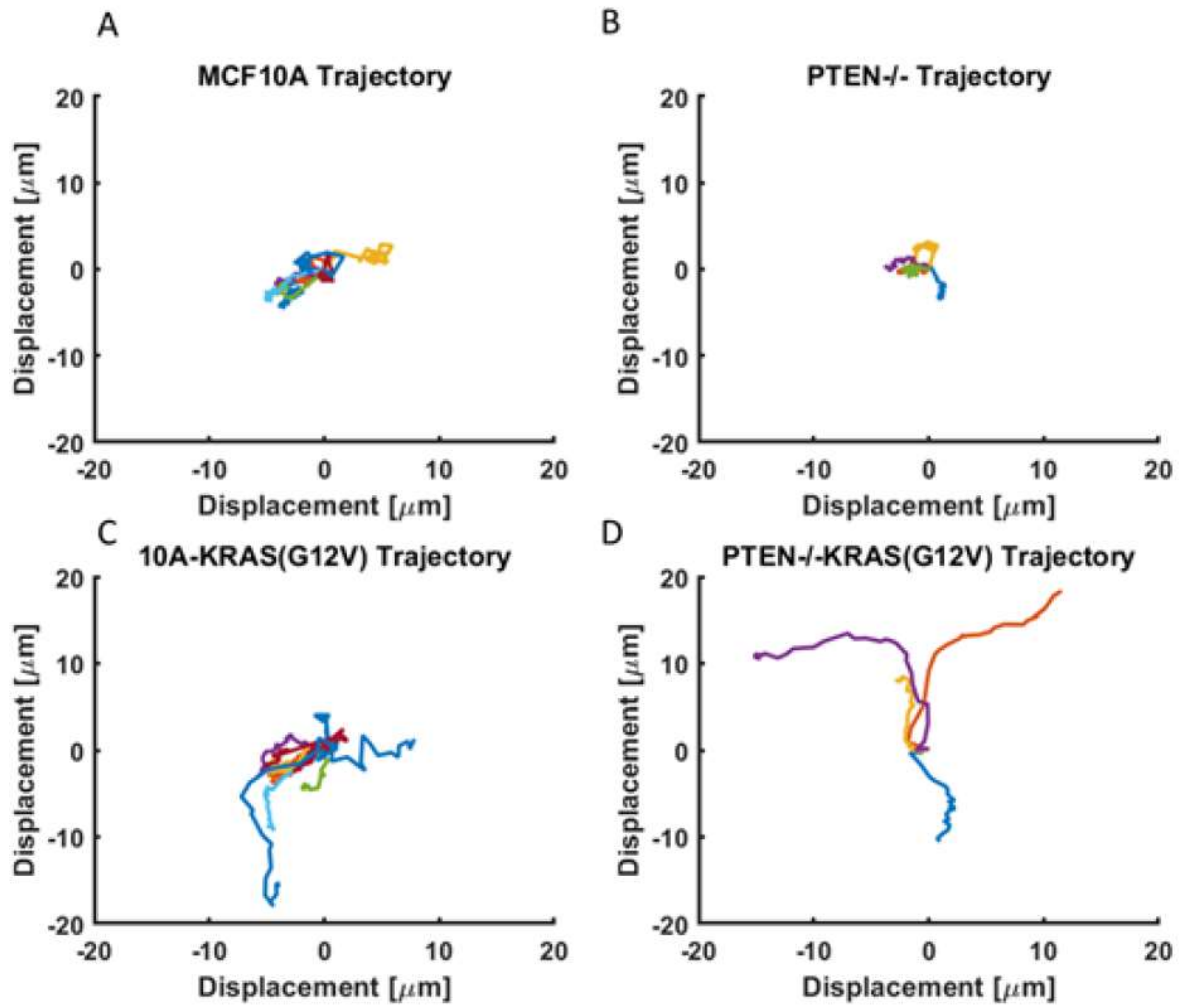


Figure 31. Trajectories of MCF-10A, PTEN^{-/-}, 10A-KRAS(G12V) and PTEN^{-/-}-KRAS(G12V) over 7.5 hours with time resolution of 15 minutes on 7500 kPa PAA gels. KRAS overexpression in both 10A-KRAS(G12V) and PTEN^{-/-}-KRAS(G12V) significantly changes the migration trajectories.

(4 ≤ N ≤ 9)

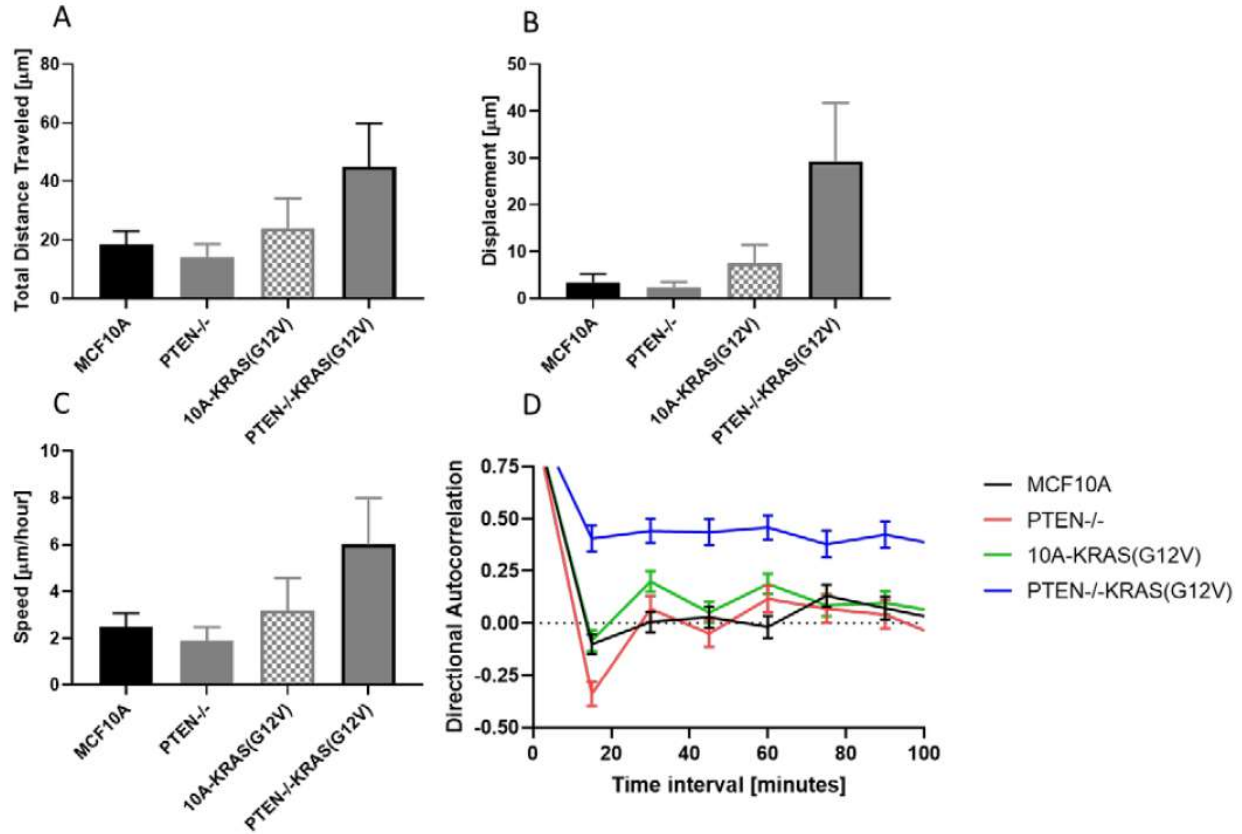


Figure 32.

(A) Total distance traveled, (B) Displacement, (C) Speed and (D) Directional Autocorrelation of MCF-10A, PTEN^{-/-}, 10A-KRAS(G12V) and PTEN^{-/-}-KRAS(G12V). KRAS overexpression slightly increases displacement and speed while combined PTEN^{-/-}-KRAS(G12V) exhibits much higher displacement and migration speed. Lower decay of directional autocorrelation of PTEN^{-/-}-KRAS(G12V) suggests that highly directed cell migration in cell with PTEN knockout and KRAS overexpression. Error bars represent SD. ($4 \leq N \leq 9$)

4.4 Discussion

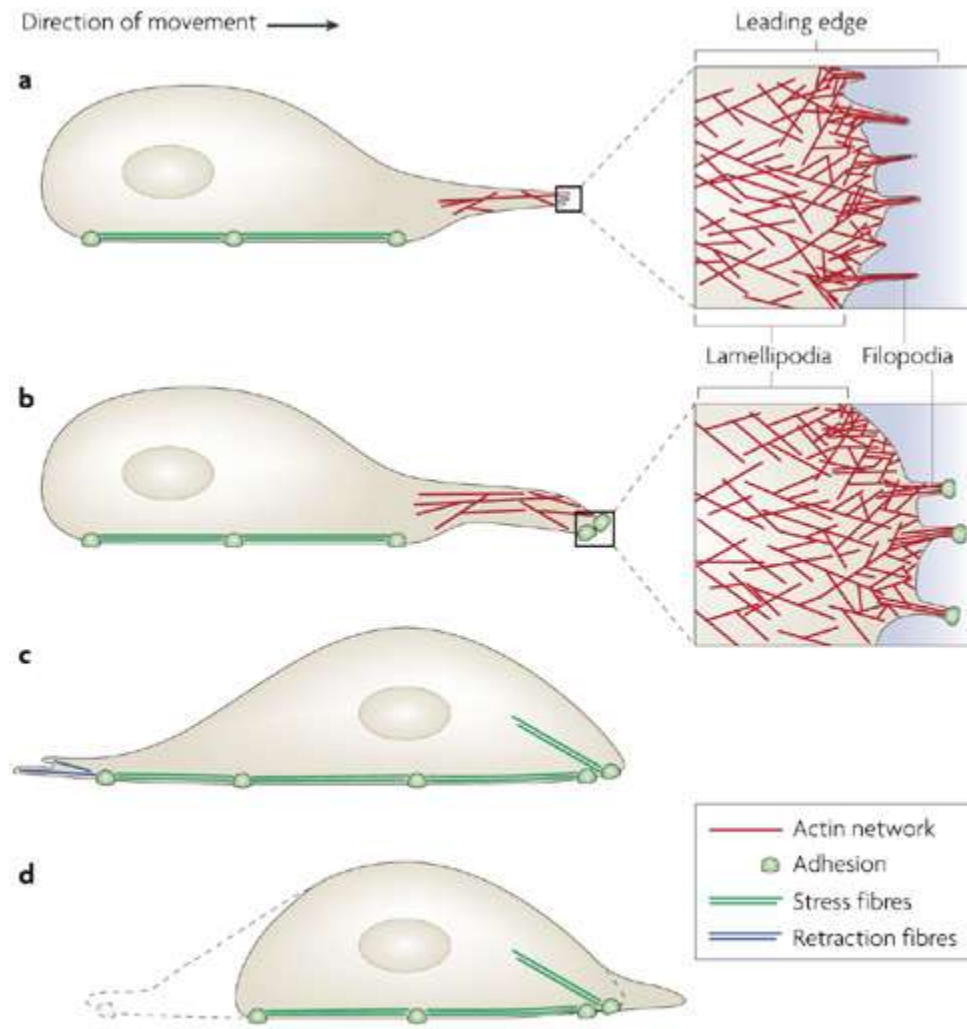
The tumor suppressor PTEN is an inhibitor of the PI3K/AKT pathway. Loss of PTEN in cells results in activation of the PI3K/AKT pathway. The oncogene KRAS promotes the activity of the MAPK/ERK pathway. [188, 203-206]. By comparing the mechanosensing of MCF-10A, PTEN^{-/-}, KRAS(G12V), and PTEN^{-/-}-KRAS(G12V) cells, we studied the differences and crosstalk between these pathways in regulating mechanosensing of breast epithelial cells.

Upon PTEN loss, PI3K is upregulated [90]. This activated PI3K pathway upregulates cofilin [207, 208], an actin-severing protein that promotes disassembly of actin filaments and stress fibers [209]. Furthermore, PTEN can influence actin organization through dephosphorylation of its lipid substrate phosphatidylinositol 3,4,5-trisphosphate (PIP3) to yield phosphatidylinositol 4,5-bisphosphate (PIP2) [197]. Most actin-severing proteins are downregulated by association with PIP2, whereas proteins that promote actin filament nucleation and bundling are typically activated by PIP2. Upregulated cofilin combined with reduced PIP2 results in actin disassembly [210]. The PTEN^{-/-} cells provided by Vitolo et al. were confirmed to have elevated activated cofilin and higher PIP3:PIP2 ratio than the control MCF-10A [211]. Indeed, our immunofluorescence study (Figure 29) reveals that a large percentage of PTEN^{-/-} cells lack actin stress fibers. The downregulated stress fiber in PTEN^{-/-} results in impaired force transmission, giving rise to lower L_p values and lower cell traction force.

In Figure 25, linear regression slopes of PTEN^{-/-} cells' spreading area, aspect ratio and traction force as functions of substrate rigidity are not significantly different from zero (Figure 25), i.e. the inability of PTEN^{-/-} cells to respond to changes in substrate rigidity. While this loss

of mechanosensing may be accounted for by the suppressed stress fiber formation in PTEN^{-/-}, there are many other proteins and molecular assemblies that can function as mechanotransducers (**Section 1.1.3**). More work is required to fully understand the molecular mechanism through which the PI3K/AKT pathways modulate cell mechanosensing.

Canonically, AKT promotes cell migration through the AKT-binding protein Girdin (girders of actin filament at the lamellipodia), which promotes the extension of lamellipodia at the leading-edges of migrating cells (Figure 33) [212, 213]. However, we observed that migration speed and directionality of PTEN^{-/-} are comparable to healthy MCF-10A. PI3K signaling pathway controls cofilin activity within the leading-edge. Enhancement of cofilin activity accelerates F-actin turnover and retrograde flow, resulting in the widening of the lamellipodia and reducing cell edge protrusion efficiency, lowering cell polarity and reduce directionality of migration [209]. Hence, while AKT enhances cell migration, the lack of stress fibers as well as reduced protrusion efficiency leads to a less directed migration pattern.



Nature Reviews | Molecular Cell Biology

Figure 33. The process of cell migration. Adapted from [214]. (A) Cell migration is initiated by protrusion of the cell's leading-edge, which is composed of structures called lamellipodia and filopodia. These protrusive structures are created by actin polymerization against cell membrane (B) Binding of integrins to ECM promote the formation of focal adhesion at the leading-edge contact sites (C) Next, the nucleus and the cell body are pushed forward through intracellular contraction forces mediated by actin-myosin interaction. (D) Gradual turnover of adhesion at the trailing edge allows disengagement of the cell from the substrates at its rear end, driving the cell towards its leading-edge.

Overexpressing activated KRAS leads to activation of the MAPK/ERK pathway, which results in hyperactivation of RhoA, a protein known to promote actin stress fiber formation. These long stress fibers in KRAS(G12V) cells (Figure 29 D) enhance force transmission and result in greater L_p value (Figure 30) and stronger traction force (Figure 26 C). The KRAS(G12V) cells can adjust their spreading area, polarization, and traction force level in response to substrate rigidity changes, suggesting that the activated MAPK/ERK promotes mechanosensing of these cells. It is worthwhile to note that, besides hyperactivating RhoA, MAPK/ERK pathway activation also enhances cell metabolism and growth [215-218]. KRAS(G12V) cells are substantially larger in spreading area than their control MCF-10A counterparts and an actual cancer cell MDA-MB-231 (Figure 26A).

KRAS overexpression also results in higher migration speed as well as directed cell migration. Cell migration is driven by actin polymerization at the leading-edge of lamellipodia, where WASP family verprolin-homologous proteins (WAVEs) activate Arp2/3 complex [219]. Overexpression of KRAS elevated expression of ERK, which directly phosphorylates WAVE2 regulatory complex [220]. This upregulated WAVE2 component promotes the actin-nucleating activity of Arp2/3, actin nucleating complex, resulting in effective leading-edge advancement during cell migration [221]. In addition, a tumor suppressor protein p27Kip1 (p27) is suppressed by high ERK activity [222]. p27 inhibits RhoA activation by interfering with the interaction between RhoA and its activators [223]. Active RhoA levels have been observed to increase in MEFs and smooth muscle cells lacking p27 [224, 225]. Combining high RhoA activity with effective leading-edge advancement and long-range force transmission due to robust actin stress fibers, KRAS(G12V) cells exhibit higher migratory potential than normal MF10A.

The result of both knocking out PTEN and overexpressing KRAS together is fascinating. The percentage of cells with stress fibers is higher in the PTEN^{-/-}-KRAS(G12V) cell line than in the PTEN^{-/-} cell line. The rescued stress fiber formation indicates that activating the MAPK/ERK pathway can overcome the suppressive effects of the PI3K pathway on stress fibers. The recovered stress fibers enable PTEN^{-/-}-KRAS(G12V) cells to generate stronger traction force. Moreover, PTEN^{-/-}-KRAS(G12V) cells are able to adjust their morphology and traction force in response to substrate rigidity, suggesting that activating the MAPK/ERK pathway can overcome the suppressive effects of the PI3K pathway on mechanosensing. More strikingly, PTEN^{-/-}-KRAS(G12V) cells have significantly higher migration speed and stronger directional persistence than the PTEN^{-/-} cells and the KRAS(G12V) cells (Figures 31, 32). These data suggest there is a crosstalk between the two pathways modulating cells' mechanosensing and directional migration.

The effects of crosstalk between the PI3K/AKT and MAPK/ERK pathways in promoting tumorigenesis have been observed by Thompson *et al* [190]. In their *in vivo* study, human breast epithelial cells MCF-10A and its daughter cell lines PTEN^{-/-}, 10A-KRAS(G12V), and PTEN^{-/-}-KRAS(G12V) were injected to mice and the survival of injected cells were monitored by bioluminescence (Fig.22). They observed that the bioluminescence of MCF-10A cells disappeared within 4 weeks, indicating the injected MCF-10A cells cannot survive in the new environment. The bioluminescence diminished by 96% for the PTEN^{-/-} and 94% for the 10A-KRAS(G12V) cells in 4 weeks after injection, indicating that only a very small population of these two cell lines can survive in the new environment. These survived cells behaved like dormant cancer cells, which survive for a long time in unfavorable environments without proliferating

and growing to form tumors. However, the bioluminescence intensity of PTEN^{-/-}-KRAS(G12V) cells increased with time, indicating their ability to survive and grow in the new environment. The rapidly growing PTEN^{-/-}-KRAS(G12V) cells at the injection site and formed tumors with measurable size. Together with these in vivo studies, our in vitro mechanobiology data on these cell lines suggest that the enhanced directional migration and mechanosensing are essential for metastatic breast cancer cells to invade secondary tissues and form tumors at places far away from the primary tumor site. Cancer cells lacking mechanosensing ability or directional migration will remain dormant. Similarly, a strong correlation between metastatic potential and the ability of mechanosensing and migration has been reported in many other types of cancer cells [66, 67, 73, 195, 196].

Our results also provide insights into the potential of components for mechanosensing as drug targets to suppress the metastasis of triple-negative breast cancer cells. The approach of targeting the actin cytoskeleton has been thought for a long time to be too toxic for clinical application [226]. It is clear that targeting actin cytoskeleton dynamics and/or contractility affects many processes in both cancer and normal cells, such as cell migration, which is a fundamental step in embryonic development and wound repair [227]. Despite the absence of specific drugs targeting actin, several drugs inhibiting focal adhesion kinase (FAK), a crucial mechanosensing component, have been developed. Defactinib, a FAK inhibitor V2-6063, is being tested in heavily pretreated patients with KRAS-mutant NSCLC in an ongoing phase 2 clinical trial [228, 229].

4.5 Summary

We demonstrated the different effects of the PI3K/AKT pathways and the MAPK/ERK pathways on mechanosensing and migration of breast epithelial cells. Activating PI3K pathway by knocking out PTEN results in loss of stress fiber in cells, leading to impaired mechanosensitivity. Activating the MAPK pathway through KRAS overexpression promotes stress fiber formation and retains MCF-10A cells' mechanosensing ability. More importantly, overexpressing KRAS in PTEN knockout cells restored the stress fiber formation, rescued their mechanosensing ability, and greatly enhanced directional cell migration. These results highlight the importance of crosstalk between the PI3K pathway and the MAPK pathway in promoting tumorigenic behavior of PTEN^{-/-}-KRAS(G12V) in vivo [190].

Chapter 5: Conclusion

Cancer is the second leading cause of mortality worldwide. The percentage of deaths associated with cancer continues to increase as average life expectancies increases due to advancement in medical fields. Therefore, cancer poses a serious problem in modern medicine. Unfortunately, it is a variety disease and this group of diseases is a major challenge for its specific diagnosis, followed by the efficacy of treatment. In order to address the increasing problem of cancer, understanding the intricacies of the process involved in tumor initiation and progression is the key to develop new therapies.

This dissertation presents the first set of experiments to characterize the effects of three canonical biomarkers of cancer, i.e. vimentin, PTEN and KRAS, on the ability of cells to sense changes in substrate rigidity. The mutations in these three biomarkers have unique effects on stress fiber formation, force transmission, and hence cell mechanosensing. A simplified summary of our results on the effects of vimentin knockdown, PTEN knockout, KRAS overexpression and double mutated PTEN knockout and KRAS overexpression cell morphology, actin organization, mechanosensing ability and directional migration are shown in Table 2 below:

	Vimentin knockdown	PTEN knockout	KRAS Overexpressed	PTEN Knockout KRAS Overexpressed
Cell Size	Slightly decreases	Slightly increases	Significantly increases	Significantly increases
Cell Polarity	Slightly decreases	Decreases	Significantly increases	Significantly increases
Actin organization	Shorter stress fibers	Less stress fibers	Long stress fibers	Long stress fibers
Mechanosensing	Yes	No	Yes	Yes
Migration	Reduces	Reduces	Enhances	Significantly Enhances

Table 2. Summary of characterization of shVim, PTEN^{-/-}, 10A-KRAS(G12V), and PTEN^{-/-}-KRAS(G12V) cells compared to their healthy control.

Vimentin knockdown alters the cytoskeleton structure and reduces the distance of force transmission. However, knocking down vimentin does not inhibit the formation of actin stress fibers and has no apparent effects on the ability of cells to sense substrate rigidity. Knocking out PTEN inhibits stress fiber formation cells and abolish cells' ability to sense substrate rigidity. Overexpressing KRAS promotes stress fiber formation in cells regardless of PTEN expression. This reformation of stress fiber rescues the mechanosensing ability in PTEN knockout cells.

Additionally, the thesis highlights the importance of stress fibers organization in migratory persistence. Vimentin intermediate filaments help orient stress fibers and promote single-cell directed migration. PTEN knockout disrupts stress fibers organization. As a result, breast epithelial cells with PTEN knockout retains the non-motile trait of the epithelial phenotype. KRAS overexpression, on the other hand, retains actin stress fibers structure and

promotes directed cell migration. Although PTEN knockout and KRAS overexpression have opposite effects on cell migration, the crosstalk between PI3K/AKT pathway and MAPK/ERK pathway significantly enhances the directional migration in cells with double mutated pathways.

Chapter 6: Future directions

6.1 Effects of Vimentin Knockdown, PTEN knockout and KRAS

overexpression on focal adhesion

Maximum traction stress, while providing valuable information about the maximum stress that focal adhesions can withhold, does not allow us to quantify the stress applied on the integrin cluster due to the resolution of the traction force microscopy used. Our FEM mesh size is approximately $5 \mu\text{m}^2$, which is larger than the actual size of a matured focal adhesion. A study quantifying the focal adhesion size of MEFs cell using vinculin, talin, and FAK staining put a rough estimate of a matured adhesion size to be $3 \mu\text{m}^2$ [230]. Figure 34 showing total internal reflection fluorescence microscopy (TIRF) images of MCF-10A, PTEN^{-/-}, 10A-KRAS(G12V), and PTEN^{-/-}-KRAS(G12V) cells stained for actin (red) and vinculin (green) from our lab indicates not all cells exhibit elongated mature focal adhesion especially on smaller cells like MCF-10A and PTEN^{-/-}. Thus, a study focusing on focal adhesion/integrin using AFM or Single Cell Force Spectroscopy is needed to fully understand the effects of these cancerous mutations (vimentin, PTEN and KRAS) on mechanotransduction/mechanosensing from the adhesion perspective.

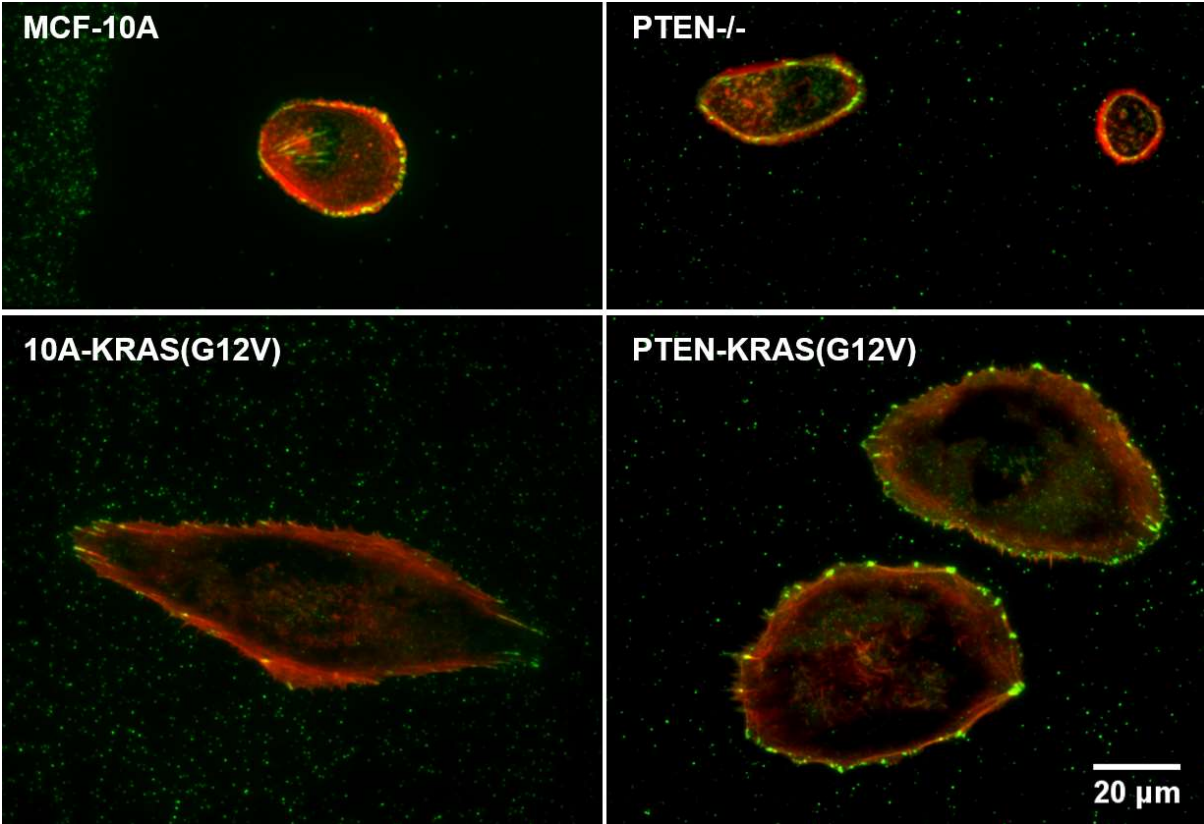


Figure 34. Total internal reflection fluorescence microscopy of MCF-10A, PTEN^{-/-}, 10A-KRAS(G12V), and PTEN^{-/-}-KRAS(G12V) cells stained with phalloidin (red) and vinculin (green).

6.2 Dynamic change of cell traction force at the initial stage of cell-substrate contact and during cell migration

In addition to measuring the force that cells apply at a single point in time, we can track how much force the cells apply on the substrate over time. After the cell is seeded onto the beads coated gel, cell morphology and beads position can be captured on the microscope with a working environment chamber. This environmental control would give us the ability to explore cell dynamics such as traction evolution, coupled with cell spreading area and potentially cytoskeleton/adhesion grow. The preliminary results on the maximum stress growth profiles are plotted in Figures 35,36. We observed that traction stress exhibits a two-phase growth for all cells except KRAS(G12V) and PTEN-/-KRAS(G12V). Interestingly, normalized maximum stress growth profiles are similar for healthy fibroblasts and vimentin knockdown. Since the amount of stress applied on the focal adhesion is correlated with the maximum stress, this (normalized) maximum stress growth profile can give us some idea about how the focal adhesion dynamics (i.e. focal adhesion recruitment rate/ lifetime stability) [173] can regulate mechanosensing, which has not yet been studied in this thesis.

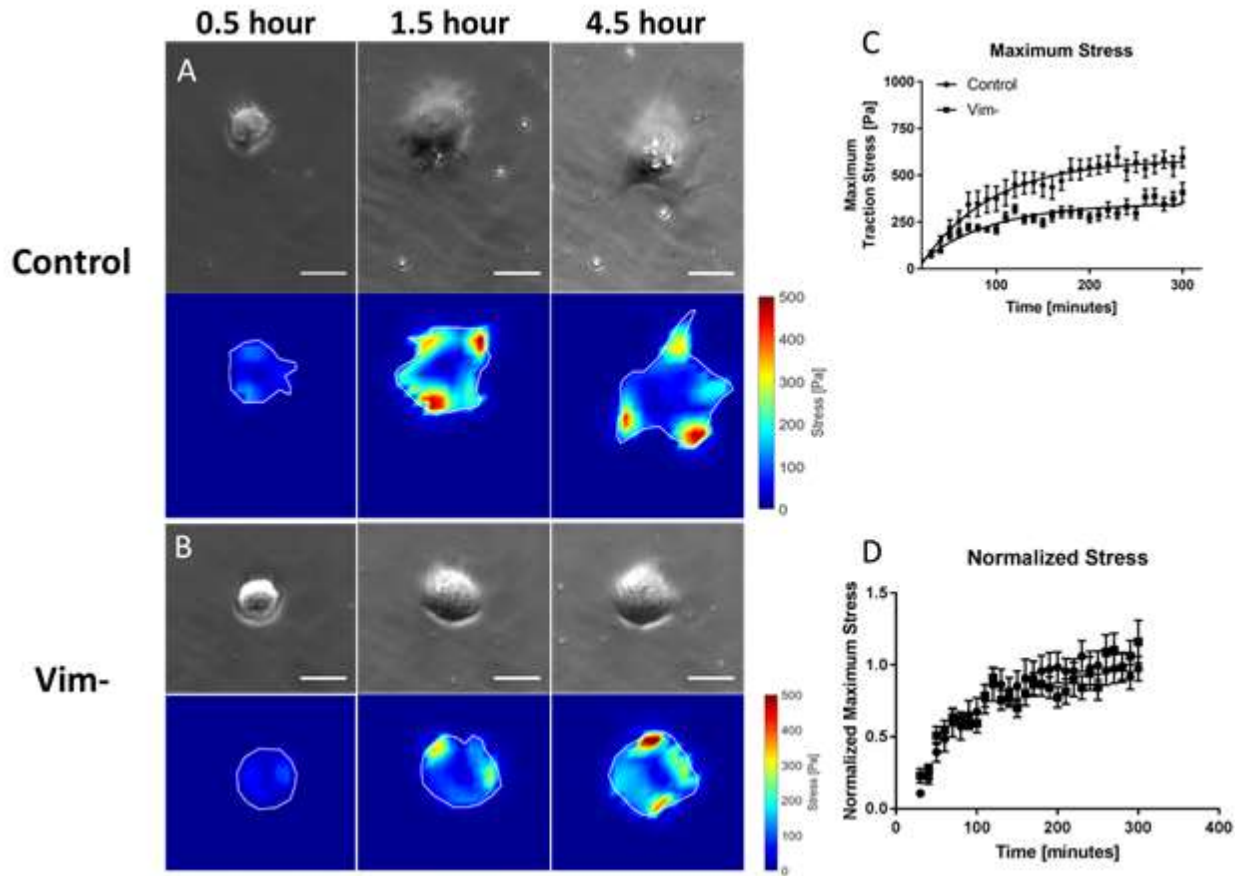


Figure 35. Time-lapse phase contrast images and stress heat maps of control (A) and vimentin knockdown (B) 3T3 fibroblasts at 0.5, 1.5, 3.0 and 4.5 hour. Scale bar = 20 μm . Maximum stress (C) and normalized maximum stress (D) over time comparison between Control (Round) and Vim- (Square) 3T3 fibroblasts. The exponential model used to fit is $Y = Y_0 + (Plateau - Y_0) * (1 - e^{-kt})$. The exponential time constant t is 75.9 and 77.7 minutes for control and vimentin knockdown cells respectively. Control cells plateaued out approximately in the range of 530-620 Pa while vimentin knockdown cells plateaued out at 330-390 Pa. Control 3T3 fibroblasts have higher plateau maximum stress and higher growth rate of stress compared to vimentin knockdown cells. However, the normalized rate of increase (normalized against plateau stress)

is the same for both populations. Values represent the mean of 14 cells from three independent experiments (N = 14, n = 3). Error bars indicate SD.

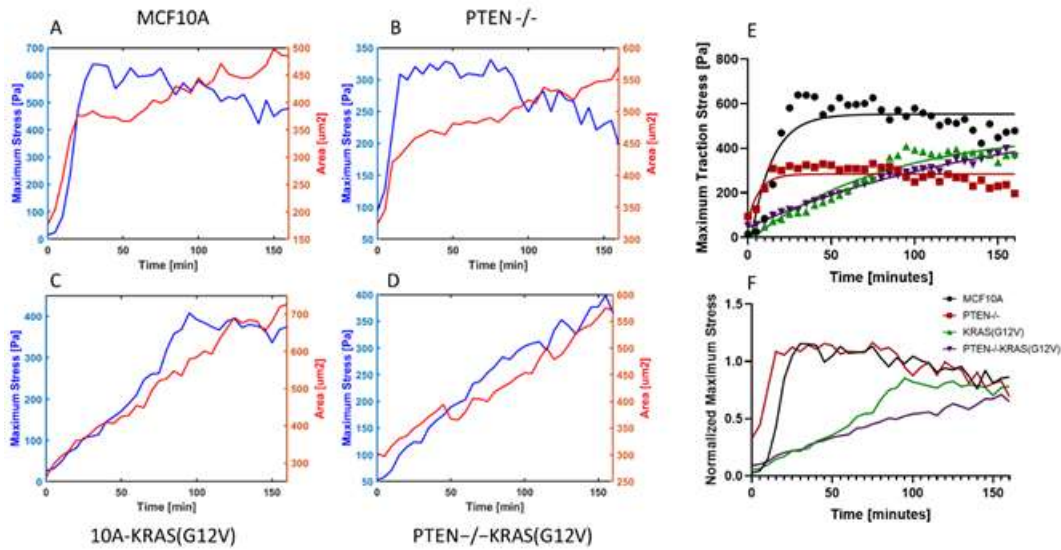


Figure 36. (A-D) Growth profile of maximum stress and cell area of one MCF-10A, PTEN^{-/-}, 10A-KRAS(G12V), PTEN^{-/-}-KRAS(G12V) and MDA-MB-231 cell. (B) Maximum stress is then fitted to function $Y = Y_0 + (Plateau - Y_0) * (1 - e^{-kt})$ to find the maximum plateau stress of each group. (F) The maximum stress over time is normalized against expected plateau of MCF-10A, PTEN^{-/-}, 10A-KRAS(G12V), PTEN^{-/-}-KRAS(G12V) cells. Overexpressing KRAS completely changes the growth profile of MCF-10A cells. ($3 \leq N \leq 6$, $2 \leq n \leq 3$)

6.3 Soft gel regime, 3D deformation and cluster studies

Finally, during our experiment with traction force on an extremely soft gel (≤ 2000 Pa), we detected a significant 3-dimensional deformation of the gel underneath the cell (Figure 37 C, D). ROCK inhibited cells do not cause such deformation, confirming that the 3d deformation is force-mediated by the cell. Comparing the z-plane of focused beads on the substrate in

regions with and without cell, we found that the deformation is into the gel (indentation). Thus, this is not due to cells pulling on gel's surface. Using live staining actin, we image the cell on a soft gel with surface coated with fluorescent beads under a confocal microscope (shown in Figure 37B). We observed that the cell assumed a spherical/ovoid shape that directly projects into the gel surface ($\approx 5\mu\text{m}$).

Furthermore, the morphology reveals that cells with cell-cell contact (cells in a cluster) exhibit drastically different morphology compared to cells in solitary (Figure 37A). While cell-cell adhesion affects cell mechanical properties and morphology [231], Figure 37A seems to indicate that cells in solitary tend to spread into the gel, not just on the gel's surface. Cells with cell-cell contact, on the other hand, mostly spread on the gel surface. In metastatic cancer cells, there are actin-rich structures present at the basal surfaces of the cells capable of projecting into and crossing extracellular barriers called invadopodia [232]. Understanding how these observed projection are formed/regulated in comparison with invadopodia, would provide a better understanding of the effects of cancerous mutations on cells in soft environments (native breast tissue rigidity) where actin stress fibers are not frequently formed and migration is limited [233, 234].

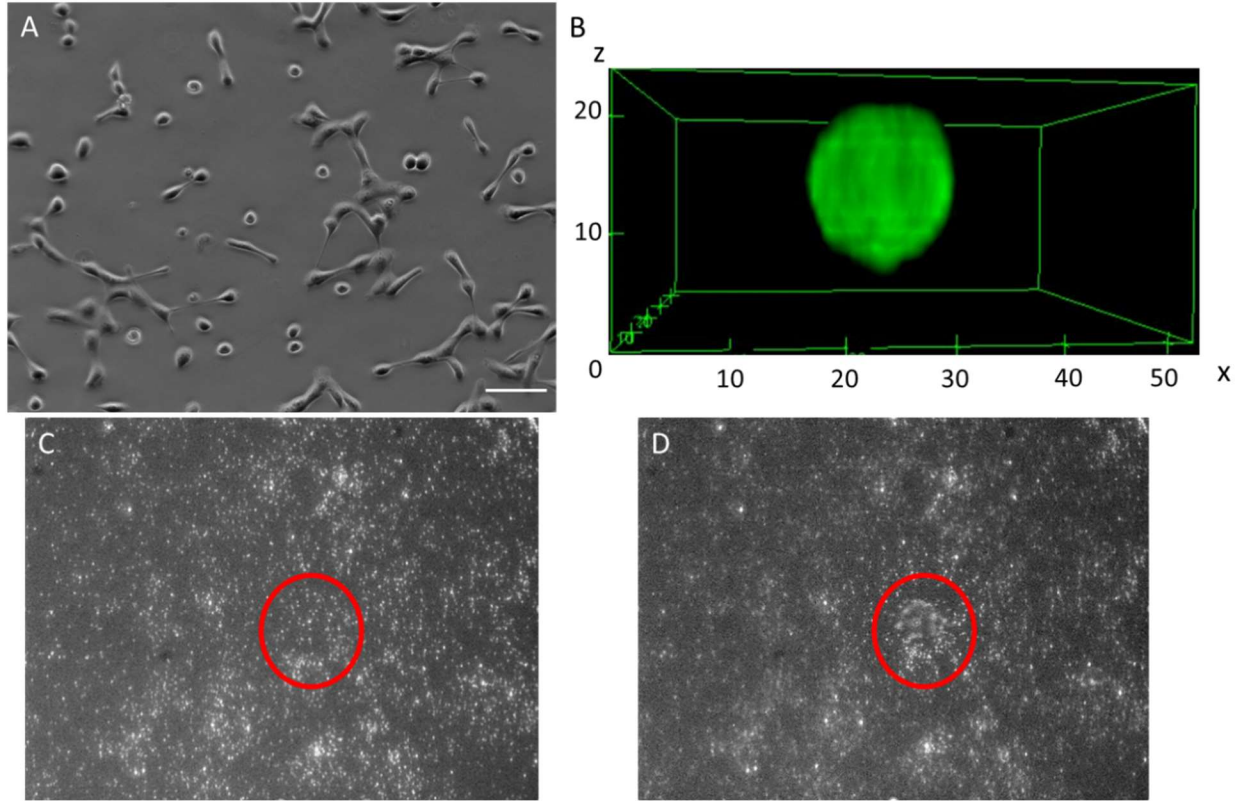


Figure 37.(A) MCF-10A cells on 800 Pa gels. Cells exhibiting cell-cell contacts have drastically different phenotypes than cells in solitary. Scale bar = 100 μm . (B) Confocal 3D view of an MCF-10A cells (actin-GFP) on/in 800 Pa gels. The gel surface is at $z = 13\mu\text{m}$ (label with red fluorescent beads – not shown). (C and D) Relaxed and loaded beads image of MCF-10A cells on 800 Pa gels. Red circle indicates the location of the cell and location of the beads with z-displacement.

Reference

1. Georges, P.C. and P.A. Janmey, *Cell type-specific response to growth on soft materials*. Journal of Applied Physiology, 2005. **98**(4): p. 1547-1553.
2. Ng, M.R., et al., *Substrate stiffness regulates cadherin-dependent collective migration through myosin-II contractility*. The Journal of cell biology, 2012. **199**(3): p. 545-563.
3. Park, J.S., et al., *The effect of matrix stiffness on the differentiation of mesenchymal stem cells in response to TGF- β* . Biomaterials, 2011. **32**(16): p. 3921-3930.
4. Engler, A.J., et al., *Matrix elasticity directs stem cell lineage specification*. Cell, 2006. **126**(4): p. 677-89.
5. Chen, Y., et al., *Receptor-mediated cell mechanosensing*. Molecular biology of the cell, 2017. **28**(23): p. 3134-3155.
6. Jaalouk, D.E. and J. Lammerding, *Mechanotransduction gone awry*. Nature Reviews Molecular Cell Biology, 2009. **10**: p. 63.
7. Fedorchak, G.R., A. Kaminski, and J. Lammerding, *Cellular mechanosensing: getting to the nucleus of it all*. Progress in biophysics and molecular biology, 2014. **115**(2-3): p. 76-92.
8. Wang, N., *Review of Cellular Mechanotransduction*. Journal of physics D: Applied physics, 2017. **50**(23): p. 233002.
9. Orr, A.W., et al., *Mechanisms of Mechanotransduction*. Developmental Cell, 2006. **10**(1): p. 11-20.
10. Peyronnet, R., et al., *Mechanosensitive channels: feeling tension in a world under pressure*. Frontiers in Plant Science, 2014. **5**: p. 558.
11. Hayakawa, K., H. Tatsumi, and M. Sokabe, *Actin stress fibers transmit and focus force to activate mechanosensitive channels*. Journal of Cell Science, 2008. **121**(4): p. 496.
12. Poolman, B., J.J. Spitzer, and J.M. Wood, *Bacterial osmosensing: roles of membrane structure and electrostatics in lipid-protein and protein-protein interactions*. Biochim Biophys Acta, 2004. **1666**(1-2): p. 88-104.
13. Trubelja, A. and G. Bao, *Molecular mechanisms of mechanosensing and mechanotransduction in living cells*. Extreme Mechanics Letters, 2018. **20**: p. 91-98.
14. Hoffman, B.D., C. Grashoff, and M.A. Schwartz, *Dynamic molecular processes mediate cellular mechanotransduction*. Nature, 2011. **475**: p. 316.
15. DuFort, C.C., M.J. Paszek, and V.M. Weaver, *Balancing forces: architectural control of mechanotransduction*. Nature Reviews Molecular Cell Biology, 2011. **12**: p. 308.
16. Ohashi, K., S. Fujiwara, and K. Mizuno, *Roles of the cytoskeleton, cell adhesion and rho signalling in mechanosensing and mechanotransduction*. The Journal of Biochemistry, 2017. **161**(3): p. 245-254.
17. Kleinsmith, J.H.G.P.B.L.J., *Becker's World Of The Cell*. 9th ed. 2016: Pearson.
18. Brouhard, G.J. and L.M. Rice, *Microtubule dynamics: an interplay of biochemistry and mechanics*. Nature Reviews Molecular Cell Biology, 2018. **19**(7): p. 451-463.
19. Hinchcliffe, E.H., *The centrosome and bipolar spindle assembly: does one have anything to do with the other?* Cell cycle (Georgetown, Tex.), 2011. **10**(22): p. 3841-3848.
20. Prasad, R.M., X. Jin, and S.M. Nauli, *Sensing a sensor: identifying the mechanosensory function of primary cilia*. Biosensors (Basel), 2014. **4**(1): p. 47-62.
21. Kaverina, I., et al., *Tensile stress stimulates microtubule outgrowth in living cells*. J Cell Sci, 2002. **115**(Pt 11): p. 2283-91.

22. Mendez, M.G., S.-I. Kojima, and R.D. Goldman, *Vimentin induces changes in cell shape, motility, and adhesion during the epithelial to mesenchymal transition*. The FASEB Journal, 2010. **24**(6): p. 1838-1851.
23. Janmey, P.A., et al., *Viscoelastic properties of vimentin compared with other filamentous biopolymer networks*. The Journal of cell biology, 1991. **113**(1): p. 155-160.
24. Mendez, M.G., D. Restle, and P.A. Janmey, *Vimentin Enhances Cell Elastic Behavior and Protects against Compressive Stress*. Biophysical Journal, 2014. **107**(2): p. 314-323.
25. Robert, A., C. Hookway, and V.I. Gelfand, *Intermediate filament dynamics: What we can see now and why it matters*. BioEssays : news and reviews in molecular, cellular and developmental biology, 2016. **38**(3): p. 232-243.
26. Goldman, R.D., et al., *Inroads into the structure and function of intermediate filament networks*. J Struct Biol, 2012. **177**(1): p. 14-23.
27. Tsuruta, D. and J.C.R. Jones, *The vimentin cytoskeleton regulates focal contact size and adhesion of endothelial cells subjected to shear stress*. Journal of Cell Science, 2003. **116**(24): p. 4977.
28. Weber, Gregory F., Maureen A. Bjerke, and Douglas W. DeSimone, *A Mechanoresponsive Cadherin-Keratin Complex Directs Polarized Protrusive Behavior and Collective Cell Migration*. Developmental Cell, 2012. **22**(1): p. 104-115.
29. Jiu, Y., et al., *Bidirectional Interplay between Vimentin Intermediate Filaments and Contractile Actin Stress Fibers*. Cell Reports, 2015. **11**(10): p. 1511-1518.
30. Gregor, M., et al., *Mechanosensing through focal adhesion-anchored intermediate filaments*. The FASEB Journal, 2014. **28**(2): p. 715-729.
31. Kim, J., et al., *Vimentin filaments regulate integrin-ligand interactions by binding to the cytoplasmic tail of integrin $\beta 3$* . J Cell Sci, 2016. **129**(10): p. 2030-42.
32. Pollard, T.D. and J.A. Cooper, *Actin, a Central Player in Cell Shape and Movement*. Science, 2009. **326**(5957): p. 1208.
33. Schwarz, U.S. and M.L. Gardel, *United we stand – integrating the actin cytoskeleton and cell–matrix adhesions in cellular mechanotransduction*. Journal of Cell Science, 2012. **125**(13): p. 3051-3060.
34. Mogilner, A. and G. Oster, *Force Generation by Actin Polymerization II: The Elastic Ratchet and Tethered Filaments*. Biophysical Journal, 2003. **84**(3): p. 1591-1605.
35. Kuo, J.-C., *Chapter Three - Focal Adhesions Function as a Mechanosensor*, in *Progress in Molecular Biology and Translational Science*, A.J. Engler and S. Kumar, Editors. 2014, Academic Press. p. 55-73.
36. Nukuda, A., et al., *Stiff substrates increase YAP-signaling-mediated matrix metalloproteinase-7 expression*. Oncogenesis, 2015. **4**(9): p. e165-e165.
37. Bershadsky, A.D., et al., *Assembly and mechanosensory function of focal adhesions: experiments and models*. Eur J Cell Biol, 2006. **85**(3-4): p. 165-73.
38. Wu, C., *Focal adhesion: a focal point in current cell biology and molecular medicine*. Cell Adh Migr, 2007. **1**(1): p. 13-8.
39. Humphries, J.D., A. Byron, and M.J. Humphries, *Integrin ligands at a glance*. Journal of Cell Science, 2006. **119**(19): p. 3901.
40. Steger M, A.G., Bremus-Köbberling E, et al, *Nanoscale biofunctionalization of polymer surfaces by laser treatment for controlled cellular differentiation.*, in *Optically Induced Nanostructures: Biomedical and Technical Applications*, O.A. König K, Editor. 2015, De Gruyter: Berlin.
41. Hynes, R.O., *Integrins*. Cell. **110**(6): p. 673-687.
42. Liu, J., et al., *Talin determines the nanoscale architecture of focal adhesions*. Proceedings of the National Academy of Sciences, 2015. **112**(35): p. E4864.

43. Al Tanoury, Z., et al., *Genes involved in cell adhesion and signaling: a new repertoire of retinoic acid receptor target genes in mouse embryonic fibroblasts*. Journal of Cell Science, 2014. **127**(3): p. 521.
44. Zhang, X., et al., *Talin depletion reveals independence of initial cell spreading from integrin activation and traction*. Nat Cell Biol, 2008. **10**(9): p. 1062-8.
45. Xu, W., H. Baribault, and E.D. Adamson, *Vinculin knockout results in heart and brain defects during embryonic development*. Development, 1998. **125**(2): p. 327-37.
46. Volberg, T., et al., *Focal adhesion formation by F9 embryonal carcinoma cells after vinculin gene disruption*. J Cell Sci, 1995. **108 (Pt 6)**: p. 2253-60.
47. Papagrigoriou, E., et al., *Activation of a vinculin-binding site in the talin rod involves rearrangement of a five-helix bundle*. Embo j, 2004. **23**(15): p. 2942-51.
48. del Rio, A., et al., *Stretching Single Talin Rod Molecules Activates Vinculin Binding*. Science, 2009. **323**(5914): p. 638.
49. Gingras, A.R., et al., *Structural and dynamic characterization of a vinculin binding site in the talin rod*. Biochemistry, 2006. **45**(6): p. 1805-17.
50. Zhu, J., et al., *Structure of a complete integrin ectodomain in a physiologic resting state and activation and deactivation by applied forces*. Molecular cell, 2008. **32**(6): p. 849-861.
51. Puklin-Faucher, E., et al., *How the headpiece hinge angle is opened: new insights into the dynamics of integrin activation*. Journal of Cell Biology, 2006. **175**(2): p. 349-360.
52. Sawada, Y., et al., *Force sensing by mechanical extension of the Src family kinase substrate p130Cas*. Cell, 2006. **127**(5): p. 1015-26.
53. Pasapera, A.M., et al., *Myosin II activity regulates vinculin recruitment to focal adhesions through FAK-mediated paxillin phosphorylation*. The Journal of Cell Biology, 2010. **188**(6): p. 877-890.
54. Hanahan, D. and R.A. Weinberg, *The hallmarks of cancer*. Cell, 2000. **100**(1): p. 57-70.
55. Talmadge, J.E. and I.J. Fidler, *AACR Centennial Series: The Biology of Cancer Metastasis: Historical Perspective*. Cancer Research, 2010. **70**(14): p. 5649.
56. Sporn, M.B., *The War on Cancer: A Reviewa*. Annals of the New York Academy of Sciences, 1997. **833**(1): p. 137-146.
57. Jiang, W.G., et al., *Tissue invasion and metastasis: Molecular, biological and clinical perspectives*. Seminars in Cancer Biology, 2015. **35**: p. S244-S275.
58. Nakaya, Y. and G. Sheng, *Epithelial to mesenchymal transition during gastrulation: an embryological view*. Dev Growth Differ, 2008. **50**(9): p. 755-66.
59. Kalcheim, C., *Epithelial-Mesenchymal Transitions during Neural Crest and Somite Development*. Journal of clinical medicine, 2015. **5**(1): p. 1.
60. Acloque, H., et al., *Epithelial-mesenchymal transitions: the importance of changing cell state in development and disease*. J Clin Invest, 2009. **119**(6): p. 1438-49.
61. Roche, J., *The Epithelial-to-Mesenchymal Transition in Cancer*. Cancers, 2018. **10**(2): p. 52.
62. Attar, R., et al., *Natural products are the future of anticancer therapy: Preclinical and clinical advancements of *Viscum album* phytometabolites*. Cell Mol Biol (Noisy-le-grand), 2015. **61**(6): p. 62-8.
63. Dongre, A. and R.A. Weinberg, *New insights into the mechanisms of epithelial–mesenchymal transition and implications for cancer*. Nature Reviews Molecular Cell Biology, 2019. **20**(2): p. 69-84.
64. Li, Y., et al., *Quantitative phase imaging reveals matrix stiffness-dependent growth and migration of cancer cells*. Scientific Reports, 2019. **9**(1): p. 248.
65. Yang, B., et al., *Stopping Transformed Growth with Cytoskeletal Proteins: Turning a Devil into an Angel*. bioRxiv, 2018: p. 221176.

66. Kraning-Rush, C.M., J.P. Califano, and C.A. Reinhart-King, *Cellular traction stresses increase with increasing metastatic potential*. PLoS One, 2012. **7**(2): p. e32572.
67. McGrail, D.J., Q.M.N. Kieu, and M.R. Dawson, *The malignancy of metastatic ovarian cancer cells is increased on soft matrices through a mechanosensitive Rho-ROCK pathway*. Journal of cell science, 2014. **127**(Pt 12): p. 2621-2626.
68. Oudin, M.J. and V.M. Weaver, *Physical and Chemical Gradients in the Tumor Microenvironment Regulate Tumor Cell Invasion, Migration, and Metastasis*. Cold Spring Harb Symp Quant Biol, 2016. **81**: p. 189-205.
69. Irby, R.B. and T.J. Yeatman, *Role of Src expression and activation in human cancer*. Oncogene, 2000. **19**(49): p. 5636-42.
70. Weaver, V.M., et al., *beta4 integrin-dependent formation of polarized three-dimensional architecture confers resistance to apoptosis in normal and malignant mammary epithelium*. Cancer cell, 2002. **2**(3): p. 205-216.
71. Brock, A., S. Krause, and D.E. Ingber, *Control of cancer formation by intrinsic genetic noise and microenvironmental cues*. Nature Reviews Cancer, 2015. **15**(8): p. 499-509.
72. Gkretsi, V. and T. Stylianopoulos, *Cell Adhesion and Matrix Stiffness: Coordinating Cancer Cell Invasion and Metastasis*. Frontiers in Oncology, 2018. **8**(145).
73. Li, X. and J. Wang, *Mechanical tumor microenvironment and transduction: cytoskeleton mediates cancer cell invasion and metastasis*. International Journal of Biological Sciences, 2020. **16**(12): p. 2014-2028.
74. Paszek, M.J., et al., *Tensional homeostasis and the malignant phenotype*. Cancer Cell, 2005. **8**(3): p. 241-54.
75. Shi, Q., et al., *Rapid disorganization of mechanically interacting systems of mammary acini*. Proceedings of the National Academy of Sciences, 2014. **111**(2): p. 658.
76. Kopanska, K.S., et al., *Tensile Forces Originating from Cancer Spheroids Facilitate Tumor Invasion*. PloS one, 2016. **11**(6): p. e0156442-e0156442.
77. Zöller, M., *CD44: can a cancer-initiating cell profit from an abundantly expressed molecule?* Nature Reviews Cancer, 2011. **11**(4): p. 254-267.
78. Ridley, A.J., et al., *Cell Migration: Integrating Signals from Front to Back*. Science, 2003. **302**(5651): p. 1704.
79. Vogel, W.F., R. Abdulhusein, and C.E. Ford, *Sensing extracellular matrix: An update on discoidin domain receptor function*. Cellular Signalling, 2006. **18**(8): p. 1108-1116.
80. Evans, R.M., *Vimentin: the conundrum of the intermediate filament gene family*. 1998. **20**(1): p. 79-86.
81. Thiery, J.P., *Epithelial-mesenchymal transitions in tumour progression*. Nat Rev Cancer, 2002. **2**(6): p. 442-54.
82. Liu, C.-Y., et al., *Vimentin contributes to epithelial-mesenchymal transition cancer cell mechanics by mediating cytoskeletal organization and focal adhesion maturation*. Oncotarget, 2015. **6**(18): p. 15966-15983.
83. Prahlaad, V., et al., *Rapid movements of vimentin on microtubule tracks: kinesin-dependent assembly of intermediate filament networks*. J Cell Biol, 1998. **143**(1): p. 159-70.
84. Leduc, C. and S. Etienne-Manneville, *Regulation of microtubule-associated motors drives intermediate filament network polarization*. J Cell Biol, 2017. **216**(6): p. 1689-1703.
85. Esue, O., et al., *A direct interaction between actin and vimentin filaments mediated by the tail domain of vimentin*. J Biol Chem, 2006. **281**(41): p. 30393-9.
86. Svitkina, T.M., A.B. Verkhovsky, and G.G. Borisy, *Plectin sidearms mediate interaction of intermediate filaments with microtubules and other components of the cytoskeleton*. J Cell Biol, 1996. **135**(4): p. 991-1007.

87. Terriac, E., et al., *Vimentin Levels and Serine 71 Phosphorylation in the Control of Cell-Matrix Adhesions, Migration Speed, and Shape of Transformed Human Fibroblasts*. *Cells*, 2017. **6**(1).
88. Kreis, S., et al., *The intermediate filament protein vimentin binds specifically to a recombinant integrin $\alpha 2/\beta 1$ cytoplasmic tail complex and co-localizes with native $\alpha 2/\beta 1$ in endothelial cell focal adhesions*. *Experimental Cell Research*, 2005. **305**(1): p. 110-121.
89. Avtanski, D. *Contribution of Extracellular Matrix to EMT*. *Adhesion/ECM/Cytoskeleton 2018*; Available from: <https://www.cellsignal.com/contents/science-cst-pathways-adhesion-ecm-cytoskeleton/contribution-of-extracellular-matrix-to-emt/pathways-emt-extracellular-matrix>.
90. Carracedo, A. and P.P. Pandolfi, *The PTEN–PI3K pathway: of feedbacks and cross-talks*. *Oncogene*, 2008. **27**(41): p. 5527-5541.
91. Niederst, M.J. and C.H. Benes, *EMT Twists the Road to PI3K*. *Cancer Discovery*, 2014. **4**(2): p. 149.
92. Xu, W., Z. Yang, and N. Lu, *A new role for the PI3K/Akt signaling pathway in the epithelial-mesenchymal transition*. *Cell adhesion & migration*, 2015. **9**(4): p. 317-324.
93. Qian, Y., et al., *PI3K induced actin filament remodeling through Akt and p70S6K1: implication of essential role in cell migration*. *Am J Physiol Cell Physiol*, 2004. **286**(1): p. C153-63.
94. Papa, A. and P.P. Pandolfi, *The PTEN–PI3K Axis in Cancer*. *Biomolecules*, 2019. **9**(4): p. 153.
95. Hollander, M.C., G.M. Blumenthal, and P.A. Dennis, *PTEN loss in the continuum of common cancers, rare syndromes and mouse models*. *Nat Rev Cancer*, 2011. **11**(4): p. 289-301.
96. Milella, M., et al., *PTEN: Multiple Functions in Human Malignant Tumors*. *Frontiers in oncology*, 2015. **5**: p. 24-24.
97. Shapiro, P., et al., *Mitogen-Activated Protein (MAP) Kinases and Receptors*, in *Encyclopedia of Endocrine Diseases*, L. Martini, Editor. 2004, Elsevier: New York. p. 252-257.
98. McCain, J., *The MAPK (ERK) Pathway: Investigational Combinations for the Treatment Of BRAF-Mutated Metastatic Melanoma*. *P & T : a peer-reviewed journal for formulary management*, 2013. **38**(2): p. 96-108.
99. Schlaepfer, D.D., et al., *Integrin-mediated signal transduction linked to Ras pathway by GRB2 binding to focal adhesion kinase*. *Nature*, 1994. **372**(6508): p. 786-91.
100. Coles, L.C. and P.E. Shaw, *PAK1 primes MEK1 for phosphorylation by Raf-1 kinase during cross-cascade activation of the ERK pathway*. *Oncogene*, 2002. **21**(14): p. 2236-44.
101. Avruch, J., et al., *Ras activation of the Raf kinase: tyrosine kinase recruitment of the MAP kinase cascade*. *Recent Prog Horm Res*, 2001. **56**: p. 127-55.
102. Maik-Rachline, G., A. Hacoheh-Lev-Ran, and R. Seger, *Nuclear ERK: Mechanism of Translocation, Substrates, and Role in Cancer*. *Int J Mol Sci*, 2019. **20**(5).
103. Sanchez-Vega, F., et al., *Oncogenic Signaling Pathways in The Cancer Genome Atlas*. *Cell*, 2018. **173**(2): p. 321-337.e10.
104. Jokinen, E. and J.P. Koivunen, *MEK and PI3K inhibition in solid tumors: rationale and evidence to date*. *Therapeutic Advances in Medical Oncology*, 2015. **7**(3): p. 170-180.
105. Mendoza, M.C., E.E. Er, and J. Blenis, *The Ras-ERK and PI3K-mTOR pathways: cross-talk and compensation*. *Trends in biochemical sciences*, 2011. **36**(6): p. 320-328.
106. Lee, E.R., et al., *Interplay between PI3K/Akt and MAPK signaling pathways in DNA-damaging drug-induced apoptosis*. *Biochim Biophys Acta*, 2006. **1763**(9): p. 958-68.
107. Choi, C. and D.M. Helfman, *The Ras-ERK pathway modulates cytoskeleton organization, cell motility and lung metastasis signature genes in MDA-MB-231 LM2*. *Oncogene*, 2014. **33**(28): p. 3668-3676.
108. Toyjanova, J., et al., *High Resolution, Large Deformation 3D Traction Force Microscopy*. *PLOS ONE*, 2014. **9**(4): p. e90976.

109. Schwarz, U.S. and J.R.D. Soiné, *Traction force microscopy on soft elastic substrates: A guide to recent computational advances*. Biochimica et Biophysica Acta (BBA) - Molecular Cell Research, 2015. **1853**(11, Part B): p. 3095-3104.
110. le Digabel, J., et al., *Magnetic micropillars as a tool to govern substrate deformations*. Lab Chip, 2011. **11**(15): p. 2630-6.
111. Humphris, A.D.L. and M.J. Miles, *Chapter 16 - Developments in Dynamic Force Microscopy and Spectroscopy*, in *Methods in Cell Biology*, B.P. Jena and J.K. Heinrich Hörber, Editors. 2002, Academic Press. p. 337-355.
112. Rajagopalan, J. and M.T. Saif, *MEMS Sensors and Microsystems for Cell Mechanobiology*. J Micromech Microeng, 2011. **21**(5): p. 54002-54012.
113. Roca-Cusachs, P., V. Conte, and X. Trepast, *Quantifying forces in cell biology*. Nature Cell Biology, 2017. **19**(7): p. 742-751.
114. Yang, Z., et al., *Determining substrate displacement and cell traction fields—a new approach*. Journal of Theoretical Biology, 2006. **242**(3): p. 607-616.
115. Hur, S.S., et al., *Live Cells Exert 3-Dimensional Traction Forces on Their Substrata*. Cellular and molecular bioengineering, 2009. **2**(3): p. 425-436.
116. Kulkarni, A.H., et al., *Traction cytometry: regularization in the Fourier approach and comparisons with finite element method*. Soft Matter, 2018. **14**(23): p. 4687-4695.
117. Mulligan, J.A., et al., *Traction Force Microscopy for Noninvasive Imaging of Cell Forces*. Advances in experimental medicine and biology, 2018. **1092**: p. 319-349.
118. Ambrosi, D., *Cellular traction as an inverse problem*. SIAM Journal on Applied Mathematics, 2006. **66**(6): p. 2049-2060.
119. Butler, J.P., et al., *Traction fields, moments, and strain energy that cells exert on their surroundings*. American Journal of Physiology - Cell Physiology, 2002. **282**(3): p. C595.
120. Long, R., et al., *Effects of gel thickness on microscopic indentation measurements of gel modulus*. Biophysical journal, 2011. **101**(3): p. 643-650.
121. Sabass, B., et al., *High Resolution Traction Force Microscopy Based on Experimental and Computational Advances*. Biophysical Journal. **94**(1): p. 207-220.
122. Huang, J., et al., *Determination of cellular tractions on elastic substrate based on an integral Boussinesq solution*. J Biomech Eng, 2009. **131**(6): p. 061009.
123. Dembo, M. and Y.L. Wang, *Stresses at the cell-to-substrate interface during locomotion of fibroblasts*. Biophysical Journal, 1999. **76**(4): p. 2307-2316.
124. Dembo, M., et al., *Imaging the traction stresses exerted by locomoting cells with the elastic substratum method*. Biophysical Journal, 1996. **70**(4): p. 2008-2022.
125. Stricker, J., et al., *Optimization of traction force microscopy for micron-sized focal adhesions*. Journal of Physics: Condensed Matter, 2010. **22**(19): p. 194104.
126. Plotnikov, S.V., et al., *High-resolution traction force microscopy*. Methods in cell biology, 2014. **123**: p. 367-394.
127. Scharnowski, S. and C.J. Kähler, *Particle image velocimetry - Classical operating rules from today's perspective*. Optics and Lasers in Engineering, 2020: p. 106185.
128. Mori, N. and K.-A. Chang, *Introduction to MPIV*.
129. Manning, G.S., *The Persistence Length of DNA Is Reached from the Persistence Length of Its Null Isomer through an Internal Electrostatic Stretching Force*. Biophysical Journal, 2006. **91**(10): p. 3607-3616.
130. Aratyn-Schaus, Y., et al., *Preparation of Complaint Matrices for Quantifying Cellular Contraction*. Journal of Visualized Experiments : JoVE, 2010(46): p. 2173.
131. Schindelin, J., et al., *Fiji: an open-source platform for biological-image analysis*. Nat Meth, 2012. **9**(7): p. 676-682.

132. Schindelin, J., et al., *The ImageJ ecosystem: An open platform for biomedical image analysis*. Molecular Reproduction and Development, 2015. **82**(7-8): p. 518-529.
133. Paluch, E.K., et al., *Mechanotransduction: use the force(s)*. BMC biology, 2015. **13**: p. 47-47.
134. Ananthakrishnan, R. and A. Ehrlicher, *The Forces Behind Cell Movement*. International Journal of Biological Sciences, 2007. **3**(5): p. 303-317.
135. Fournier, M.F., et al., *Force transmission in migrating cells*. The Journal of Cell Biology, 2010. **188**(2): p. 287-297.
136. Gorelik, R. and A. Gautreau, *Quantitative and unbiased analysis of directional persistence in cell migration*. Nature Protocols, 2014. **9**(8): p. 1931-1943.
137. Kalluri, R. and R.A. Weinberg, *The basics of epithelial-mesenchymal transition*. The Journal of clinical investigation, 2009. **119**(6): p. 1420-1428.
138. Ko, S.H., et al., *Expression of the intermediate filament vimentin in proliferating duct cells as a marker of pancreatic precursor cells*. Pancreas, 2004. **28**(2): p. 121-8.
139. de Souza, P.C. and S.G. Katz, *Coexpression of cytokeratin and vimentin in mice trophoblastic giant cells*. Tissue and Cell, 2001. **33**(1): p. 40-45.
140. Cochard, P. and D. Paulin, *Initial expression of neurofilaments and vimentin in the central and peripheral nervous system of the mouse embryo in vivo*. The Journal of Neuroscience, 1984. **4**(8): p. 2080-2094.
141. Mahrle, G., et al., *Intermediate filaments of the vimentin and prekeratin type in human epidermis*. J Invest Dermatol, 1983. **81**(1): p. 46-8.
142. Eckes, B., et al., *Impaired wound healing in embryonic and adult mice lacking vimentin*. Journal of Cell Science, 2000. **113**(13): p. 2455.
143. Eckes, B., et al., *Impaired mechanical stability, migration and contractile capacity in vimentin-deficient fibroblasts*. Journal of Cell Science, 1998. **111**(13): p. 1897.
144. Jiu, Y., et al., *Vimentin intermediate filaments control actin stress fiber assembly through GEF-H1 and RhoA*. Journal of cell science, 2017. **130**(5): p. 892-902.
145. El-Brolosy, M.A. and D.Y.R. Stainier, *Genetic compensation: A phenomenon in search of mechanisms*. PLoS genetics, 2017. **13**(7): p. e1006780-e1006780.
146. Linthicum, W., et al., *Effects of PTEN Loss and Activated KRAS Overexpression on Mechanical Properties of Breast Epithelial Cells*. International Journal of Molecular Sciences, 2018. **19**(6): p. 1613.
147. Thomas, G., et al., *Measuring the mechanical properties of living cells using atomic force microscopy*. Journal of visualized experiments : JoVE, 2013(76): p. 50497.
148. Beningo, K.A., et al., *Traction forces of fibroblasts are regulated by the Rho-dependent kinase but not by the myosin light chain kinase*. Archives of biochemistry and biophysics, 2006. **456**(2): p. 224-231.
149. McCann, C.P., et al., *Cell speed, persistence and information transmission during signal relay and collective migration*. Journal of Cell Science, 2010. **123**(10): p. 1724.
150. Kolega J, J.L., Taylor DL, *The role of solation-contraction coupling in regulating stress fiber dynamics in nonmuscle cells*. The Journal of Cell Biology, 1991. **114**(5): p. 993-1003.
151. Geiger, B. and A. Bershadsky, *Assembly and mechanosensory function of focal contacts*. Current Opinion in Cell Biology, 2001. **13**(5): p. 584-592.
152. Yeung, T., et al., *Effects of substrate stiffness on cell morphology, cytoskeletal structure, and adhesion*. Cell Motility and the Cytoskeleton, 2005. **60**(1): p. 24-34.
153. Geiger, B., et al., *Transmembrane crosstalk between the extracellular matrix and the cytoskeleton*. Nat Rev Mol Cell Biol, 2001. **2**(11): p. 793-805.
154. Geiger, B., J.P. Spatz, and A.D. Bershadsky, *Environmental sensing through focal adhesions*. Nature Reviews Molecular Cell Biology, 2009. **10**: p. 21.

155. Wozniak, M.A. and C.S. Chen, *Mechanotransduction in development: a growing role for contractility*. Nature Reviews Molecular Cell Biology, 2009. **10**: p. 34.
156. Wiche, G., *Role of plectin in cytoskeleton organization and dynamics*. Journal of Cell Science, 1998. **111**(17): p. 2477-2486.
157. Seifert, G.J., D. Lawson, and G. Wiche, *Immunolocalization of the intermediate filament-associated protein plectin at focal contacts and actin stress fibers*. European journal of cell biology, 1992. **59**(1): p. 138-147.
158. Na, S., et al., *Plectin contributes to mechanical properties of living cells*. American Journal of Physiology - Cell Physiology, 2009. **296**(4): p. C868-C877.
159. Guo, M., et al., *The Role of Vimentin Intermediate Filaments in Cortical and Cytoplasmic Mechanics*. Biophysical Journal, 2013. **105**(7): p. 1562-1568.
160. Maniotis, A.J., C.S. Chen, and D.E. Ingber, *Demonstration of mechanical connections between integrins, cytoskeletal filaments, and nucleoplasm that stabilize nuclear structure*. Proceedings of the National Academy of Sciences, 1997. **94**(3): p. 849-854.
161. Costigliola, N., et al., *Vimentin fibers orient traction stress*. 2017.
162. Wang, N., J.D. Tytell, and D.E. Ingber, *Mechanotransduction at a distance: mechanically coupling the extracellular matrix with the nucleus*. Nature Reviews Molecular Cell Biology, 2009. **10**: p. 75.
163. Hu, S., et al., *Mechanical anisotropy of adherent cells probed by a three-dimensional magnetic twisting device*. American Journal of Physiology-Cell Physiology, 2004. **287**(5): p. C1184-C1191.
164. Gjorevski, N., et al., *Dynamic tensile forces drive collective cell migration through three-dimensional extracellular matrices*. Scientific Reports, 2015. **5**(1): p. 11458.
165. Sunyer, R., et al., *Collective cell durotaxis emerges from long-range intercellular force transmission*. Science, 2016. **353**(6304): p. 1157.
166. Gan, Z., et al., *Vimentin Intermediate Filaments Template Microtubule Networks to Enhance Persistence in Cell Polarity and Directed Migration*. Cell Systems, 2016. **3**(3): p. 252-263.e8.
167. Chan, C.E. and D.J. Odde, *Traction Dynamics of Filopodia on Compliant Substrates*. Science, 2008. **322**(5908): p. 1687-1691.
168. Case, L.B. and C.M. Waterman, *Integration of actin dynamics and cell adhesion by a three-dimensional, mechanosensitive molecular clutch*. Nature Cell Biology, 2015. **17**: p. 955.
169. Leube, R.E., M. Moch, and R. Windoffer, *Intermediate filaments and the regulation of focal adhesion*. Current Opinion in Cell Biology, 2015. **32**: p. 13-20.
170. Dave, J.M. and K.J. Bayless, *Vimentin as an Integral Regulator of Cell Adhesion and Endothelial Sprouting*. 2014. **21**(4): p. 333-344.
171. Kim, H., et al., *Filamin A is required for vimentin-mediated cell adhesion and spreading*. 2010. **298**(2): p. C221-C236.
172. Kim, H. and C.A. McCulloch, *Filamin A mediates interactions between cytoskeletal proteins that control cell adhesion*. FEBS Letters, 2011. **585**(1): p. 18-22.
173. Burgstaller, G., et al., *Keeping the Vimentin Network under Control: Cell–Matrix Adhesion–associated Plectin 1f Affects Cell Shape and Polarity of Fibroblasts*. Molecular Biology of the Cell, 2010. **21**(19): p. 3362-3375.
174. Das, T., T.K. Maiti, and S. Chakraborty, *Traction force microscopy on-chip: shear deformation of fibroblast cells*. Lab on a Chip, 2008. **8**(8): p. 1308-1318.
175. Das, T., T.K. Maiti, and S. Chakraborty, *Augmented stress-responsive characteristics of cell lines in narrow confinements*. Integrative Biology, 2011. **3**(6): p. 684-695.
176. Zielinski, R., et al., *Finite Element Analysis of Traction Force Microscopy: Influence of Cell Mechanics, Adhesion, and Morphology*. Journal of Biomechanical Engineering, 2013. **135**(7): p. 071009-071009-9.

177. Jean, C., et al., *Influence of stress on extracellular matrix and integrin biology*. *Oncogene*, 2011. **30**(24): p. 2697-2706.
178. Aratyn-Schaus, Y. and M.L. Gardel, *Transient frictional slip between integrin and the ECM in focal adhesions under myosin-II tension*. *Current biology : CB*, 2010. **20**(13): p. 1145-1153.
179. Shemesh, T., A.D. Bershadsky, and M.M. Kozlov, *Physical model for self-organization of actin cytoskeleton and adhesion complexes at the cell front*. *Biophys J*, 2012. **102**(8): p. 1746-56.
180. Gardel, M.L., et al., *Traction stress in focal adhesions correlates biphasically with actin retrograde flow speed*. *The Journal of Cell Biology*, 2008. **183**(6): p. 999-1005.
181. Guo, Y.R. and R. MacKinnon, *Structure-based membrane dome mechanism for Piezo mechanosensitivity*. *Elife*, 2017. **6**.
182. Macosko, C.W., *Rheology : principles, measurements, and applications*. 1994, New York, NY: VCH.
183. Gawlitta, W., M. Osborn, and K. Weber, *Coiling of intermediate filaments induced by microinjection of a vimentin-specific antibody does not interfere with locomotion and mitosis*. *European journal of cell biology*, 1981. **26**(1): p. 83-90.
184. Hedberg, K.K. and L.B. Chen, *Absence of intermediate filaments in a human adrenal cortex carcinoma-derived cell line*. *Experimental Cell Research*, 1986. **163**(2): p. 509-517.
185. Holwell, T.A., S.C. Schweitzer, and R.M. Evans, *Tetracycline regulated expression of vimentin in fibroblasts derived from vimentin null mice*. 1997. **110**(16): p. 1947-1956.
186. Colucci-Guyon, E., et al., *Mice lacking vimentin develop and reproduce without an obvious phenotype*. *Cell*, 1994. **79**(4): p. 679-694.
187. Saini, K.S., et al., *Targeting the PI3K/AKT/mTOR and Raf/MEK/ERK pathways in the treatment of breast cancer*. *Cancer Treatment Reviews*, 2013. **39**(8): p. 935-946.
188. Adeyinka, A., et al., *Activated mitogen-activated protein kinase expression during human breast tumorigenesis and breast cancer progression*. *Clin Cancer Res*, 2002. **8**(6): p. 1747-53.
189. Sivaraman, V.S., et al., *Hyperexpression of mitogen-activated protein kinase in human breast cancer*. *The Journal of clinical investigation*, 1997. **99**(7): p. 1478-1483.
190. Thompson, K.N., et al., *The combinatorial activation of the PI3K and Ras/MAPK pathways is sufficient for aggressive tumor formation, while individual pathway activation supports cell persistence*. *Oncotarget*, 2015. **6**(34): p. 35231-35246.
191. Aguirre-Ghiso, J.A., *The problem of cancer dormancy: understanding the basic mechanisms and identifying therapeutic opportunities*. *Cell Cycle*, 2006. **5**(16): p. 1740-3.
192. Duman, B.B., et al., *Evaluation of PTEN, PI3K, MTOR, and KRAS expression and their clinical and prognostic relevance to differentiated thyroid carcinoma*. *Contemporary oncology (Poznan, Poland)*, 2014. **18**(4): p. 234-240.
193. Vitolo, M.I., et al., *Deletion of PTEN Promotes Tumorigenic Signaling, Resistance to Anoikis, and Altered Response to Chemotherapeutic Agents in Human Mammary Epithelial Cells*. *Cancer Research*, 2009. **69**(21): p. 8275.
194. Gaetani, R., et al., *When Stiffness Matters: Mechanosensing in Heart Development and Disease*. *Frontiers in Cell and Developmental Biology*, 2020. **8**(334).
195. Chin, L., et al., *Mechanotransduction in cancer*. *Current opinion in chemical engineering*, 2016. **11**: p. 77-84.
196. Lin, H.-H., et al., *Mechanical phenotype of cancer cells: cell softening and loss of stiffness sensing*. *Oncotarget*, 2015. **6**(25): p. 20946-20958.
197. Lim, M.A., et al., *Roles of PDK-1 and PKN in regulating cell migration and cortical actin formation of PTEN-knockout cells*. *Oncogene*, 2004. **23**(58): p. 9348-9358.
198. Malek, M., et al., *PTEN Regulates PI(3,4)P2 Signaling Downstream of Class I PI3K*. *Molecular Cell*, 2017. **68**(3): p. 566-580.e10.

199. dos Remedios, C.G. and N.J. Nosworthy, *The Role of PIP2 in Actin, Actin-Binding Proteins and Disease*, in *Actin-Binding Proteins and Disease*, C.G. dos Remedios and D. Chhabra, Editors. 2008, Springer New York: New York, NY. p. 290-297.
200. Zhou, J., et al., *Mechanism of Focal Adhesion Kinase Mechanosensing*. PLOS Computational Biology, 2015. **11**(11): p. e1004593.
201. Cox, T.R. and J.T. Erler, *Remodeling and homeostasis of the extracellular matrix: implications for fibrotic diseases and cancer*. Disease models & mechanisms, 2011. **4**(2): p. 165-178.
202. Butcher, D.T., T. Alliston, and V.M. Weaver, *A tense situation: forcing tumour progression*. Nature reviews. Cancer, 2009. **9**(2): p. 108-122.
203. Koboldt, D.C., et al., *Comprehensive molecular portraits of human breast tumours*. Nature, 2012. **490**(7418): p. 61-70.
204. Davis, E.J., et al., *Risk of second primary tumors in men diagnosed with prostate cancer: a population-based cohort study*. Cancer, 2014. **120**(17): p. 2735-41.
205. Mirzoeva, O.K., et al., *Basal Subtype and MAPK/ERK Kinase (MEK)-Phosphoinositide 3-Kinase Feedback Signaling Determine Susceptibility of Breast Cancer Cells to MEK Inhibition*. Cancer Research, 2009. **69**(2): p. 565.
206. Yu, J., J. Drisko, and Q. Chen, *Inhibition of pancreatic cancer and potentiation of gemcitabine effects by the extract of Pao Pereira*. Oncol Rep, 2013. **30**(1): p. 149-56.
207. Chan, P.M., L. Lim, and E. Manser, *PAK is regulated by PI3K, PIX, CDC42, and PP2Calpha and mediates focal adhesion turnover in the hyperosmotic stress-induced p38 pathway*. J Biol Chem, 2008. **283**(36): p. 24949-61.
208. Thillai, K., et al., *Deciphering the link between PI3K and PAK: An opportunity to target key pathways in pancreatic cancer?* Oncotarget, 2017. **8**(8): p. 14173-14191.
209. Delorme, V., et al., *Cofilin activity downstream of Pak1 regulates cell protrusion efficiency by organizing lamellipodium and lamella actin networks*. Developmental cell, 2007. **13**(5): p. 646-662.
210. Janmey, P.A. and U. Lindberg, *Cytoskeletal regulation: rich in lipids*. Nature Reviews Molecular Cell Biology, 2004. **5**(8): p. 658-666.
211. Vitolo, M.I., et al., *Loss of PTEN induces microtentacles through PI3K-independent activation of cofilin*. Oncogene, 2013. **32**(17): p. 2200-2210.
212. Jiang, P., et al., *An Actin-Binding Protein Girdin Regulates the Motility of Breast Cancer Cells*. Cancer Research, 2008. **68**(5): p. 1310.
213. Enomoto, A., et al., *Akt/PKB regulates actin organization and cell motility via Girdin/APE*. Dev Cell, 2005. **9**(3): p. 389-402.
214. Mattila, P.K. and P. Lappalainen, *Filopodia: molecular architecture and cellular functions*. Nature Reviews Molecular Cell Biology, 2008. **9**(6): p. 446-454.
215. Micucci, C., S. Orciari, and A. Catalano, *Hyperglycemia promotes K-Ras-induced lung tumorigenesis through BASCs amplification*. PLoS One, 2014. **9**(8): p. e105550.
216. Kerr, E.M., et al., *Mutant Kras copy number defines metabolic reprogramming and therapeutic susceptibilities*. Nature, 2016. **531**(7592): p. 110-3.
217. Sasaki, H., et al., *Overexpression of GLUT1 correlates with Kras mutations in lung carcinomas*. Mol Med Rep, 2012. **5**(3): p. 599-602.
218. Bryant, K.L., et al., *KRAS: feeding pancreatic cancer proliferation*. Trends Biochem Sci, 2014. **39**(2): p. 91-100.
219. Suetsugu, S., et al., *Differential Roles of WAVE1 and WAVE2 in Dorsal and Peripheral Ruffle Formation for Fibroblast Cell Migration*. Developmental Cell, 2003. **5**(4): p. 595-609.

220. Steinestel, K., et al., *Expression of Abelson interactor 1 (Abi1) correlates with inflammation, KRAS mutation and adenomatous change during colonic carcinogenesis*. PloS one, 2012. **7**(7): p. e40671-e40671.
221. Joseph, N., et al., *A conformational change within the WAVE2 complex regulates its degradation following cellular activation*. Scientific Reports, 2017. **7**(1): p. 44863.
222. Kress, T.R., T. Raabe, and S.M. Feller, *High Erk activity suppresses expression of the cell cycle inhibitor p27Kip1 in colorectal cancer cells*. Cell communication and signaling : CCS, 2010. **8**(1): p. 1-1.
223. Sharma, S.S. and W.J. Pledger, *The non-canonical functions of p27(Kip1) in normal and tumor biology*. Cell cycle (Georgetown, Tex.), 2016. **15**(9): p. 1189-1201.
224. Sun, J., et al., *Role for p27^{Kip1} in Vascular Smooth Muscle Cell Migration*. Circulation, 2001. **103**(24): p. 2967-2972.
225. Besson, A., et al., *p27Kip1 modulates cell migration through the regulation of RhoA activation*. Genes Dev, 2004. **18**(8): p. 862-76.
226. Gandalovičová, A., et al., *Migrastatics—Anti-metastatic and Anti-invasion Drugs: Promises and Challenges*. Trends in Cancer, 2017. **3**(6): p. 391-406.
227. Tashiro, E. and M. Imoto, *Screening and target identification of bioactive compounds that modulate cell migration and autophagy*. Bioorganic & Medicinal Chemistry, 2016. **24**(15): p. 3283-3290.
228. Gerber, D.E., et al., *Phase 2 study of the focal adhesion kinase inhibitor defactinib (VS-6063) in previously treated advanced KRAS mutant non-small cell lung cancer*. Lung Cancer, 2020. **139**: p. 60-67.
229. Román, M., et al., *KRAS oncogene in non-small cell lung cancer: clinical perspectives on the treatment of an old target*. Molecular Cancer, 2018. **17**(1): p. 33.
230. Kim, D.-H. and D. Wirtz, *Focal adhesion size uniquely predicts cell migration*. FASEB journal : official publication of the Federation of American Societies for Experimental Biology, 2013. **27**(4): p. 1351-1361.
231. Stroka, K.M. and H. Aranda-Espinoza, *Effects of Morphology vs. Cell-Cell Interactions on Endothelial Cell Stiffness*. Cellular and molecular bioengineering, 2011. **4**(1): p. 9-27.
232. Eddy, R.J., et al., *Tumor Cell Invadopodia: Invasive Protrusions that Orchestrate Metastasis*. Trends in cell biology, 2017. **27**(8): p. 595-607.
233. Wolfenson, H., et al., *Tropomyosin controls sarcomere-like contractions for rigidity sensing and suppressing growth on soft matrices*. Nat Cell Biol, 2016. **18**(1): p. 33-42.
234. Lo, C.M., et al., *Cell movement is guided by the rigidity of the substrate*. Biophysical Journal, 2000. **79**(1): p. 144-152.
235. Blair, D. and E. Dufresne, *The Matlab Particle Tracking Code Repository*. 2005.
236. Chandrasekhar, S., *Liquid Crystals*. 2 ed. 1992, Cambridge: Cambridge University Press.

Appendix

This appendix only consists of code snippets that are relevant to the algorithm for solving for traction force and related analysis. Most of the tedious tasks, such as cleaning up the output, saving data, opening figures, etc. are only shown once or not shown at all. For a complete version of the codes in this section including external libraries and packages, visit my GitHub at github.com/htmtri/MatlabTFM

For a brief demonstration of the process, visit github.com/htmtri/pythonTFM and try out the TFM_PIV notebook. This version, however, is written in python using Jupyter notebook kernel, so there are differences in the algorithm. Nevertheless, it is a good way to visualize the process since MATLAB does not have a fully functional electronic notebook at the time this thesis is submitted.

Appendix A. Traction Force Microscopy (MATLAB & ANSYS APDL)

A1. Image Preprocess (TFM_Prep)

According to the methodology, we need to process at least a set of 3 images: one image of the cell to trace cell boundary, one image of the beads when the gel is deformed by the cells and one image of the beads when the gels are not under load.

```

[filec pathname]=uigetfile('*.TIFF', 'Pick the Phase contrast image file of the cell');
disp(['Cell Phase contrast image is ',filec])
[filea pathname]=uigetfile('*.TIFF', 'Pick the Fluorescent image of the beads before Trypsin')
disp(['Bead image before Trypsin is ',filea])
[fileb pathname]=uigetfile('*.TIFF', 'Pick the Fluorescent image of the beads after Trypsin')
disp(['Bead image after Trypsin is ',fileb])
pathname=pwd;
pathname=[pathname,filesep];

%Read images
c=imread([pathname,filec]);
a_org=imread([pathname,filea]);
b_org=imread([pathname,fileb]);

```

The image of the cell is taken in phase contrast mode and is not subjected to any image processing. The beads images, however, could use some image processing techniques to reduce the noise. Here, we use a slightly modified version of the bandpass filter provided by Daniel Blair and Eric Dufresne in their implementation of particle tracking [235]. This filter suppresses pixel noise and long-wavelength image variations while retaining information of a characteristic size. First, the program produces a low-pass image by convolving the original with a gaussian (which depends on the noise level that is set to 0 i.e. assuming high SNR ratio from beads image taken with the microscope). Next, a second low-pass image is produced by convolving the original with a boxcar function (which depends on the size of the object, in this case, we use the bead's diameter in pixel). By subtracting the boxcar version from the gaussian version, we use the boxcar version to perform a high-pass. (Figure S1A,B)

```

%bpassTF(im,noise[0/1],fsize [6-9 for 0.1um beads],threshold)
a=bpassTF(a_org,0,10,0.05*mode(a_org(:)));
b=bpassTF(b_org,0,10,0.05*mode(b_org(:)));

```

Now, we need to crop the ROI of all 3 images: the region that covered the cell of interest. There is a small drift in the images captured before and after due to physical interaction with the sample (pipetting, open/close environment chamber, ...), so we need to crop another ROI for de-drift: the region that has no cell and does not have any cells in close proximity. De-drifting was done by applying MATLAB cross-correlation function to compare before and after trypsinization beads images. (Figure S1C,D)

```

get user input to select a rectangular region enclosing the cell
figure,imshow(c,[])
title('Please select a rectangle region enclosing the cell');
disp('Please select a rectangle region enclosing the cell');
rect=round(getrect);
rect(3)=(round(rect(3)/32)+1)*32-1;
rect(4)=(round(rect(4)/32)+1)*32-1;
loading=imcrop(a,rect);
cellimg=imcrop(c,rect);

figure,imshow(c,[])
title('Please select a rectangle region far away from any cell');
disp('Please select a rectangle region far away from any cell');
recs=round(getrect);
recs(3)=(round(recs(3)/32)+1)*32-1;
recs(4)=(round(recs(4)/32)+1)*32-1;
[xd yd]=im_shift(a,b,recs);
%If enough to cut
if rect(2)+yd+rect(4)<size(b,1)
    nulfig=imcrop(b,rect+[xd yd 0 0]);

%cut image
csimg(:,:,1)=double(loading)/max(double(loading(:)));
csimg(:,:,2)=double(nulfig)/max(double(nulfig(:)));
csimg(:,:,3)=zeros(size(nulfig));
close all;

```

Finally, we draw cell boundaries to extract cell area, aspect ratio and input gel conditions with ANSYS version.

```

% Draw cell edge
figure, imshow(celling,[])
title('Please trace cell/colony outline');
disp('Please trace cell/colony outline in the figure');
[bwc,xc,yc]=roipoly;
reg=bwlabel(bwc);
[s,l]=bwboundaries(bwc);
g=regionprops(l, 'PixelList', 'Area', 'MajorAxisLength', 'MinorAxisLength');
Cell_Area=g.Area;
AspectRatio=g.MajorAxisLength./g.MinorAxisLength;
cellx=s{1}(:,2);
celly=s{1}(:,1);
cellTrace = [cellx celly];
figure()
imshow(csimg,[])
hold on
plot(cellTrace(:,1),cellTrace(:,2), 'r.')
hold off

%Scale factor, please modify it accordingly
scaleb=input('Scale bar (um/pixel): ');
if isempty(scaleb)
% User input Gel stiffness
egel=input('Gel Stiffness (Pa): '),
% User input ANSYS version
ver=input('ANSYS version: '),
%gel dimensions as the image size scaled for ansys. Thickness is set to be 64um;
gel.height=100*1e-6; %400.0*scale1;
gel.length=double(size(celling,2))*scale1;
gel.width=double(size(celling,1))*scale1

```

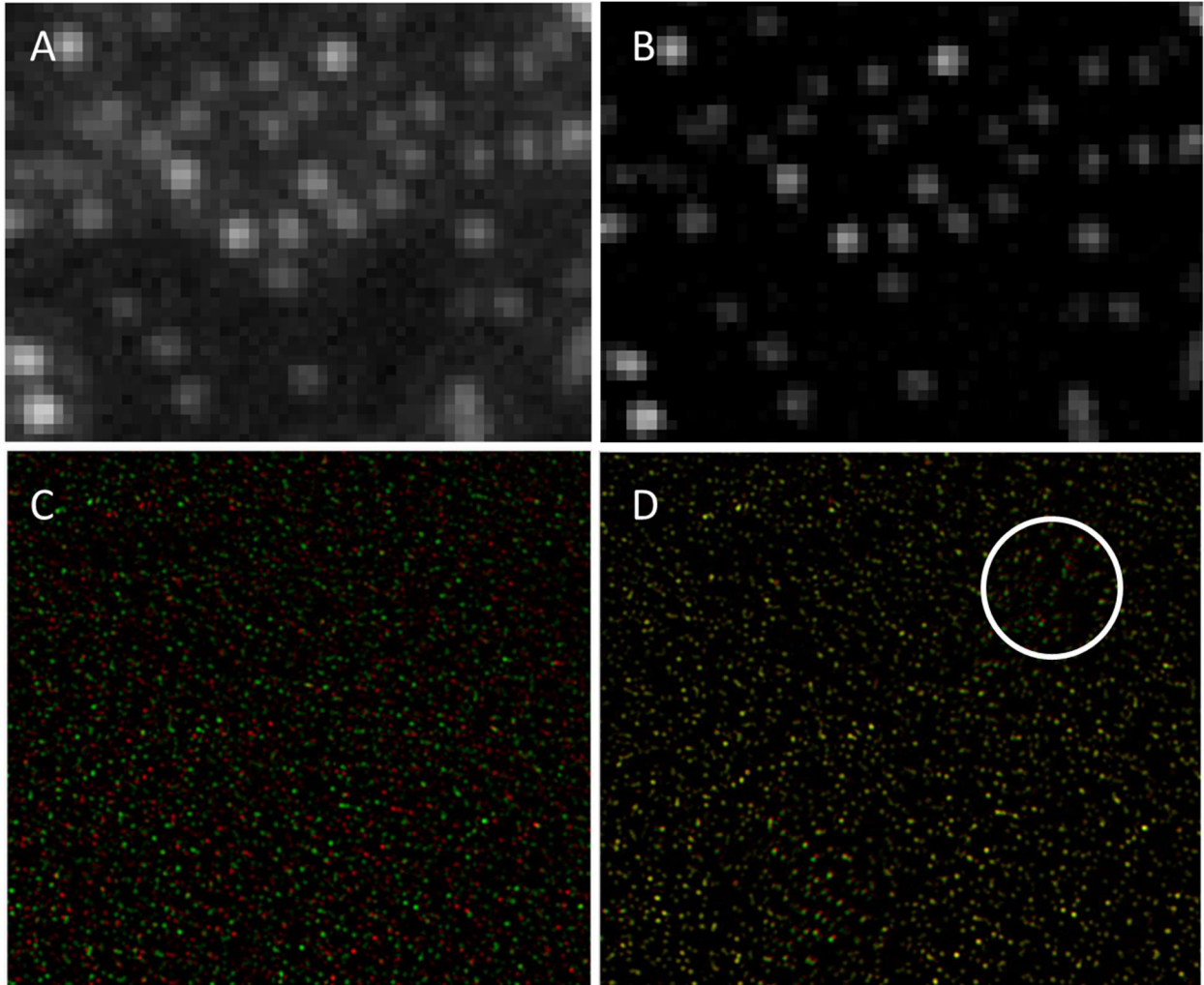


Figure S1. Demonstration of bpass filter: (A) bead image before filter, (B) bead image after filter. Demonstration of imshift correction: overlay bead images before (green) and after (red) trypsin (C) before shift corrected, (D) after shift corrected. White circle highlights the real displacement of beads cause by cell traction.

A2. PIV (TFM_disp)

With proper cropped and de-drifted beads images, we can now perform PIV to extract beads deformation caused by the cell. The explanation of the method is provided in the main section of the thesis above.

```
%PIV code to get the bead displ
[xi,yi,iu,iv,D]=mpiv(sdata.nulfig,sdata.loadimg,windows_size,windows_size,0.5,0.5,search_range,search_range,1,'mqd',1,0);
%input: img1,img2,xsize,ysize,xoverlap,yoverlap,xmax,ymax,dt,type,recur,plot
[iu_f,iv_f,iu_s, iv_s] = mpiv_filter(iu,iv, 2, 3.0, 3, 0);
%input: iu,iv,filter 2= median, std_stray, interpolation, plot
[iu_i, iv_i] = mpiv_smooth(iu_s, iv_s, 0);
```

The rest is mostly cleanup task: dealing with NaN (Not-a-Number) values from PIV analysis, denoise, bogus displacement due to empty/noisy regions of abnormal beads displacement that is out of analysis range. Then, the location of the nodes and the displacement at the nodes is saved for the next step.

```

%check and replace NaN field in iu_i and iv_v with 0
iu_i(isnan(iu_i))=0;
iv_i(isnan(iv_i))=0;

%remove drift. the drift will be taken as the x and y displacements at
%nodes outside the cell.
iu_m=iu_i;
iv_m=iv_i;

figure,
imshow(sdata.cellimg, [])
title('Please trace the loose outline around cell');
disp('Please trace the loose outline around in the figure');
[bw,xc,yc]=roipoly;
[s,l]=bwboundaries(bw);
cellxl=s{1}(:,2);
cellyl=s{1}(:,1);

bws=imresize(bw,size(iu'));
bws=bws';
ids=find(bws(:)==0);
driftx=mean(iu_m(ids));
drifty=mean(iv_m(ids));

dispm=sqrt(iu_m(ids).^2+iv_m(ids).^2);
dnoise=nanstd(dispm);

iu_m=iu_i-driftx;
iv_m=iv_i-drifty;

%remove large displacements in area without beads
%Selecte polygonal regions where displacement are large but no beads
removp=input('Do you want to remove bogus displacements? \n [1 (yes), 0 (No)]: ');
while removp==1
    [xdata,ydata,bw,xc,yc]=roipoly;
    [in, on] = inpolygon(xgrid,ygrid,xc,yc);
    iu_m(in)=0;
    iv_m(in)=0;
    figure,
    imshow(cimg, []);
    hold on,
    quiver(xm',ym',iu_i,iv_i,'c');
    quiver(xgrid,ygrid,iu_m,iv_m,'r');
    plot(sdata.cellTrace(:,1),sdata.cellTrace(:,2),'r.')
    hold off
    title('Left click to continue removing, Right click to stop');
    [x,y,removp]=ginput(1);
end

%real disp defined as having snr larger than snr outside cell
dispmags = sqrt(iu_m.^2+iv_m.^2);
realdisp=find(dispmags>0.5*dnoise);
% realdisp=find(dispmags./dnoise>(mean(dispm)./dnoise));
if length(realdisp) < 0.1*length(find(in==1))
    warning('Number of real displacement nodes is too low')
end

```

A3. Force Reconstruction (TFM_solve)

First, we need to construct ANSYS model.

```
%init
sdata=load([samp, '.mat']);
xgrid=sdata.xgrid;
ygrid=sdata.ygrid;
xdisp=sdata.xdisp;
ydisp=sdata.ydisp;
scale=sdata.scale;
version=sdata.version;
cellTrace=sdata.cellTrace;
outcelldisp=sdata.outcelldisp;
dispnoise=sdata.dispnoise;
cimg=sdata.cimg;
gel=sdata.gel;

%define meshsize for ansys
isize=double(max([xgrid(2)-xgrid(1) ygrid(2)-ygrid(1)]));
meshsize=isize*scale;

%write ansys modeling file to generate the nodes
modelfile=writeAnsysModel(samp,gel,meshsize)

%Run Ansys to generate mesh and export the mesh number and x-y coordinates
cmds=['"',homedrive,':\Program Files\ANSYS Inc\v',num2str(version),'\ansys\bin\winx64\ANSYS',num2str(version),'.exe" -b -i ', ...
    modelfile, ' -o ', samp, 'ModelLog.txt'];
[stat results]=system(cmds);

% If ansys run with error, Terminate program and you need to find if there
% is anything wrong.
if stat
    outp=0;
    return;
end
```

A typical ANSYS model text file looks like this:

```

finish
/clear
/TITLE,cell1
/PREP7
/graph,full
block,0,0.00018547,0,0.00010304,0,6.44e-005 !dimensions of model
ET,1,SOLID185 !8 nodes 3 degrees of freedom (translational x,y,z)
MPTEMP,,,,,,,,
MPTEMP,1,0 !default
MPDATA,EX,1,,7500 !young modulus
MPDATA,PRXY,1,,0.4 !poisson ratio
ESIZE,2.576e-006 !meshsize
vmesh,1 !volume 1 mesh
  nsel,s,loc,z,0,0 !select a new set of nodes from z = 0 to z = 0
/OUTPUT,NLIST_cell1,txt
nlist
/OUTPUT
FINISH

```

Next, we need to specify what needs to be solved from the model (solver).

```

    reading nlist and cell data - finding positions and displacements
m=readnode(['NLIST_',samp, '.txt'],2,10,50,7);
nlist=m.nodes;
xn=nlist(:,2)+xgrid(1)*scale; yn=nlist(:,3)+ygrid(1)*scale;
dxn=interp2(xgrid'*scale,ygrid'*scale,xdisp'*scale,xn,yn);
dyn=interp2(xgrid'*scale,ygrid'*scale,ydisp'*scale,xn,yn);
dxn(isnan(dxn))=0;
dyn(isnan(dyn))=0;

%find the nodal displacement 1 standard deviations larger than noise level
dispmags=sqrt(dxn.^2+dyn.^2);
realids=find(dispmags>0.5*dispnoise*scale);
% realids=find(dispmags>(mean(outcelldisp)+0.25*dispnoise)*scale);
num_node=length(realids);

%find nodes inside cell
xcell=(cellTrace(:,1))*scale;
ycell=(cellTrace(:,2))*scale;
Incell=inpolygon(xn,yn,xcell,ycell);
index_cell=find(Incell==1);
num_innode=size(index_cell,1);

%find nodes with real displacement and inside cell
realindex=intersect(index_cell,realids);
num_realindex=size(realindex,1);

%real displacement condition check
if num_realindex < 0.1*num_innode
    warning('Number of real displacement nodes is too low')
    writeerror(samp,['Number of real displacement nodes is too low. num_innode = ', ...
        num2str(num_innode), ' num_realnode = ',num2str(num_realindex)])
end

% Making displacement table for AYSYS (only nodes within cell are
% assigned displacements)
B=[[1:length(realindex)]' (nlist(realindex,1)) xn(realindex) yn(realindex) dxn(realindex) dyn(r
ealindex)];
B(2:length(realindex)+1,:)=B(1:length(realindex),:);
B(1,:)=[0:5];
format shortG;
dlmwrite([samp, 'load.txt'],B, '\t');
% Making ansys input text file for ansys - to apply the load on top
solvfiln=WriteAnsysSolver(samp,gel,meshsize,num_realindex)

ansysbatch=writeAnsysCommand(samp,homedrive,version,24);

```

A typical ANSYS solver looks like this:

```
finish
/clear
/TITLE,cell1
/PREP7
/graph,full
block,0,0.00018547,0,0.00010304,0,6.44e-005 !dimensions of model
ET,1,SOLID185 !8 nodes 3 degrees of freedom (translational x,y,z)
MPTEMP,,,,,,,,
MPTEMP,1,0 !default
MPDATA,EX,1,,7500 !young modulus
MPDATA,PRXY,1,,0.4 !Poisson ratio
ESIZE,2.576e-006 !meshsize
nset, all
vmesh,1
*dim,Txy,table,941,5,1 !nodal load table
*tread,Txy,'cell1load.txt' !read load
*do,i,1,941,1 !reconstruct load
d,Txy(i,1),ux,Txy(i,4)
d,Txy(i,1),uy,Txy(i,5)
*enddo
da,2,ux,0 !degree of freedom
da,2,uy,0
da,2,uz,0
FINISH
/SOLU
SOLVE
FINISH
/POST1
nset,s,loc,z,0,0
/OUTPUT, PRNSOL_cell1.txt
prnsol,s,comp !g solver mode
/OUTPUT
FINISH
```

Finally, we just need to instruct ANSYS via cmd to start solving for force.

A4. Plots (TFM_Plot)

First, we need to process the output from ANSYS. PRNSOL_S contains information about the nodal stress on the top layer (surface) of the gel. PRNLD contains information about nodal

loads (reaction force). PRNSOL_U contains information about nodal displacement. Ideally, this is exactly the same as PIV result. Practically, the displacements from ANSYS and mPIV only match inside the loose outline defined by TFM_disp, but this is sufficient for our purpose of obtaining cellular traction. From the output files, we can extract total traction force, maximum stress and average stress. In addition, net moment and strain energy (stored in the gel) can also be obtained. Afterward, we can make plots of cell image overlay with nodal displacements/nodal forces as well as cell outline with stress heatmap to visualize traction stress location (Figure 10D)

```

Area=sdata.meshsize*sdata.meshsize;
xnn = sdata.xnode; ynn = sdata.ynode;
xn=xnn/sdata.scale;yn=ynn/sdata.scale;

% Stress on On Layer 1 due to the load on top surface
ress1=readnode(['PRNSOL_',samp,'.txt'],2,17,37,7);
list_1=ress1.nodes;syz=-list_1(:,6);sxz=-list_1(:,7);
S1=sqrt((syz).^2+(sxz).^2);
SForce=Area*S1;
totSForce=sum(SForce);
Avgstress=mean(S1);
Maxstress=max(S1);

%read reaction force
forcedatan=readnode(['PRNLD_',samp,'.txt'],2,17,37,4);
Fxn=-forcedatan.nodes(:,2);
Fyn=-forcedatan.nodes(:,3);
RForce=sqrt((Fxn).^2+(Fyn).^2);
totForce=sum(RForce);
Sxn=Fxn./Area;
Syn=Fyn./Area;
R1=RForce./Area;
AvgRstress=mean(R1);
MaxRstress=max(R1);

%read displacement
displacement=readnode(['PRNSOL_U',samp,'.txt'],2,17,37,5);
Dxn=displacement.nodes(:,2);
Dyn=displacement.nodes(:,3);
D1=sqrt((sdata.dxn).^2+(sdata.dyn).^2);
D2=sqrt((Dxn).^2+(Dyn).^2);
Avgdisp=mean(D1);
Avgdispsol=mean(D2);

%StrainEnergyDensity
SE = sum(Area.*(sdata.dxn.*sxz + sdata.dyn.*syz))/2;
%Traction Moment
mtrs=[sum(xnn.*sxz) (sum(xnn.*syz)+sum(ynn.*sxz))/2;(sum(xnn.*syz)+sum(ynn.*sxz))/2 sum(ynn.*syz)]*
Area;
[D, W]=eig(mtrs);
NetMoment=trace(mtrs);

```

```

%plot displacement result
A = figure();
imshow(sdata.cimg, []);
hold on,
quiver(xn,yn,sdata.dxn,sdata.dyn,'c');
plot(sdata.cellTrace(:,1),sdata.cellTrace(:,2),'r','LineWidth',2);
if isfield(sdata,'numCells')
    for i=1:length(sdata.indCellArea)
        plot(sdata.indCellTrace{i}(:,1),sdata.indCellTrace{i}(:,2),'LineWidth',1.5)
    end
end
hold off

%plot force result
B = figure();
imshow(sdata.celling, []);
hold on,
quiver(xn,yn,Fxn,Fyn,'y')
plot(sdata.cellTrace(:,1),sdata.cellTrace(:,2),'r','LineWidth',2);
hold off

%plot stressmap result
mx=max(xn);
my=max(yn);
[xssm,yssm]=meshgrid(0:mx,0:my);
zmsh=griddata(xn,yn,S1,xssm,yssm);
C = figure();
imagesc(zmsh);colormap(jet);colorbar;
hold on,
plot(sdata.cellTrace(:,1),sdata.cellTrace(:,2),'w','LineWidth',2);
cbar=colorbar;
set(get(cbar,'ylabel'),'String','Stress [Pa]','fontsize', 16);
set(cbar,'fontsize', 16);
hold off

```

Appendix B. Traction Force Post Analysis (MATLAB)

B1. Order Parameter

To quantify short-ranged stress alignment ($\sim 3\mu\text{m}$) using the order parameter S commonly used in liquid crystal to describe the orientational order of a nematic liquid crystal [236]. In our case, the order parameter specifies the orientational order of local stress vectors in cells. First, we need to segment the cells into small squares consisting of at least 4 nodes (i.e. minimum size of 32×32 pixels).

```
xmin = min(cellTrace(:,1));
ymin = min(cellTrace(:,2));
xmax = max(cellTrace(:,1));
ymax = max(cellTrace(:,2));
biggrid = polyshape([xmin xmax xmax xmin],[ymin ymin ymax ymax]);

gridsize = 36;

index = 0;
% lgrid = cell((ceil((xmax-xmin)./gridsize).*(ceil((ymax-ymin)./gridsize))),1);

for x = xmin:gridsize:xmax
    for y = ymin:gridsize:ymax
        vertices = [[x,y]; [x+gridsize,y]; [x+gridsize,y+gridsize]; [x,y+gridsize]];
        cond = inpolygon(vertices(:,1),vertices(:,2),cellTrace(:,1),cellTrace(:,2));
        cond2 = inpolygon(cellTrace(:,1),cellTrace(:,2),vertices(:,1),vertices(:,2));
        if any(cond(:) > 0) || any(cond2(:) > 0 )
            sgrid = polyshape([x x+gridsize x+gridsize x],[y y y+gridsize y+gridsize]);
            index = index+1;
            lgrid{index} = sgrid;
        end
    end
end
```

Next, we need to traverse through every segment; for each segment, the local alignment is first calculated, then the angles between the local alignment and each force

vectors are obtained. Finally, each segment's order parameter is calculated as the mean of all angles in the segment. The cell's order parameter is defined as the mean of all segment's order parameter. (Figure S2)

```

% check for nodes in cell boundary
inTrace = inpolygon(xn,yn,cellTrace(:,1),cellTrace(:,2));
xfil = xn(inTrace);
yfil = yn(inTrace);
xstressf = xstress(inTrace);
ystressf = ystress(inTrace);

% go through all segments, check for nodes in segments and perform calculation
for k=1:index
    inrect = inpolygon(xfil,yfil,lgrid{k}.Vertices(:,1),lgrid{k}.Vertices(:,2));
    xpos = xfil(inrect);
    ypos = yfil(inrect);
    xstr = xstressf(inrect);
    ystr = ystressf(inrect);
    if ~(length(xstr) < 1 || length(ystr) < 1)
        xnew = mean(xstr);
        ynew = mean(ystr);
        theta = zeros(length(xstr),1);
        for i = 1:length(xstr)
            theta(i) = atan2d(xstr(i).*ynew-xnew.*ystr(i), ...
                xstr(i).*xnew+ystr(i).*ynew);
        end
        s(k) = mean((3.*cosd(theta).^2 - 1)./2);
    end
end
m.ordergrid = mean(s);
end

```

B2. Correlation length

Every node from the result of traction force analysis consists of position x , y and length u , v in Cartesian coordinate. To find the correlation length, which is defined as $\langle \cos \theta \rangle =$

$e^{-\frac{d}{P}}$, we need to find the cosine of the angle between two nodes and their respective distance.

First, we need to filter out nodes with zero-length vectors.

```
% screening
xCell = cellTrace(:,1);
yCell = cellTrace(:,2);

[inCell onCell]= inpolygon(xn,yn,xCell,yCell);
flooridx = abs(xstress)>1;
flooridy = abs(ystress)>1;

xstr=xstress(inCell&flooridx&flooridy);
ystr=ystress(inCell&flooridx&flooridy);
xnn=xn(inCell&flooridx&flooridy);
ynn=yn(inCell&flooridx&flooridy);
```

Next, we need to calculate the dot product and distance of every node with the rest of the nodes in the filtered list.

```
[dotp,distance] = deal(NaN(length(xstr)));

for i = 1:length(xstr)
    for j = 1:length(xstr)
        if j >= i
            dotp(i,j) = dot([xstr(i) ystr(i)]./norm([xstr(i) ystr(i)]), ...
                [xstr(j) ystr(j)]./norm([xstr(j) ystr(j)]));
            distance(i,j) = round(sqrt((xnn(i)-xnn(j)).^2 + (ynn(i)-ynn(j)).^2));
        end
    end
end
```

Now, we will organize the result in a table of distances between nodes and corresponding dot product between nodes. If a value of distance has several corresponding dot products, we will average them.

```

dist = unique(distance(:));
dist = dist(~isnan(dist));
[R,C] = arrayfun(@(n)find(distance==n),dist,'Uni',0);
pos = cellfun(@(r,c)[r(:),c(:)],R,C,'Uni',0);
lengthofpos=cellfun(@(x) numel(x),pos);

moa = NaN(length(pos),max(lengthofpos)./2);

for ii = 1:length(pos)
    for jj = 1:size(pos{ii},1)
        moa(ii,jj) = abs(dotp(pos{ii}(jj,1),pos{ii}(jj,2)));
    end
end

avg_angle = nanmean(moa,2);

m.uniquedist = dist;
m.avgangle = avg_angle;

```

With dot product and unique distance calculated, plots of $\langle \cos \theta \rangle$ vs distance d can now be made and fitted to an exponential function to extract correlation length P (Figure S2).

```

udist = m.uniquedist.*0.161;

g = fitype('a+b*exp(-c*x)');
f = fit(udist,m.avgangle,g,'Exclude',udist > uthres);

figure()
hold on
plot(f,udist,m.avgangle,'.')
xlabel('Distance[\mum]')
ylabel('<cos \theta> of two stress vectors')
ylim([0 1])
saveas(gcf,['AngleDist',samp,'.png'])
m.fitmodel = f;
m.b = f.b;
m.c = f.c;

```

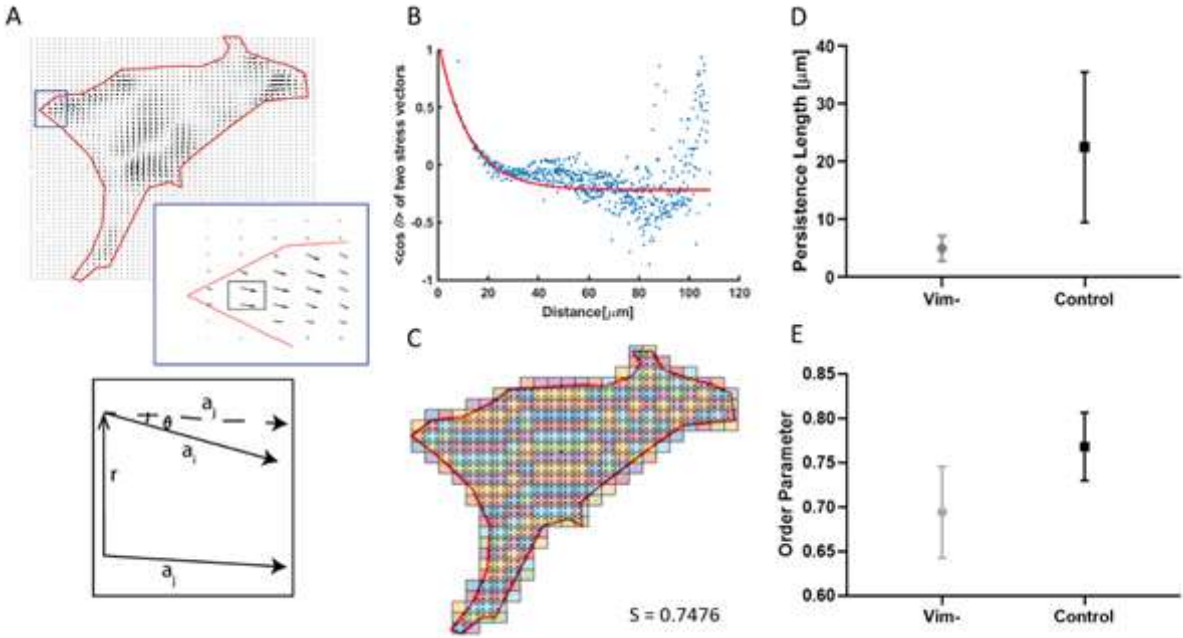


Figure S2. (A,B) Demonstration of correlation length calculation. (C) Demonstration of order parameter calculation. Result of average correlation length (D) and (E) order parameter for control and shVim fibroblasts.

Appendix C. Time lapse TFM (MATLAB)

C1. Time lapse TFM (TFMTL)

For n number of frames, we can simply write a loop to run TFM packages n times to analyze the whole movie. However, this is a very inefficient usage of computation time, especially since a complete analysis of one single cell could take up to 5 minutes. Analyzing a whole 5 hours video (assuming 5 minutes between frame) of a single cell would take 300 minutes to complete, not counting human interaction time (drawing cell boundary, ROI cropping, ...). Hence, we need to make use of multi-core processing. First, we need to separate parts of the code that require human interaction. Then, we can optimize the de-drifting, PIV, constructing ANSYS model and plotting code (automated tasks) such that each core can work independently on these tasks one frame at a time. This can be done by making asynchronous calls (non-blocking execution) to functions running those tasks on all cores available in the system. Since some tasks share similar resources such as ROI, crop size, gel conditions, ... ; we can optimize even further with parallel processing, which requires well-defined uniform inputs (in our case, a uniform non changing frame-by-frame image/input matrices' size). This method is preferable to asynchronous programming since we can easily optimize these codes to run on GPU or NPU (which has a lot more cores than traditional CPU server) by converting MATLAB matrices into gpuArrays. The codes here are written for CPU. Assuming we are running on arcts-01 (12 cores), the computation time is reduced by roughly a factor of 12.

Human Interaction Part: Biggest change from static TFM is the usage of a TIFF stack to store images. We need to grab the stack of phase contrast image and trace each cell by hand (or by thresholding if the image has fluorescent labels). Below is the tracing by hand version:

```

FileTif=uigetfile('*.TIF', 'Pick Phase Tiff Stack');
InfoImage=imfinfo(FileTif);
mImage=InfoImage(1).Width;
nImage=InfoImage(1).Height;
NumberImages=length(InfoImage);
FinalImage=zeros(nImage,mImage,NumberImages,'uint16');
StackImage=zeros(nImage,mImage,'uint16');

TifLink = Tiff(FileTif, 'r');
for i=1:NumberImages
    TifLink.setDirectory(i);
    FinalImage(:,:,i)=TifLink.read();
    StackImage=StackImage+FinalImage(:,:,i);
end
TifLink.close();
StackImage=StackImage./NumberImages;

for i = [1:NumberImages]
    cellimg=imcrop(FinalImage(:,:,i),rect);

    [cellTrace] = epiTrace(cellimg,0.9);
    figure, imshow(cellimg,[])
    hold on
    plot(cellTrace(:,1),cellTrace(:,2),'r.')
    hold off
    if retrace == 1
        figure, imshow(cellimg,[])
        title('Please trace the cell outline');
        disp('Please trace the cell outline in the figure');
        [bwc,xc,yc]=roipoly;
        reg=bwlabel(bwc);
        [s,L]=bwboundaries(bwc);
        hold on,plot(s{1}(:,2),s{1}(:,1),'r.')
        hold off
        cellx=s{1}(:,2);
        celly=s{1}(:,1);
        cellTrace = [cellx celly];
        g=regionprops(L, 'PixelList', 'Area', 'Centroid');
        Cell_Area=g.Area;
        centroids = cat(1, g.Centroid);
    else
        g = polyshape(cellTrace(:,1),cellTrace(:,2));
        Cell_Area = g.area;
        [centroids(:,1), centroids(:,2)] = g.centroid;
    end
end

```

Parallel Processing Part:

- Adjusting for image shift on before and after trypsinization image stacks:

```
parfor i = 1:NumberImages
    sd = load([samp, '-T', num2str(i), '.mat']);
    rect=sd.cellrec;
    recs=sd.rectd;

    a_org=FinalImage(:, :, i);
    a = bpassTF(a_org, 0, 7, 0.05*mode(a_org(:)));

    loading=imcrop(a, rect);

    [xd yd]=im_shift(a, b, recs);
    %If enough to cut
    if rect(2)+yd+rect(4)<size(b,1)
        nulfig=imcrop(b, rect+[xd yd 0 0]);
        cimg = createoverlayimg(loading, nulfig);
    else
        cimg = 'Error cutting';
        writeerror([samp, '-T', num2str(i)], 'TFMTL_Prep4:Not enough to cut')
    end

    sd.cimg=cimg;
    sd.loading=loading;
    sd.nulfig=nulfig;
    sd.drift=[xd, yd];
    parsavestruct([samp, '-T', num2str(i), '.mat'], sd)
end
```

- Parallel PIV:

```

parfor i=j:k
    sd = load([samp, '-T', num2str(i+n), '.mat']);
    [xi,yi,iu,iv,D]=mpiv(sd.nulfimg,sd.loading,36,36,0.5,0.5,11,11,1,'mqd',1,0);
    [iu_f,iv_f,iu_s, iv_s] = mpiv_filter(iu,iv, 2, 3.0, 3, 0);
    [iu_i, iv_i] = mpiv_smooth(iu_s, iv_s, 0);

    %check and replace NaN fields in iu_i and iv_i with 0
    iu_i(isnan(iu_i))=0;
    iv_i(isnan(iv_i))=0;
    [xm,ym]=meshgrid(min(xi):xi(2)-xi(1):max(xi),min(yi):mean(diff(yi)):max(yi));
    %remove drift. the drift will be taken as the x and y displacements at
    %nodes outside the cell.
    iu_m=iu_i;
    iv_m=iv_i;
    [xdata,ydata,bw,xc,yc]=roipoly(sd.cimg,sd.cellTrace(:,1),sd.cellTrace(:,2));
    bws=imresize(bw,size(iu'));
    bws=bws';
    ids=find(bws(:)==0);
    driftx=mean(iu_m(ids));
    drifty=mean(iv_m(ids));

    dispm=sqrt(iu_m(ids).^2+iv_m(ids).^2);
    dnoise=nanstd(dispm);
    iu_m=iu_i-driftx;
    iv_m=iv_i-drifty;
    %% Autoremove displacement outside cell ROI
    try
        newTrace = moveBoundary([samp, '-T', num2str(i+n)],30)
        [xdata,ydata,bw,xc,yc]=roipoly(sd.cimg,newTrace.xTraceOut,newTrace.yTraceOut);
    catch
        warning('new trace error - trace outside of image edge')
        writeerror([samp, '-T', num2str(i+n)], 'TFMTL_Dis2:expand boundary error')
    end
    xgrid = xm';
    ygrid = ym';
    [in, on] = inpolygon(xgrid,ygrid,xc,yc);
    iu_m(~in & ~on)=0;
    iv_m(~in & ~on)=0;

    parwritedispimg(samp,i+n,sd.cimg,sd.xgrid,sd.ygrid,sd.xdisp,sd.ydisp,sd.cellTrace);
    parsavestruct([samp, '-T', num2str(i+n), '.mat'],sd);
    close all
end
end

```

- ANSYS is built to be run with parallel processing. Hence, we only need to specify the number of cores to be used when constructing the ansys model. The compiler will take care of the rest.

C2. Fitting

Since the maximum stress growth profile exhibits an exponential growth accompany by a plateau, we can fit the maximum stress over time to an exponential of the form: $Y = Y_0 + (Plateau - Y_0) * (1 - e^{-kt})$. With this, plateau traction stress for both cell lines as well as the rate of increase (k). Furthermore, maximum stress over time can be normalized against the plateau maximum stress to compare growth profiles between different populations. Fitting and normalization were done directly in GraphPad Prism 8 due to excellent descriptive statistics that come with the exponential plateau model available in the software.

Appendix D. Migration Analysis (Python & VBA)

C1. Trajectories

Trajectories were plotted as the positions of each cell centroid over time. Example:

```
plot((CtrlCent{i}.Cent(:,1)-CtrlCent{i}.Cent(1,1))*0.161,(CtrlCent{i}.Cent(:,2)-
(CtrlCent{i}.Cent(1,2)))*0.161)
```

C2. Displacement and Total Distance

Displacement was calculated using the difference in final position t_f and initial position t_i . Total distance traveled was calculated as the sum of displacement from each time point t_i with the previous time point t_{i-1} .

```

import numpy as np
import pandas as pd
import seaborn as sns
import matplotlib.pyplot as plt

controlDF = pd.read_csv('CtrlCentroid.csv', header=None)
vimDF = pd.read_csv('VimCentroid.csv', header=None)

t = np.zeros([27,1])
t = controlDF[0][0:28]

CDisp = np.zeros(len(controlDF))
VDisp = np.zeros(len(vimDF))

CtrlDirR = np.empty([int(len(controlDF)/len(t)),2]) #0: Disp (d), totalDisp (D)
VimDirR = np.empty([int(len(vimDF)/len(t)),2])

j = 0
aggC = 0
aggV = 0

for i in range(1, len(vimDF)):
    if i%28 == 0:
        CDisp[i] = 0
        VDisp[i] = 0
        CtrlDirR[j][0]= ((controlDF[1][i-1]- controlDF[1][i-28])**2 + (controlDF[2][i-
1] - controlDF[2][i-28])**2)**0.5
        VimDirR[j][0]= ((vimDF[1][i-1]-vimDF[1][i-28])**2 + (vimDF[2][i-1] - vimDF[2][i-
28])**2)**0.5
        CtrlDirR[j][1]= aggC
        VimDirR[j][1]= aggV
        aggC = 0
        aggV = 0
        j = j+1
    else:
        CDisp[i] = ((controlDF[1][i]- controlDF[1][i-1])**2 + (controlDF[2][i] - controlDF[2][i-
1])**2)**0.5
        VDisp[i] = ((vimDF[1][i]-vimDF[1][i-1])**2 + (vimDF[2][i] - vimDF[2][i-1])**2)**0.5
        aggC = aggC +CDisp[i]
        aggV = aggV +VDisp[i]

```

C3. Directional Autocorrelation

Directional Autocorrelation (DA) were calculated using a slightly modified Diper [136]. Most changes made to the original code were related to Excel cells' position/highlight (bug fixing), which do not change the code's algorithm. Results of directional autocorrelation are plotted using Prism and MATLAB.